Mount Interference and Flow Angle Impacts on Unshielded Total Temperature Probes

Reuben Alexander Quickel

Thesis submitted to the faculty of the Virginia Polytechnic Institute and State University in partial fulfillment of the requirements for the degree of

Master of Science

In

Aerospace Engineering

K. Todd Lowe

Joseph A. Schetz

Walter F. O'Brien

May 2, 2019

Blacksburg, Virginia

Keywords: Total Temperature, Heat Transfer, Mount Effects, Flow Angle, Conduction, Convection, Aerodynamic Error

Mount Interference and Flow Angle Impacts on Unshielded Total Temperature Probes

Reuben Alexander Quickel

ABSTRACT

Accurately measuring the total temperature of a high-speed fluid flow is a challenging task that is required in many research areas and industry applications. The difficulty in total temperature measurement generally stems from attempting to minimize measurement error or accurately predict error so it can be accounted for. Conduction error and aerodynamic error are two very common sources of error in total temperature probe measurements. Numerous studies have been performed in prior literature to account for simple cases of both errors. However, the impacts of a mounting strut and freestream flow angle on conduction error and aerodynamic error have not been previously modeled. Both of these effects are very common in gas-turbine applications of total temperature probes. Therefore, a fundamental study was performed to analyze the impact of mount interference and freestream flow angle on a probe's conduction error and aerodynamic error.

An experimental study of aerodynamic error was performed using strut-mounted thermocouples in a high-speed jet at Mach numbers ranging from 0.25-0.72. This study showed that a strut stagnation point can provide aerodynamic error reductions and insensitivity to approach Mach number. An off-angle experimental study of conduction error was also performed using strut-mounted thermocouples at pitch angles ranging from -30° to 30°. High-fidelity Computational Fluid Dynamics (CFD) simulations with Conjugate Heat Transfer (CHT) were performed in conjunction with the experiments to provide key heat transfer information and flow visualizations. It was identified that unshielded total temperature probes have reduced conduction error at off-angles, but are sensitive to changes in the freestream flow angle. A low-order method was developed to account for mount interference and flow angle effects. The developed low-order method utilizes a local Mach number for aerodynamic error predictions and a local Reynolds number for conduction error predictions. This developed low-order method was validated against experimental and 3D, CFD/CHT results, and was shown to accurately capture flow angle trends, mount interference effects, and the impacts of varying probe geometry.

Mount Interference and Flow Angle Impacts on Unshielded Total Temperature Probes

Reuben Alexander Quickel

GENERAL AUDIENCE ABSTRACT

Accurately measuring the total temperature of a high-speed fluid flow is a challenging task that is required in many research areas and industry applications. Many methods exist for measuring total temperature, but the use of thermocouple based probes immersed into a flow remains a common and desirable measurement technique. The difficulty in using thermocouple based probes to acquire total temperature stems from attempting to minimize or accurately predict the probe's measurement error. Conduction, convection, and radiation heat transfer between the fluid flow and probe create challenges for minimizing measurement error so that the accurate total temperature can be obtained. Numerous studies have been performed in prior literature to account for simple cases of each error source. However, there are many complex, practical applications in which the influence of each error source has not been studied. The impacts of a freestream flow angle and the total temperature probe's mounting structure have not been previously modeled. Both of these effects are very common in gas-turbine applications of total temperature probes. This Thesis will present a fundamental study analyzing the impact that freestream flow angle and a probe's mount have on a total temperature probe's measurement error. The influence of conduction and convection heat transfer was studied experimentally for numerous probe geometries, and the impacts of a mounting strut and freestream flow angle were analyzed. A low-order method was developed to predict conduction error and aerodynamic error for total temperature probes in off-angle conditions with the presence of mount interference. The developed low-order method was shown to accurately capture the effects of a mounting strut, varying probe geometry, and varying flow angle. Additionally, the low-order method was validated against experimental and 3D, CFD/CHT results.

Acknowledgements

There are numerous individuals that I would like to acknowledge and thank for their contributions and support throughout my graduate school journey at Virginia Tech. I would like to thank both my co-advisors Dr. Todd Lowe and Dr. Joseph Schetz. Their regular support and technical guidance drove me to pursue my Master of Science, and played a significant role in the successful completion of my graduate school work. They have both been great advisors, and have helped me grow professionally to become a better engineer.

I would like to thank Pratt and Whitney for funding this research and for providing excellent opportunities through the continued partnership with Virginia Tech. I would like to thank Dr. Charlie Haldeman, Andrew Consiglio, Tyler Englerth, and Ian Agoos at Pratt & Whitney for their frequent project feedback and insightful discussions.

I would like to acknowledge the support of all my friends, many of whom I have met during my years at Virginia Tech. I have greatly enjoyed the relaxing time spent with friends outside of work, and also appreciate the support and shared knowledge given by fellow students. I would like to thank my team members Tyler Vincent and Sean Powers for their valuable assistance with the computational and experimental work discussed in this paper.

Thank you to my girlfriend, Emily Sewell, for being patient, supportive and by my side throughout my Bachelors and Masters completion. Finally, thank you to my family for the continuous encouragement and for supporting my decisions and educational track.

Table of Contents

1 Introduction 1
1.1 Governing Relations of Thermocouple Performance 1
1.2 Aerodynamic Error 3
1.3 Conduction Error 4
1.4 Radiation Error 5
1.5 Transient Error 6
1.6 Total Temperature Probe Design History and Applications 7
2 Low-Order Models 11
2.1 Modeling Aerodynamic Error with Mount Interference 11
2.2 General Conduction Error Models 14
2.3 Enhanced Conduction Error Models 16
3 Computational Modeling Methods 19
4 Experimental Setup, Instrumentation, and Methods 22
4.1 Virginia Tech Heated Jet Rig 22
4.2 Velocity Error Experiment – Sensor Assembly and Procedure 24
4.3 Experimental Methods for Inducing & Measuring Conduction Error 27
4.4 Virginia Tech Open Jet Wind Tunnel 30
4.5 Conduction Error Experiment – Sensor Assembly and Procedure 32
4.6 Additional Conduction Error Investigations 37
5 Results 40
5.1 Aerodynamic Error Experiment Results 40
5.2 Aerodynamic Error Low-Order Model Predictions 41
5.3 Aerodynamic Error Results – Uncertainty Quantification 45
5.4 Conduction Error Experimental and CFD/CHT Results 48
5.5 Unsteady and Cambered Conduction Error Experiment Results 56
5.6 Various Conduction Error Low-Order Model Predictions 59
5.7 Conduction Error Results – Uncertainty Quantification 69
6 Conclusion 76
6.1 Future Work 78
REFERENCES 79

List of Figures

Figure 1.1: Diagram of a type E thermocouple circuit 2
Figure 1.2: Common thermocouples types used in total temperature probes 2
Figure 1.3: Types of shielded total temperature sensors 8
Figure 1.4: Diagram of straight shield total temperature probe design 8
Figure 1.5: Additional thermocouple configurations 9
Figure 2.1: Rankine half-body flow-field and an illustrated virtual probe position 13
Figure 2.2: Virtual probe method with example flow-field and virtual probe line 18
Figure 3.1: 2D mesh for modeling the flow-field around cambered strut 20
Figure 4.1: Virginia Tech Hot Jet Facility 22
Figure 4.2: Detailed diagram of jet configuration 23
Figure 4.3: Plenum total temperature sensor 23
Figure 4.4: Diagram of nozzle mount for sensor assembly 24
Figure 4.5: NACA 0024 airfoil profile 24
Figure 4.6: Sensor assembly for aerodynamic error experiment 25
Figure 4.7: Beaded, bare wire thermocouple in ceramic tube 26
Figure 4.8: Methods to induce conduction error 1) Heated flow, 2) Chilled mount, 3) Heated mount 29
Figure 4.9: Virginia Tech Open Jet Wind Tunnel 30
Figure 4.10: External view of Virginia Tech Open Jet Wind Tunnel closed test section 31
Figure 4.11: Internal view of Virginia Tech Open Jet Wind Tunnel closed test section setup 32
Figure 4.12: Symmetric strut profile for conduction error experiments 33
Figure 4.13: Nexthermal coil heater geometry and specifications 33
Figure 4.14: Base temperature probe assembly 34
Figure 4.15: Strut-internal heated total temperature sensor assembly 35
Figure 4.16: Fully assembled unshielded total temperature sensor 35
Figure 4.17: Conduction error experiment, tested probe geometries 36
Figure 4.18: Diagram of forced unsteadiness experiment 37
Figure 4.19: Cambered strut profile 38
Figure 4.20: Open test section mounting configuration 39
Figure 5.1: Comparison of Mach sweep experiment results 40
Figure 5.2: Comparison of experiment results and low order aero recovery predictions for sheathed L/t = 0.067 probe 41
Figure 5.3: Comparison of experiment results and low order aero recovery predictions for sheathed L/t = 0.15 probe 42
Figure 5.4: Comparison of experiment results and low order aero recovery predictions for sheathed L/t = 0.059 bare wire probe 42
Figure 5.5: Comparison of experiment results and total recovery predictions using combined conduction and aerodynamic error, sheathed L/t = 0.067 probe 44

Figure 5.6: Comparison of experiment results and total recovery predictions using combined conduction and aerodynamic error, sheathed L/t = 0.15 probe 45
Figure 5.7: Uncertainty of aerodynamic error experiment results 47
Figure 5.8: Uncertainty of LOM aerodynamic error predictions 48
Figure 5.9: Experimental results for 0.020", L/d = 5 (L/t = 0.08) probe in symmetric strut 49
Figure 5.10: Experimental C.S. collapse for the nominal 0.020", L/d = 5 probe 49
Figure 5.11: Sensor CFD/CHT prediction of averaged convection coefficient vs. freestream flow angle for 0.02 in., L/d = 5 probe 50
Figure 5.12: CFD/CHT results of streamlines around 0.020", L/d = 5 probe, 0° and 10° freestream flow angles 51
Figure 5.13: Experimental results for L/t study in symmetric strut 52
Figure 5.14: CFD/CHT predictions of sensor averaged convection coefficient vs. freestream flow angle for L/t study 52
Figure 5.15: CFD/CHT predictions of streamlines around 0.020", L/t = 0.08 and L/t = 0.16 probes, 10° freestream flow angle 53
Figure 5.16: Experimental results for probe diameter study in symmetric strut 54
Figure 5.17: CFD/CHT predictions of sensor averaged convection coefficient vs. freestream flow angle for diameter study, 3D CFD results 54
Figure 5.18: Experimental impacts of forced unsteadiness on unshielded total temperature probe, 0.020" O.D., L/d = 5 56
Figure 5.19: Virginia Tech Open Jet Wind Tunnel test section influence, experimental results for 0.020" O.D., L/d = 5 probe 57
Figure 5.20: 3D CFD results vs Virginia Tech Open Jet Wind Tunnel test section influence, 0.020" O.D., L/d = 5 58
Figure 5.21: Experimental results for 0.020", L/d = 5 (L/t = 0.08) probe in cambered strut 59
Figure 5.22: Total velocity contours used for virtual probe method, symmetric strut 60
Figure 5.23: Virtual probe lines from symmetric strut 2D CFD solutions 61
Figure 5.24: Comparison of experiment results and predictions using Virtual Probe Method with Moffat perpendicular flow correlation and enhanced conduction model, 0.020" L/d = 5 probe . 62
Figure 5.25: Comparison of predictions using Virtual Probe Method, enhanced conduction model and three different Nu-Re correlations. Additional Moffat, Perp. flow predictions performed with standard conduction model, 0.020" L/d = 5 probe 63
Figure 5.26: Comparison between experiments, 3D CFD results, and predictions using Virtual Probe Method, enhanced conduction model, and Churchill-Bernstein and ⊥ Moffat correlations, 0.020" L/d = 5 probe 64
Figure 5.27: Comparison of experiments and low-order predictions using Virtual Probe Method, enhanced conduction model, and Churchill-Bernstein and ⊥ Moffat correlations. Symmetric strut, for the L/t variation study 65
Figure 5.28: Comparison of experiments and low-order predictions using Virtual Probe Method, enhanced conduction model, and Churchill-Bernstein and ⊥ Moffat correlations. Symmetric strut, for the diameter variation study 65

Figure 5.29: Comparison between experiments, 3D CFD, and low order predictions using Virtual Probe Method, enhanced conduction model, and Churchill-Bernstein and Moffat perpendicular flow correlations. Symmetric strut, for the L/t variation study..... 66
Figure 5.30: Comparison between experiments, 3D CFD, and low order predictions using Virtual Probe Method, enhanced conduction model, and Churchill-Bernstein and Moffat perpendicular flow correlations. Symmetric strut, for the diameter variation study 66
Figure 5.31: Total velocity contours used for virtual probe method, cambered strut..... 67
Figure 5.32: Virtual probe lines from cambered strut 2D, CFD solutions 68
Figure 5.33: Comparison between symmetric strut and cambered strut virtual probe lines..... 68
Figure 5.34: Comparison of cambered experiment results and predictions using Virtual Probe Method, enhanced conduction model, and both the Moffat perpendicular correlation and Churchill-Bernstein correlation, 0.020 in. L/d = 5 probe 69
Figure 5.35: Symmetric strut conduction sensitivity results with $\pm$ 2 standard deviations, L/t and diameter studies 70
Figure 5.36: Symmetric strut conduction sensitivity and total uncertainty results for L/t and diameter studies 71
Figure 5.37: Cambered strut conduction sensitivity and total uncertainty 71
Figure 5.38: Comparison of total uncertainty for low-order predictions and experiment results, symmetric strut configurations, Moffat $\perp$ correlation 73
Figure 5.39: Comparison of total uncertainty for low-order predictions and experiment results, symmetric strut configurations, Churchill-Bernstein correlation 73
Figure 5.40: Comparison of total uncertainty for low order predictions and experiment results, symmetric strut configurations, Churchill-Bernstein correlation 74
Figure 5.41: Comparison of total uncertainty for low-order predictions using different dependent variables, uncertainty of symmetric strut predictions using Moffat $\perp$ correlation 75

List of Tables

Table 5.1: Summary of the percent difference between the recovery of each low order method and the experiment results 43
Table 5.2: Summary of time-averaged, conduction sensitivity values for all probe geometries and pitch angles experimentally tested on symmetric strut 55
Table 5.3: Summary of conduction sensitivity values calculated from 3D CFD/CHT results, symmetric strut 56

Nomenclature

θ	Conduction Driver
M	Mach number
R	Overall Recovery Factor
h	Convection Heat Transfer Coefficient
S	Seebeck Coefficient
T_t	Total Temperature
T_j	Junction Temperature
$T_{j,i}$	Junction Temperature
T_b	Base Temperature
T_s	Static Temperature
ΔV	Voltage Difference
V	Total Velocity
E_v	Velocity Error
E_c	Conduction Error
E_r	Radiation Error
E_t	Transient Error
C_p	Specific Heat Capacity
α	Aerodynamic Recovery Factor
γ	Specific Heat Ratio
A	Reference Area
L	Reference Length
d	Thermocouple Diameter
k_{tc}	Effective Thermal Conductivity of the Thermocouple
k_{fluid}	Thermal Conductivity of the Fluid
K_r	Form Factor
ε	Emissivity
σ	Stefan-Boltzmann Constant
τ	Time Constant
ρ	Density
β	Prandtl-Glauert Factor
Bi	Biot Number
Re	Reynolds Number
Nu	Nusselt Number
P	Reference Perimeter
Pr	Prandtl Number
P_s	Static Pressure
P_t	Total Pressure
St	Strouhal Number
f	Shedding Frequency

1 Introduction

Obtaining an accurate measurement of the total temperature of a fluid is a significant requirement in many modern industries and areas of research. Wind tunnels, high speed jets, hypersonic flows, and the jet engine industry are just a few examples of practical work that require accurate total temperature measurements. The jet engine industry in particular, has a great need to measure the total temperature of gas flows at numerous locations throughout the engine. Crucial performance, efficiency, and part life metrics are determined by the fluid's total temperature at various states. A standalone thermocouple or combination of a thermocouple and stagnation tube have become standard equipment used to measure total temperature in the jet engine industry. This type of total temperature sensor is commonly attached to a support structure and used for measurements in the compressor, turbine, and nozzle of a jet engine. One of the most important and challenging areas within the engine to accurately know the total temperature is the high-pressure turbine (HPT). Within the HPT, gas temperatures can exceed the melting temperature of many common metals, and large temperature gradients, flow velocities, unsteadiness, and turbulence are present.

HPT blades and vanes are designed with internal cooling channels that discharge cooled air out of the blade/vane to create a cooled film along the part surface that protects it from extreme conditions. Similarly, a total temperature sensor must be mounted to a cooled support structure to acquire measurements within a harsh environment such as the HPT. This mounting configuration results in large conduction effects that have the potential to create a significant error in the sensors reading. Likewise, the extreme environment results in radiation, transient, and aerodynamic errors that can further prevent the total temperature sensor from reading the true total temperature of the fluid. The magnitude of these errors is greatly dependent on the flow conditions and geometry of the probe. There exists a wide range of prior literature relating to the prediction of simple cases of each error source [1-12,24,25,34,35], but the prediction of these error sources is still an active area of study and development. The error relating to total temperature sensors with a stagnation tube (shielded sensor) has been largely characterized and successfully predicted in previous literature [1-12]. However, the use of a stagnation tube inherently creates a larger sensor which can be undesirable in many jet engine applications. If the stagnation tube is removed, the mounting structure and freestream flow angle will have a significantly increased impact on the sensor's performance and associated errors. The influence of mount interference effects and flow angle have not been modeled in prior literature; therefore, the present study will seek to understand and quantify these effects on an unshielded total temperature probe.

1.1 Governing Relations of Thermocouple Performance

A thermocouple is a device that consists of an electrical junction formed between two dissimilar conductive materials. The thermocouple produces a temperature dependent voltage that can be used to measure temperature through the Seebeck Effect. The Seebeck Effect explains that if two

different metals are attached at both ends, and one junction is placed in something hot while the other junction is placed in something cold, then a voltage (potential difference) is created. If the thermocouple has reached a steady state the temperature difference along the thermocouple can be directly calculated from the induced voltage using Equation 1.1 where S is the Seebeck coefficient, a local material property [16].

$$\Delta V = S(T_h - T_c) \tag{1.1}$$

If one of the two junction temperatures are known, then Equation 1.1 can be used to determine the temperature of the other junction. This known temperature is called the reference temperature and is commonly a physical or digital ice point. A diagram of a thermocouple circuit can be seen in Figure 1.1.

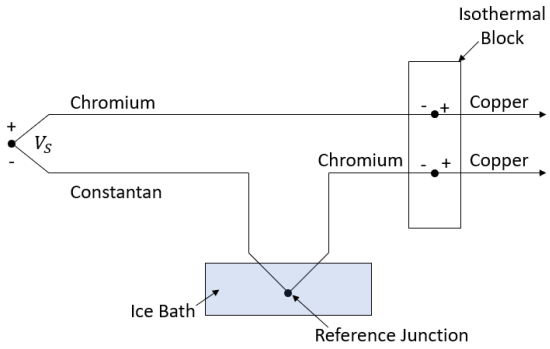

Figure 1.1: Diagram of a type E thermocouple circuit

Thermocouples can be manufactured from numerous materials in many sizes and shapes. The materials used in a thermocouple will determine the measurement temperature range while the geometry will impact the probe's strength, time response, and associated errors. Figure 1.2 shows a diagram of six different types of thermocouples. Generally, exposed and bare-wire butt-welded thermocouples have the fastest time response, while sealed sheaths with an isolated junction have the slowest response. All of the thermocouples used in this study will be sealed sheaths with a grounded junction unless explicitly stated otherwise. This type of thermocouple provides an acceptable time response relative to an isolated junction while simultaneously benefitting from the strength and protection provided from the sealed sheath.

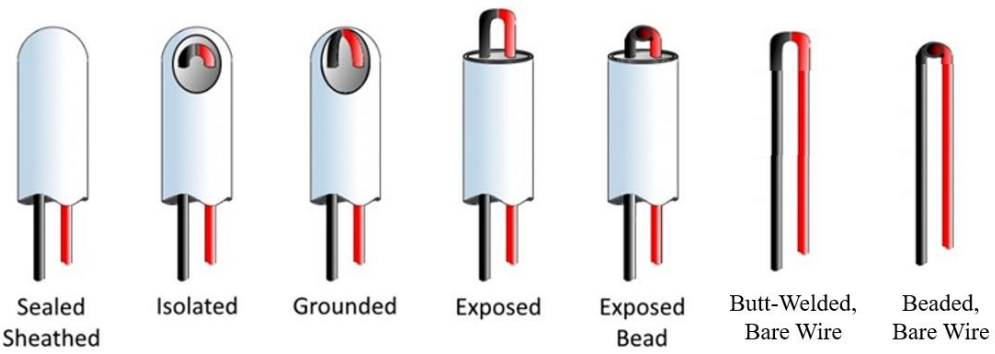

Figure 1.2: Common thermocouples types used in total temperature probes (from Ref. [18])

The overall performance of a thermocouple-based total temperature sensor is defined by the ratio of the measured temperature to the total temperature of the fluid. This non-dimensional ratio is referred to as the overall recovery factor, R, and is described by Equation 1.2. Tt is the total temperature of the fluid, and T_j is the thermocouple measured temperature. The total temperature of a moving fluid is given in Equation 1.3 which accounts for the kinetic energy of the fluid as well as its static temperature and represents the true fluid temperature if it was stagnated adiabatically.

$$R = \frac{T_j}{T_t} \tag{1.2}$$

$$T_t = T_s + \frac{V^2}{2C_p} \tag{1.3}$$

Therefore, the overall recovery factor measures how well the total temperature probe is able to recover the total thermal energy of the moving fluid. Convection is the heat transfer mechanism by which thermal energy is transferred from the moving fluid to the total temperature probe junction. However, other heat transfer processes such as conduction and radiation also transfer energy to and from the total temperature probe's junction resulting in a measured temperature different than the true total temperature of the flow. Therefore, the heat transfer balance between these competing mechanisms must be understood to optimize a probe design, predict a probe's measured temperature, or determine the true total temperature from a measured temperature. One initial step to analyze this heat transfer balance is to independently identify the impact of each error source. These error sources are usually linearly subtracted from the ideal recovery ratio of 1 to acquire a prediction for the probe's measured temperature. This method, described in Equation 1.4, can be used to estimate the overall recovery factor without obtaining both the true total temperature and a measured temperature.

$$R = 1 - E_v - E_c - E_r - E_t \tag{1.4}$$

However, often in real applications each error source will not be independent of the others. Conduction and radiation are generally coupled effects that must be analyzed or solved simultaneously. Therefore, the method of analyzing each error source independently may not always be ideal, but it can be valuable for parameter studies or for situations where one error source is dominant. The following sections will discuss a probe's recovery potential in the presence of pure convection as well as analyze the effects of conduction and radiation on probe performance.

1.2 Aerodynamic Error

Velocity or aerodynamic error is present for all total temperature sensors and can be a primary source of error for high recovery probes in high-speed flows. When a moving fluid encounters a solid body, a boundary layer forms along the body surface. Within this boundary layer the flow velocity is continuously reduced until it becomes completely stagnated at the surface of the object. During this velocity reduction in the boundary layer the moving fluid's kinetic energy is converted to thermal energy [19]. However, this conversion process is non-ideal, resulting in the fluid not

completely recovering the total temperature of the flow at the surface of the body. For a total temperature probe, this leads to some total temperature redistributed inside the boundary layer and a fluid stagnation temperature at the probe's surface that is lower than the flow total temperature. This results in a measurement error in the sensor temperature reading due to aerodynamic recovery or velocity error. Some key parameters when determining velocity error are the flow Mach number, the ratio of specific heats of the fluid γ, and the aerodynamic recovery factor α. The aerodynamic recovery factor α describes how efficiently the kinetic energy of a moving fluid is converted to thermal energy in the boundary layer and can be seen in Equation 1.5.

$$\alpha = \frac{T_j - T_s}{T_t - T_s} \tag{1.5}$$

This aerodynamic recovery factor is dependent on the fluid Prandtl number and the geometry of the body, in this case the total temperature sensor. From prior literature, the aerodynamic recovery factor for an unshielded, bare-wire thermocouple positioned parallel to the flow has been found to be $\alpha = 0.86 \pm 0.09$ [8]. Meanwhile, the aerodynamic recovery factor for the same type of probe positioned normal to the flow has been found to be $\alpha = 0.68 \pm 0.07$ [8]. A formula can be developed for the junction temperature by using the isentropic relationship between total and static temperature seen in Equation 1.6. Solving for T_j in Equation 1.6 results in the junction temperature formula seen in Equation 1.7. Finally, by subtracting Equation 1.7 from the total temperature, the velocity error formula can be created as seen in Equation 1.8.

$$\frac{T_s}{T_t} = \left(1 + \frac{\gamma - 1}{2} M^2\right)^{-1} \tag{1.6}$$

$$T_j = T_t\left(1 - (1 - \alpha)\frac{[(\gamma - 1)/2]M^2}{1 + [(\gamma - 1)/2]M^2}\right) \tag{1.7}$$

$$E_v = 1 - \frac{T_j}{T_t} = (1 - \alpha)\frac{[(\gamma - 1)/2]M^2}{1 + [(\gamma - 1)/2]M^2} \tag{1.8}$$

Since aerodynamic recovery factor and specific heat ratios are generally fixed for a desired probe design, the total temperature probe geometry is typically designed to set a favorable Mach number over the sensor that minimizes velocity error. Historic probe geometries designed to reduce aerodynamic error are reviewed in Section 1.6.

1.3 Conduction Error

As previously mentioned, the junction reading of a total temperature probe is dependent on a heat transfer balance. One crucial part of this is the balance between convection and conduction. Conduction can be described as the interaction between microscopic particles that results in flow of internal energy from a high temperature area to a low temperature area. The rate at which energy is conducted is directly dependent on the temperature gradient that exists between two objects or along an object and the thermal conductivity of the material. The differential form of Fourier's Law, seen in Equation 1.9, states that the local heat flux q is equal to the product of the thermal conductivity, k, and the negative temperature gradient, ∇T.

$$q = \frac{1}{A}\frac{dQ}{dt} = -k\nabla T \tag{1.9}$$

Convection is a heat transfer mechanism described as the transfer of internal energy to or from an object by the movement of a surrounding fluid. Convection can occur freely or it can be forced when a fluid is propelled across an object or vice versa. Newton's Law of Cooling, seen in Equation 1.10, describes the heat loss due to forced convection, where h is the convection heat transfer coefficient and A is the exposed area.

$$\frac{dQ}{dt} = -hA\Delta T(t) \tag{1.10}$$

Forced convection is highly desirable when measuring a fluid total temperature as it is the primary mechanism to transfer energy from the moving fluid to the total temperature probe. However, the balance between conduction and convection results in a measurement error known as conduction error. Consider an unshielded, strut mounted thermocouple in a perpendicular cross flow, one simple method of modeling the conduction error is to treat the total temperature probe as a very long rod subjected to one-dimensional heat conduction. The solution to this model, expressed as conduction error, can be seen in Equation 1.11.

$$E_c = 1 - \frac{T_j}{T_t} = \frac{T_t - T_b}{T_t \cosh(L\sqrt{\frac{4h}{dk_{tc}}})} \tag{1.11}$$

This conduction error solution has been derived in Eckert and Drake (1959) and Özişik (1977) [20-21], and would be best used to describe a sealed sheath thermocouple with an insulated junction. Equation 1.11 shows that conduction error is dependent on the convection heat transfer coefficient h, effective thermal conductivity of the total temperature probe, k_{tc}, probe geometry, and the temperature difference between the total temperature of the flow and the base temperature of the probe. This temperature difference is very large and can result in substantial errors for thermocouples mounted on a cooled strut. Therefore, to minimize conduction error, the probe must be designed to provide a large denominator in Equation 1.11. This can be done by increasing the probe length, *L*, increasing the convection heat transfer coefficient, *h*, or decreasing the probe diameter, *d*. The convection heat transfer coefficient can be very difficult to predict, but is known to scale with Reynolds Number.

1.4 Radiation Error

Thermal radiation is another primary heat transfer mechanism that impacts the performance of total temperature sensors in the form of a measurement error called radiation error. Thermal radiation is a type of electromagnetic radiation that consist of waves carrying energy that propagate through space. Thermal radiation is emitted by all matter and is created by the thermal motion of particles within matter. Since radiation is emitted by all matter, the combined heat transfer to a thermocouple from radiation and convection is difficult to accurately predict. However, a simple model for radiation error can be seen in Equation 1.12. This formula accounts for the combination of convection and radiation from a single source to the thermocouple [8].

$$E_R = 1 - \frac{T_j}{T_t} = \frac{K_r \sigma \varepsilon A_r ({T_j}^4 - {T_w}^4)}{T_t h_c A_c} \quad (1.12)$$

As seen in Equation 1.12, radiation error can easily become very large at high temperatures since T_j and T_w are each raised to the fourth power. Other important variables within the radiation error equation are the form factor, K_r, the emissivity, ε, and the convection heat transfer coefficient, h. The form factor, K_r, also known as the view factor, relates to the geometry and orientation of the two bodies of interest and describes the amount of radiation leaving one object that will reach the other. Meanwhile, the emissivity, ε, of a material surface describes its ability to emit thermal radiation energy. Emissivity depends on temperature, the material, and surface geometry and can vary from zero to one. An emissivity of one is considered a perfect black body that emits the maximum amount of thermal radiation for a given temperature. Finally, radiation error is dependent on the Stefan-Boltzmann constant σ, the areas available for radiation A_r, and convection A_c. The available area for radiation and convection are typically the same for a total temperature probe and will therefore cancel in Equation 1.12.

The effects of radiation on total temperature probes have been studied in great detail [11,12,22-26]. Some of these studies identify emissivity for a large range of materials and the effects of oxidation and temperature on emissivity [27-30]. For shielded temperature probes, the view factor between the shield and probe can often be assumed to be near one, since the convection and radiation area are the same and the shield is typically a large body surrounding the probe. This makes the use of Equation 1.12 simple if the temperature of the shield is known. In other practical applications, such as an unshielded total temperature probe in a harsh environment like a turbine engine's HPT, numerous objects could contribute large amounts of radiation energy to the probe requiring a more complex method to analyze radiation error. Even in practical applications of shielded total temperature probes, the shield temperature will vary along its length and radiation from the shield will affect each location on the total temperature probe differently due to different view factors. Some work has been done attempting to model these more complex radiation situations [11-12]. However, complex radiation calculations are not generally needed in low temperature thermocouple applications and their need can be greatly reduced in high temperature applications if a total temperature probe is properly designed to minimize radiation error. Two potential methods to reduce radiation error are to control the surrounding wall temperatures or utilize a surface material with a low emissivity. Additionally, many total temperature probe designs utilize a shield to block radiation and reduce the number of significant sources providing radiation to the thermocouple.

1.5 Transient Error

Transient error is unique from the previously discussed types of measurement error, since it is caused by the thermal capacity of the materials used within a total temperature probe and related to its response rate. The measured temperature of a thermocouple junction always lags behind a change in the surrounding fluid flows temperature [8]. This is because heat must be transferred from the fluid flow to the probe junction to change the temperature. This transfer of energy requires

time, and therefore results in a temperature difference described by the measurement error known as transient error. This error can be determined from the probe time constant and the rate of change in the junction temperature as expressed in Equation 1.13.

$$E_T = 1 - \frac{T_j}{T_t} = \frac{\tau}{T_t}\frac{dT_j}{dt} \tag{1.13}$$

Equation 1.13 for a first-order instrument can be derived from the energy equation and comes from a balance between convection heat flow into the thermocouple and the rate of increasing internal energy within the probe [20]. The time constant, τ, is the ratio of thermal storage capacity to the heat intake per degree of temperature difference. This time constant is dependent on the object's volume to surface area, density, ρ, specific heat, C_p, and the convection heat transfer coefficient, h. The time constant for a thermocouple, assuming a thin rod with a volume to surface area of d/4, can be calculated using Equation 1.14 [8].

$$\tau = \frac{\rho C_p d}{4h_c} \tag{1.14}$$

This constant can be experimentally measured by recording the time the junction temperature takes to reach 63.2% of its final response to a change in the surrounding fluid flows temperature. Experimental methods for measuring the time constant have been studied in depth [32-34]. Additionally, other analytical methods for determining response rate and associated temperature delays have been discussed in Shepard (1977) and Goodwin (1945) [35,36]. A solution for the measured junction temperature at a given time can be determined by solving the differential equation in Equation 1.13 for T_j. Equation 1.15 shows the solution for T_j in terms of the time t, total temperature Tt, time constant, τ, and the initial junction temperature, $T_{j,i}$.

$$T_j(t) = \left(T_{j,i} - T_t\right)e^{-t/\tau} + T_t \tag{1.15}$$

Transient error is generally not a significant source of error in steady flows, but can be extremely large in unsteady flow with large temperature gradients. Total temperature probes can be designed to reduce transient error by minimizing the probe time constant. This is commonly done by decreasing the thermocouple diameter, but it can also be achieved by selecting a material with lower density or smaller specific heat.

1.6 Total Temperature Probe Design History and Applications

Research and development of total temperature probe design has been well recorded throughout the past century [3,4,6-10,23]. A historic goal for total temperature probe design has been to produce a sensor that provides minimal error for a given set of flow conditions. This goal can be achieved by minimizing the previously discussed error sources. Numerous types of shielded total temperature probes have historically been used to minimize error sources for a range of flow conditions. A range of different types of shielded total temperature sensors can be seen in Figure 1.3.

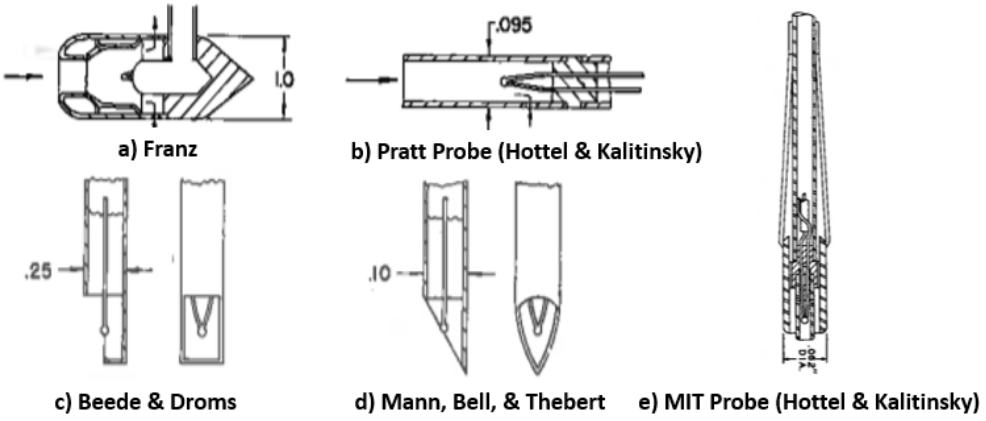

Figure 1.3: Types of shielded total temperature sensors (from Ref. [4,8])

Each of these sensor types have unique advantages and disadvantages; however, a probe is often selected based on its robustness and simplicity. For example, the design presented by Franz is uncommon due to its complex geometry and design [8]. One commonly utilized design is a redesign of the MIT probe known as the Pratt & Whitney probe [4]. This probe, discussed in Hottel and Kalitinsky (1945), provides a simple straight tube geometry around a thermocouple and features several bleed or vent holes circumferentially at one location along the straight tube. The straight stagnation tube used in this design allows the minimization of several previously discussed error sources. First, the stagnation tube acts as a shield for the thermocouple from radiation which greatly reduces radiation error. Secondly, the ratio of vent hole area to inlet area can be used to set a low internal velocity around the thermocouple within the tube which greatly reduces aerodynamic error. Finally, the conduction error can be minimized in this configuration by designing a probe with a long L/D ratio. A detailed diagram of the conventional straight tube Pratt & Whitney probe can be seen in Figure 1.4.

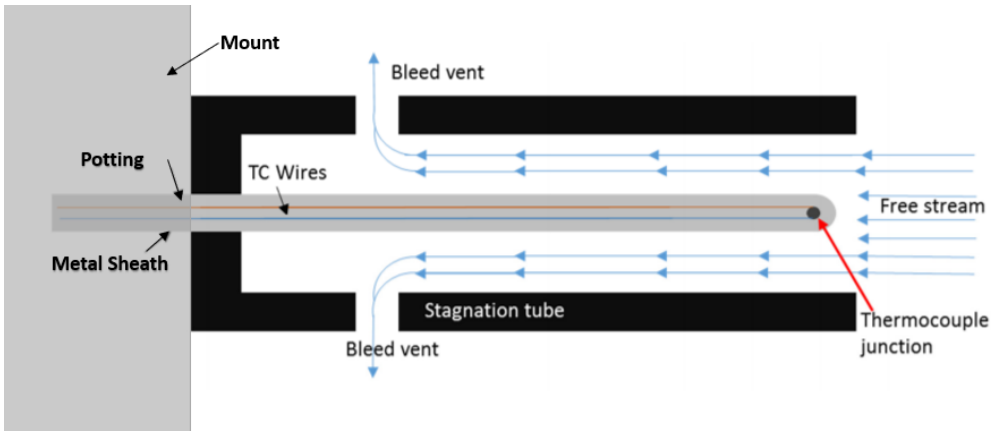

Figure 1.4: Diagram of straight shield total temperature probe design (from Ref. [31])

One other shielded total temperature probe design to note is the spade tip total temperature probe discussed by Beede and Droms [37]. The spade tip sensor utilizes similar features to the conventional Pratt and Whitney probe, and can be useful for applications where the sensor is inserted into the flow from a side wall or boundary.

The discussed shielded total temperature probe designs can be effective for producing a probe with minimal errors. However, historic designs of total temperature probes assume the probe can physically survive the flow environment and take little account of space constraints. Specifically, for jet engine applications, restrictive space constraints and flow temperatures above the probe material melting point could force probe design for high spatial resolution or survivability.

Shielded total temperature probe designs can be modified to prioritize probe survivability, but they will always have significantly worse spatial resolution than an unshielded total temperature probe. Similar to shielded sensors, there are numerous types of unshielded sensors each with varying advantages and disadvantages. Several types of thermocouples that can be used for unshielded total temperature probes have already been discussed in Figure 1.2, but additional unshielded designs can be seen in Figure 1.5.

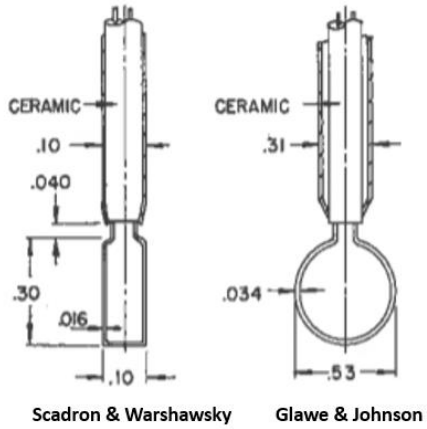

Figure 1.5: Additional thermocouple configurations (from Ref. [8])

All unshielded, total temperature probes are relatively simple in design compared to shielded sensors, but they are also generally more sensitive to changes in the flow environment. The simplicity and small size of these sensor types are excellent for maximizing spatial resolution or survivability; however, a cost of these new design objectives is that error minimalization must become a secondary design objective. This results in probes with a larger measurement error than the previously discussed optimized shielded sensors. With a larger measurement error, the importance of accurately predicting and calibrating for that measurement error increases. Therefore, it is ideal to select an unshielded total temperature probe with a geometry that is simple to model and analyze in order to predict its measurement error. Many beaded thermocouples for example, are complicated to accurately and easily model due to potential asymmetries in the bead and the interation of the bead wake with the supporting wires. Similarly, the Scardon and Warshawsky [38] probe and Glawe and Johnson [39] probe feature tip geometry that generate wakes which will interact with the downstream portion of the probe. A sealed sheath thermocouple design will be used throughout this paper and serves as a good option for unshielded total temperature probes because of its geometric simplicity and modeling ease.

Small, unshielded total temperature probes could be utilized in many gas turbine applications. By removing the shield and decreasing the probe size, both spatial and temporal resolution can be

greatly improved. This makes unshielded sensors attractive for temperature measurements in areas with small physical constraints, flow transients, and large temperature gradients. Unshielded total temperature sensors are much more susceptible to radiation, but they can still have minimized conduction error through a long probe L/d. Additionally, aerodynamic error can be minimalized by utilizing the effects of mount interference. Mount interference refers to a mounting strut significantly changing the flow-field around a total temperature sensor relative to the freestream flow. This significant change could be a result of the sensor being positioned near the stagnation region on the mount or at a location where the local flow is accelerated by the mount.

The flow physics and recovery of an unshielded, strut mounted total temperature probe behave very different than that of a traditional shielded probe design. Therefore, an investigation is needed to identify the recovery performance and flow physics around an unshielded, strut mounted total temperature probe. The next sections will analyze the effects of mount interference and freestream flow angle on unshielded, strut mounted total temperature probes. It will be shown that mount interference can be utilized by small, unshielded sensors to provide some benefits similar to a traditional shield. A simple, low-order model that utilizes potential flow to model aerodynamic error of a strut mounted total temperature probe will be presented. Additionally, a method to model the influence of mount interference and flow angle on conduction error will be discussed. Three-dimensional computational fluid dynamics (CFD) simulations will be used in low-order model development and to visualize key flow physics driving the behavior of sensor performance. Finally, experimental results will be used to validate the presented low-order methods.

2 Low-Order Models

Low-order models are used to predict total temperature probe performance for a wide range of geometries and flow conditions. They can be used to rapidly estimate sensor recovery and are a cheap and quick way to evaluate and compare sensor performance rather than performing experiments or full-scale 3D CFD simulations. Low-order models can also be extremely useful as a design tool. Their rapid evaluation time allows users to consider huge numbers of cases to optimize individual design parameters. They also give you the capability to study the influence of many nondimensional parameters such as Reynolds number, thermal conductivity, L/d, and Mach number along with many other parameters, but they require the associated physics to be encapsulated by the model. The discussed low-order models are physics-based solutions for the interaction between a flow-field and a simple sensor geometry. They often contain empirical data and are applicable only under certain conditions which must always be considered by the user.

2.1 Modeling Aerodynamic Error with Mount Interference

Analytical expressions to model aerodynamic error were previously discussed in Equations 1.6-1.8. These equations present a way to predict aerodynamic error based only on fluid Mach number and the aerodynamic recovery factor α. Therefore, if one can utilize the correct Mach number and aerodynamic recovery factor α, the aerodynamic error of a total sensor should be simple to predict. For most probe types, the aerodynamic recovery factor is simply a function of the flow angle. The values presented in Section 1.3 of $\alpha = 0.86 \pm 0.09$ for a parallel flow and $\alpha = 0.68 \pm 0.07$ for a perpendicular flow should hold true for most unshielded sensors composed of either sheathed or bare wire thermocouples. However, some of the uniquely shaped probes, like the Scardon and Warshawsky [38] probe and Glawe and Johnson [39] probe, may not follow these α values well due to shedding from the probe tip impacting downstream portions of the probe. Additionally, α is expected to fall between the two provided values for flow angles between 0 and 90 degrees. In prior literature, modifications to the original recovery factor formulation described in Equation 1.5 have been made to account for flow velocity reductions within a shielded total temperature sensor [8]. The shielded probe's corrected aerodynamic recovery factor is described in Equation 2.1.

$$\alpha' = 1 - (1 - \alpha)\left(\frac{{V_{int}}^2}{{V_{ext}}^2}\right) \tag{2.1}$$

This modified recovery factor accounts for the fluid's reduced velocity in a shield through a velocity ratio term. This is equivalent to using the flow Mach number local to the sensor instead of the freestream Mach number in Equation 1.8. A shielded, bare-wire probe positioned parallel to the flow, is commonly designed to have a roughly 1/8 velocity ratio to create a high recovery sensor [8]. Since a mounting strut similarly reduces the flow velocity around a total temperature sensor, Equation 2.1 could be used in combination with Equation 1.8 to model the probe's velocity error in the presence of mount interference if the local velocity at the probe location was known. This velocity local to the probe can be significantly different than the freestream velocity and is dependent on the mounting-strut geometry and probe length. The mount thickness and leading-

edge profile are two critical geometric features that will influence the velocity reduction caused by mount interference. Additionally, the velocity profile along the length of the sensor will vary as the flow velocity continuously decreases as it approaches the strut leading edge. However, for a low-order analytical prediction, the local flow velocity at the tip of the sensor can be used. This approximation provides an accurate estimation in parallel flow, since the flow around the tip of the probe has the highest velocity and largest influence on aerodynamic error.

In order to estimate the local flow velocity near the tip of the total temperature probe, simple analytical theories such as potential flow can be utilized. Potential flow theory is a method that assumes an incompressible, inviscid and irrotational flow. This theory defines a potential function $\Phi(x, z, t)$ that is continuous and satisfies both the conservation of mass and momentum with the previously stated assumptions. Potential flow theory can be used to quickly model several types of flows where viscous effects are primarily limited to the boundary layer. In the case of a total temperature probe mounted in a symmetric airfoil or strut at zero degrees angle of attack, potential flow can provide a good estimation for the flow-field around the stagnation region of the strut. The predicted flow-field can then be used to identify the local flow velocity near the tip of the temperature sensor. Specifically, a Rankine half-body can be used to estimate the flow field around a symmetric strut with a given thickness.

A Rankine half-body utilizes the principle of superposition to combine the potential flow solutions for a uniform flow and a source flow. The combination of these solutions results in a flow representative of a freestream flow over a symmetric strut. When creating a Rankine half-body there are two important parameters that can be set. The first is the speed of the uniform flow and the second is the strength of the source. These two terms directly set a non-dimensional size of the strut and velocity of the freestream flow. From this solution, the location of the tip of a total temperature probe can be determined based on the L/t parameter describing the length of the probe relative to the thickness of the airfoil. A virtual probe velocity can then be identified based on the location where the probe tip would be within the potential flow-field solution. Note that this is called a virtual probe velocity since the probe itself is not modeled in in the Rankine half body solution. This assumes that the mounting strut has a significantly larger effect on the flow-field velocity than the probe. A Rankine half-body flow-field solution along with an illustrated virtual probe position can be seen in Figure 2.1. The identified virtual probe velocity can then be used as the local velocity for the recovery factor in Equation 2.1. This process was utilized in a MATLAB script that can be used to quickly solve for the aerodynamic error of a total temperature sensor in the presence of mount interference.

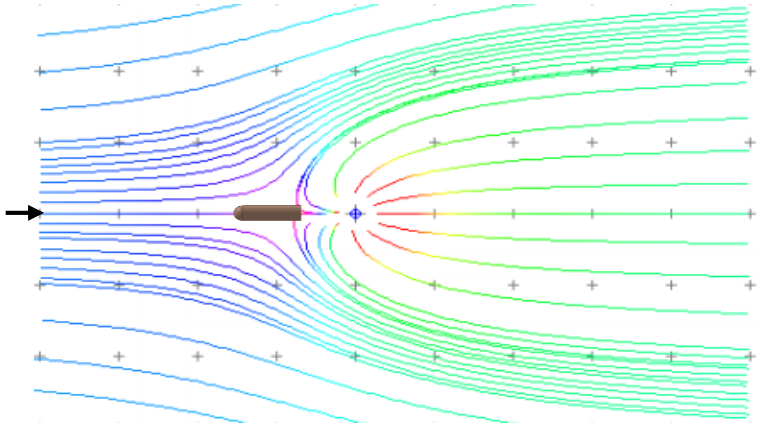

Figure 2.1: Rankine half-body flow-field and an illustrated virtual probe position

Potential flow theory is a very useful tool to quickly identify a probe's local flow velocity in the presence of mount interference; however, the assumptions used in simple potential flow limit its use to flows that are incompressible, irrotational and attached. Since velocity error becomes a primary concern for total temperature probes in high-speed flows, a compressibility correction is required to extend the local velocity prediction method to compressible flow regimes. The Prandtl-Glauert transformation or Karmam-Tsien rule can be utilized to transform an incompressible potential flow solution for use in a compressible flow regime. The Prandtl-Glauert transformation provides a compressible pressure coefficient that is equal to the incompressible pressure coefficient divided by the Prandtl-Glauert factor seen in Equation 2.2 for two-dimensional flows.

$$\beta = \sqrt{1 - {M_\infty}^2} \tag{2.2}$$

Similarly, the Karman-Tsien rule provides a compressible pressure coefficient correction seen in Equation 2.3.

$$C_p = \frac{C_{p,0}}{\sqrt{1-{M_\infty}^2+\left[\frac{{M_\infty}^2}{1+\sqrt{1-{M_\infty}^2}}\right]\frac{C_{p,0}}{2}}} \tag{2.3}$$

These compressibility corrections result in an increased virtual probe velocity compared to the original incompressible predictions. These compressibility corrections extend the use of simple potential flow predictions up to freestream Mach 0.7 flows when transonic effects begin to occur. The outlined method of utilizing potential flow theory to identify a virtual probe velocity for use in the recovery factor equation is useful for any low angle flow around a symmetric strut, but is still limited to attached flow. The application of this virtual probe method can be greatly extended by using a 2D, CFD simulation to identify the local flow conditions at the probe's location. With a 2D simulation, the local flow angle can be identified to determine the needed aerodynamic recovery factor α, and the local flow velocity at the probe tip can be utilized for calculating the local Mach number. Performing a 2D, CFD simulation takes considerably more time than an analytical calculation, but is still relatively quick and expands the application of the virtual probe prediction method to struts with trailing edge separation, camber, and higher freestream flow angles.

2.2 General Conduction Error Models

The conduction error of a total temperature probe is considerably more complex to model and predict than aerodynamic error. This is primarily due to the fact that conduction error results from a heat transfer balance between conduction and convection along the sensor. Much previous work has been done to predict conduction error by modeling the thermocouple as a 1-dimensional pin fin [8,11-12,24,31]. Though both conduction and convection are three-dimensional, their effects on a total temperature sensor can typically be modeled by assuming the sensor is quasi-one-dimensional along its length. This quasi-one-dimensional assumption generally holds true as long as the Biot number is much less than 1. Therefore, the Biot number along with several other important parameters need to be defined for the following discussion. The Biot number is a nondimensional value that is described in Equation 2.4 and provides a ratio of a body's internal heat transfer resistance versus its surface heat transfer resistance.

$$Bi = \frac{hL}{k_{tc}} \tag{2.4}$$

In Equation 2.4, L is the characteristic length, h is the average convection heat transfer coefficient over the probe's surface, and k_{tc} is an effective thermal conductivity of the probe. The characteristic length for the Biot number is determined by the ratio of the volume to surface area for a three-dimensional body or the ratio of the area to perimeter for a two-dimensional object. Modeling the sheathed thermocouple as a circular cylinder would result in a characteristic length of d/4 for a Biot number calculation. The Reynolds number is another important nondimensional parameter shown in Equation 2.5 which describes the ratio of inertial forces to viscous forces in a fluid flow and uses freestream flow properties at the fluid's total temperature.

$$Re = \frac{\rho U d_{tc}}{\mu} \tag{2.5}$$

In Equation 2.5, ρ is the fluid density, U is the freestream flow velocity, d_{tc} is the diameter of the probe, and μ is the dynamic viscosity of the freestream fluid. Finally, the Nusselt number is a crucial nondimensional parameter when discussing conduction error because it represents the ratio of convective to conductive heat transfer normal to the probe surface. The Nusselt number can be seen in Equation 2.6.

$$Nu = \frac{h d_{tc}}{k_{fluid}} \tag{2.6}$$

A simple solution for the conduction error of a one-dimensional pin fin was presented in Equation 1.11. In most applications, the geometry and freestream flow conditions would be known which results in, h, being the primary unknown needed to determine a total temperature sensors conduction error. One method for predicting, h, is to use an empirical correlation between the Nusselt number and Reynolds number such as Equation 2.7 presented by Moffat [8] for wires in a parallel flow. This correlation was developed from experimental data of bare wire thermocouples in parallel flow at Reynolds numbers between 100 and 10,000. Substituting Equation 2.6 into Equation 2.7 results in Equation 2.8 which can be used to estimate a total lumped, h, for a total temperature sensor.

$$Nu = (0.085 \pm 0.009)Re^{0.674} \tag{2.7}$$

$$h = 0.085\frac{k_{fluid}}{d_{tc}}Re^{0.674} \tag{2.8}$$

This should be a good approximation when, *h*, along the probe's surface is relatively constant or if the majority of probe's volume is lumped together near the junction and experiences a high, *h*, such as with a beaded bare wire thermocouple. The convective heat transfer coefficient from Equation 2.8 can now be substituted back into Equation 1.11 to form Equation 2.9. The numerator of Equation 2.9 is an important nondimensional term known as the conduction driver θ as seen in Equation 2.10.

$$E_c = 1 - \frac{T_j}{T_t} = \frac{\frac{T_t - T_b}{T_t}}{\cosh(2\frac{L}{d_{tc}}\sqrt{0.085\frac{k_{fluid}}{k_{tc}}Re^{0.337}})} \tag{2.9}$$

$$\theta = \frac{T_t - T_b}{T_t} \tag{2.10}$$

Equation 2.9 directly shows that a sensors conduction error or recovery is a function of four nondimensional ratios: θ, L/d_{tc}, k_{fluid}/k_{tc}, and the Reynolds number. This can be reduced to 3 nondimensional parameters by reformulating the thermal conductivity ratio. Equation 2.6 shows a relationship between k_{fluid} and the Nusselt number while Equation 2.4 shows a relationship between the k_{tc} and the Biot number. These two equations can be rearranged and substituted into the thermal conductivity ratio to form Equation 2.11 below. The Biot number can then be solved for in Equation 2.11 and reformulated in terms of the thermal conductivity ratio and the Reynolds number as expressed in Equation 2.12.

$$\frac{k_{fluid}}{k_{tc}} = \frac{h_c d_{tc}/Nu}{h_c d_{tc}/4Bi} = \frac{4Bi}{Nu} \tag{2.11}$$

$$Bi = 0.085\frac{k_{fluid}}{k_{tc}}\frac{Re^{0.674}}{4} \tag{2.12}$$

It can be seen that this new Biot number formulation is equivalent to a large portion of the hyperbolic cosine argument in Equation 2.9. Therefore, the Biot number can be substituted in to form Equation 2.13.

$$E_c = 1 - \frac{T_j}{T_t} = \frac{\frac{T_t - T_b}{T_t}}{\cosh(4\frac{L}{d_{tc}}\sqrt{Bi})} \tag{2.13}$$

Equation 2.13 provides an analytical expression to calculate a sensors conduction error or recovery based on three nondimensional parameters θ, L/d_{TC}, and the Biot number. Note that this is one more parameter than is needed to model aerodynamic error, and that the probe geometry, flow conditions, and conduction driver must all be considered when comparing conduction error predictions. However, the numerator in Equation 2.13 can be moved to the other side to form the conduction sensitivity parameter seen in Equation 2.14.

$$C.S. = \frac{T_t - T_j}{T_t - T_b} = \frac{1-R}{\theta} = \frac{1}{\cosh(4\frac{L}{d_{tc}}\sqrt{Bi})} \tag{2.14}$$

The conduction sensitivity parameter is dependent only on the probe geometry and the Biot number which means no known temperatures are needed. Therefore, this parameter can be used to collapse a sensor's recovery for any known conduction driver. This conduction driver independence is powerful for nondimensional scaling of experiments as it means only Reynolds number and probe geometry must be matched to compare different experiments or experimental results to predictions.

There are other models that could be used when attempting to model conduction error of a total temperature sensor. One such model is the thermal resistance model which uses an electrical circuit analogy to model the sensor [21]. In this model, a temperature difference is analogous to a potential difference and the rate of heat flow can be treated as an electrical current. However, the thermal resistance model utilizes physic similar to the described Moffat model through the use of a Nusselt-Reynolds correlation to predict the convective heat transfer coefficient, *h*. Though the thermal resistance model could be an effective way to model conduction error, it will not be considered or utilized in the following work.

2.3 Enhanced Conduction Error Models

The low-order model that was discussed in Section 2.2 and presented by Moffat [8] provides a simple way to model conduction error for a total temperature sensor. However, this model makes several assumptions that greatly limit the application and accuracy of that low-order model. Equation 1.11 assumes that $(dT/dx)_{x=L} = 0$ which is representative of a thermocouple with an insulated tip, but would not be accurate for a bare wire or grounded probe. Without the insulated tip assumption, Equation 1.11 can be rederived from the linear ODE in Equation 2.15 to produce the conduction error equation seen in Equation 2.16. Equation 2.16 takes the same form as Equation 1.11 but features an additional hyperbolic sine term in the denominator which is a result of allowing a nonzero $(dT/dx)_{x=L}$ [11]. Similar to the Moffat formulation, this conduction error formula can be easily rewritten to form the conduction sensitivity parameter seen in Equation 2.17.

$$\frac{d^2T}{dx^2} = \frac{hP}{kA}[T(x) - T_f] \tag{2.15}$$

$$E_c = 1 - \frac{T_j}{T_t} = \frac{\frac{T_t - T_b}{T_t}}{\cosh(L\sqrt{\frac{hP}{k_{tc}A}}) + \frac{h}{k_{tc}}\sqrt{\frac{k_{tc}A}{hP}}\sinh(L\sqrt{\frac{hP}{k_{tc}A}})} \tag{2.16}$$

$$C.S. = \frac{T_t - T_j}{T_t - T_b} = \frac{1}{\cosh(L\sqrt{\frac{hP}{k_{tc}A}}) + \sqrt{\frac{hA}{k_{tc}P}}\sinh(L\sqrt{\frac{hP}{k_{tc}A}})} \tag{2.17}$$

Another restrictive assumption is that Equation 1.11 assumes the convective film coefficient h is constant over the entire surface of the probe. This assumption is almost never true in real applications, but can provide an estimate for some simple geometry probes in a crossflow. One

approach to improving this assumption would be to allow, *h*, to vary along the probe length, but assume that it is constant over each cross section. The results of this assumption were discussed and implemented in Schetz et al (2016) and Vincent et al (2017) [11,12]. This method requires a numerical approach to model the conduction error of a sensor, but is significantly more accurate than the initial constant-*h* assumption and allows more complex probe geometries and flow interactions to be modeled. A third approach is to acknowledge $h_{tip} > h_{side}$, but to assume after the tip the convective film coefficient, *h*, is constant along the side of the probe [11]. This results in the conduction error formula shown in Equation 2.18.

$$E_c = 1 - \frac{T_j}{T_t} = \frac{\frac{T_t - T_b}{T_t}}{\cosh(L\sqrt{\frac{h_{side}P}{k_{tc}A}}) + \frac{h_{tip}}{k_{tc}}\sqrt{\frac{k_{tc}A}{h_{side}P}}\sinh(L\sqrt{\frac{h_{side}P}{k_{tc}A}})} \tag{2.18}$$

For this approach, h_{tip} is representative of an average film coefficient over the semi-sphere tip of a sheathed thermocouple while h_{side} represents an average film coefficient along the length of the probe behind the tip. This assumption will not be quite as accurate as the numerical approach, but will keep the low-order model for conduction error analytical while improving fidelity over the original constant h assumption.

A complication of using the form of the conduction error equation found in Equation 2.18 is how to determine h_{tip} and h_{side}. If the freestream Reynolds number is used as described in the Moffat model, the tip and side convective film coefficients will be predicted to be the same. Also, the Nusselt-Reynolds correlation presented in Equation 2.7 was developed based on lumped, *h*, results for beaded, bare-wire probes, therefore it will not represent the same flow physics that would occur separately on the tip and side of a sheathed thermocouple. There are several other Nusselt-Reynolds correlations that have been presented in previous literature. Two important correlations to note are Equation 2.19 and Equation 2.20.

$$Nu = (0.44 \pm 0.06)Re^{0.50} \tag{2.19}$$

$$Nu = 0.3 + \frac{0.62{Re_d}^{0.5}Pr^{1/3}}{[1+(0.4Pr)^{2/3}]^{0.25}}[1 + (\frac{Re_d}{282{,}000})^{5/8}]^{0.8} \tag{2.20}$$

Equation 2.19 was presented by Moffat [8] and developed for bare wire thermocouples positioned normal to the flow. Meanwhile, Equation 2.20 was presented by Churchill and Bernstein and was developed for cylinders in a crossflow [43]. Both of these correlations could be utilized in the prediction of conduction error for specific thermocouple configurations. However, both correlations predict a lumped, *h*, and were not developed to capture separate flow physics that occur on the tip and side of a sheathed thermocouple. Therefore, two new Nusselt-Reynolds correlations would need to be developed to properly utilize Equation 2.18.

Two other significant limitations of the conduction error models presented in the above sections is their inability to model recovery change with flow angle and inability to account for mount interference when a small, total temperature sensor is mounted on a strut. Mount interference effects and their impact on the flow around a sensor were previously discussed in Section 1.6 and Section 2.1. A method was presented called the virtual probe method which is used to account for

the impact of the strut on the local flow field around a sensor. This virtual probe method can be similarly applied to any of the discussed conduction models to determine a local Reynolds number that accounts for mount interference to be used with a Nusselt-Reynolds correlation. The process of doing this would be to calculate a potential flow, panel method, or 2D, CFD solution for the flow field around the desired strut. Then extract a velocity profile line at the location that the total temperature sensor would be positioned within the flow-field. An example 2D, CFD solution and virtual probe velocity line can be seen in Figure 2.2.

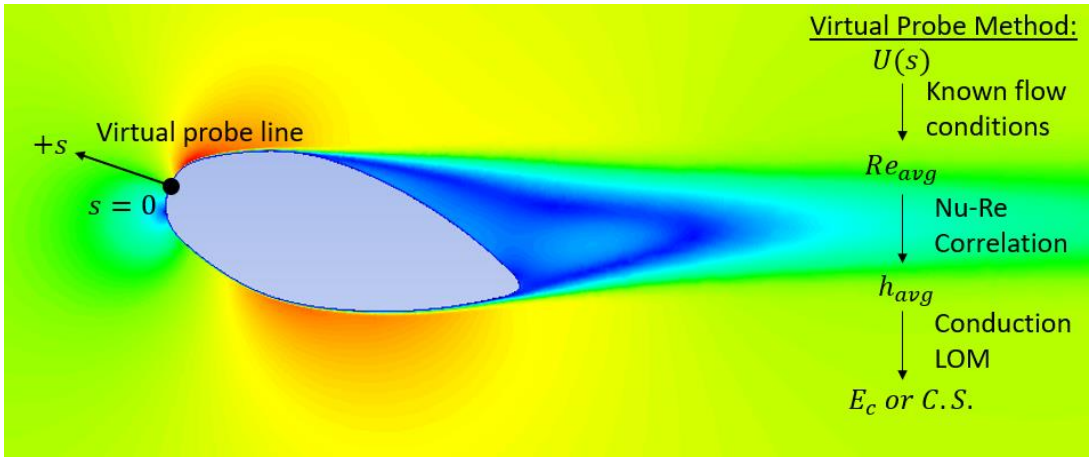

Figure 2.2: Virtual probe method with example flow-field and virtual probe line

For the conduction models that use an average convective film coefficient, *h*, the extracted velocity along the sensor length can be averaged and used to calculate a local Reynolds number. This local Reynolds number can then be used with an appropriate Nusselt-Reynolds correlation to determine the corresponding, *h*, value which can finally be input into the conduction error models shown in Equation 1.11 or Equation 2.16. This paper will attempt to prove that the change in local Reynolds number captures the majority of both mount interference effects and changes in the freestream flow angle. Therefore, by using the virtual probe method to acquire a local Reynolds number instead of the freestream Reynolds number, sensor performance variation due to both mount interference and freestream flow angle can be accounted for. This claim will be further discussed in Chapter 5.

3 Computational Modeling Methods

Computational Fluid Dynamics (CFD) simulations were performed to provide flow visualizations and help identify the physics causing different flow behaviors. The computational simulations presented in this work were performed using the commercial finite volume CFD/CHT code ANSYS Fluent. In order to computationally model a viscous fluid flow, governing equations known as the Navier-Stokes equations must be solved. The Navier-Stokes equations are derived from the laws of conservation of mass, conservation of momentum, and conservation of energy for a fluid flow and can be written in a differential or integral form. The governing equations that were used for this study were a simplification of the Navier-Stokes equations known as the Reynolds-averaged Navier-Stokes (RANS) equations. These equations neglect instantaneous turbulent fluctuations by taking a time average of the original Navier-Stokes equations [19]. This results in additional unknown stress terms in the momentum and energy equations that require an extra model for turbulent Reynolds stresses. However, the RANS governing equations result in a set of equations that are simpler to solve and can provide accurate steady-state time averaged solutions.

During the computational modeling used for this work, the flow was assumed to be turbulent and experimental conditions were matched whenever possible. The $k-\omega$ shear stress transport (SST) turbulence model was used for all calculations. This model can be utilized in a variety of applications and is a useful model for boundary layer flows since it uses a two-equation model which can treat near wall and freestream flows differently. The $k-\omega$ SST model uses a $k-\varepsilon$ model for regions that are far from walls and uses a $k-\omega$ model equation for near wall regions. A transition function is then utilized to ensure the correct equations are used in the appropriate regions [44].

Steady, planar simulations were performed to acquire the needed velocity flow-field around at strut to be used in low-order predictions using the virtual probe method. These computations did not model the total temperature sensor, but simulated the flow around the experimental strut by modeling the strut geometry as a stationary wall with standard roughness and a no-slip boundary condition. The strut geometry was acquired by tracing the experimental strut, and then a spline was utilized to create a CAD file of the strut geometry. Additionally, a density-based solver was used with velocity inlet and pressure outlet boundary conditions. The inlet velocity was set to match the experiments 12.6 m/s, and all pressure boundary conditions were set to match an average total pressure during experimental testing of 945 mbar. Pressure far-field boundary conditions were used for the top and bottom boundaries with the same total pressure and a Mach number of 0.038 which corresponded to the 12.6 m/s flow velocity. Finally, a turbulence viscosity ratio of 1, and a turbulence intensity ratio of 1% was used, which was expected to be representative of conditions in the Virginia Tech Open Jet Wind Tunnel.

The steady planar simulations utilized a hybrid grid with 2D, triangular mesh elements for the majority of the domain while rectangular elements where used to resolve the boundary layer. The meshes for the steady planar simulations generally consisted of around 100,000 elements, and an example mesh can be seen in Figure 3.1. Figure 3.1 shows the meshing of the full fluid domain

that was modeled as well as zoomed in images of the meshing around the strut body and the boundary layer resolution. For each simulation, profiles of the dimensionless wall y+ value was confirmed to be 1.0 or less to ensure the boundary layer was properly resolved.

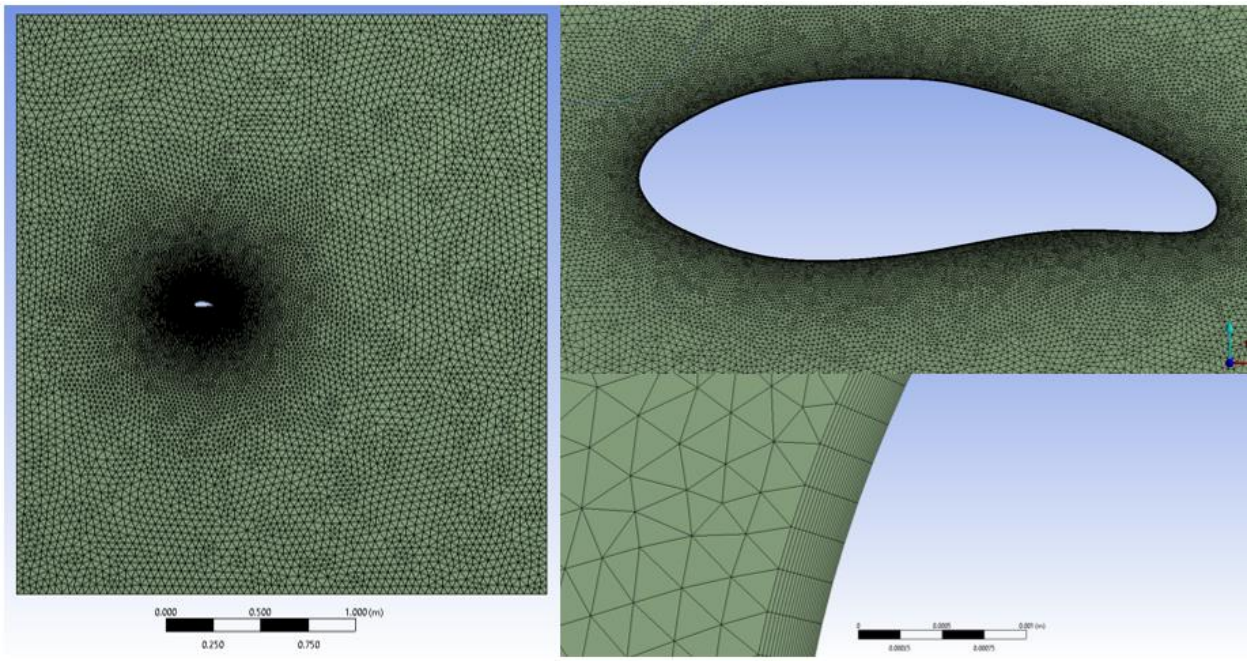

Figure 3.1: 2D mesh for modeling the flow-field around cambered strut

3D, CFD/CHT simulations were also performed using a hybrid grid with tetrahedron volume elements for the majority of the domain and a prism layer to resolve the boundary layer. The steady, 3D simulations utilized the same solver, boundary conditions, and turbulence model that were described for the planar simulations. However, the total temperature probe was also modeled within these simulations. The geometry of the total temperature probe was accurately modeled, but the probe was assumed to be a single material with properties similar to 304 stainless-steel except for a reduced thermal conductivity of 9.0 W/mK.

The reduced thermal conductivity of 9.0 W/mK was used to account for the effective thermal conductivity of the physical probe containing thermocouple wires and insulating magnesium oxide powder. This effective thermal conductivity was determined using an area weighted average of each material within a sheathed Type E thermocouple. The internal dimensions of the sheathed thermocouple were provided by Omega, the thermocouple supplier. The 304 stainless steel sheath was determined to make up 51% of the thermocouples area and have a thermal conductivity of 14.4 W/mK. Meanwhile, the thermocouple wires were found to make up 8% of the total probe area and had an average thermal conductivity of 19.25 W/mK. Finally, the magnesium oxide powder was determined to occupy 41% of the probe area. The thermal conductivity of the magnesium oxide powder was estimated using information from Godbee et al (1965) [47]. MgO (E-98) was assumed with a 0.64 volume fraction and an average probe temperature of 50 C to estimate a MgO powder thermal conductivity of 0.6 W/mK. This thermal conductivity is significantly lower than solid magnesium, but should be representative of the powdered form

utilized in the tested sheathed temperature probes. The full heat transfer interaction between the flow and sensor was modeled in these simulations and a temperature boundary condition was utilized at the base of the sensor to set a conduction driver comparable to that induced in the conduction error experiments. Additional details regarding effective techniques for meshing and ANSYS Fluent setup can be found in Schneider et al (2015) and Reardon et al (2017) [45,46]. An analysis cannot be confidently utilized unless it is tested against experimental data. Experimental studies for assessing the analyses presented are the subject of the next chapter.

4 Experimental Setup, Instrumentation, and Methods

Numerous total temperature probe geometries were experimentally tested to gain information about how freestream flow angle and mount interference impact sensor aerodynamic and conduction errors. These experimental results were also utilized to validate the developed low-order methods previously discussed. The following section will discuss the facilities, instrumentation, total temperature sensor assembly, geometries tested, flow conditions tested, and the testing procedures used during the performed experiments. First, the aerodynamic error experiment will be discussed which were all performed using the Virginia Tech Hot Jet facility. Next, the conduction error experiments will be discussed which were performed in the Virginia Tech Open Wind Tunnel facility. After discussing the facilities and experimental setup, the post processing procedure will be described in depth for both sets of experiments.

4.1 Virginia Tech Heated Jet Rig

The facility utilized for the experimental study of aerodynamic error was the Virginia Tech Hot Jet. The purpose of this study was to validate the analytical methodology named the virtual probe method (VPM) presented in Section 2.1. The Virginia Tech Hot Jet is located at the Advanced Power and Propulsion Lab in Blacksburg, and a diagram of the facility can be seen in Figure 4.1. This facility utilizes compressed air from a reciprocating compressor that pressurizes two reservoir tanks. A dryer is then used to remove moisture from the compressed air. This compressed air is supplied to an 8 in. plenum which features a Sylvania 192 kW Flanged Inline Heater, Model 073153 that is capable of heating the flow to above 700 F. However, the inline heater was not used for this study. The air in the plenum passes through a 4 in. contraction and through three 20x20 screens and a 16 CPSI honeycomb which is used to straighten the flow. Finally, the flow passes through a 2 in. contraction nozzle and exhausts into the ambient outdoor air. More details about the Virginia Tech Hot Jet facility can be found in Englerth et al [31]. A detailed diagram of the hot jet rig and the utilized 2 in. contraction nozzle can be seen in Figure 4.2.

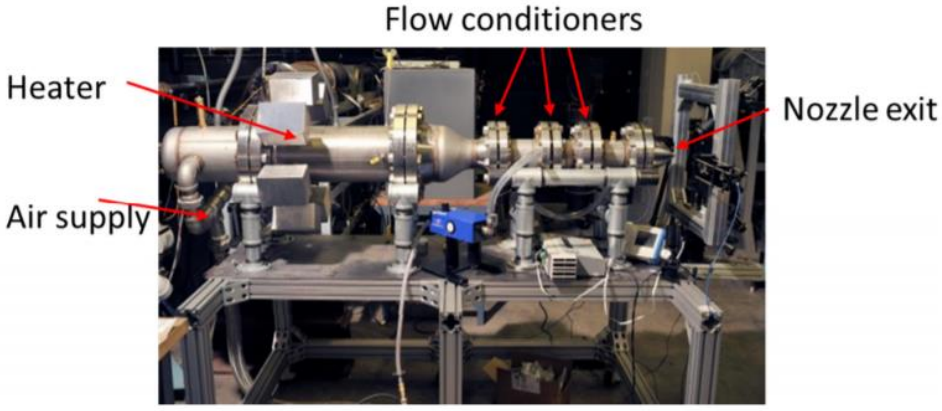

Figure 4.1: Virginia Tech Hot Jet Facility (from Ref. [31])

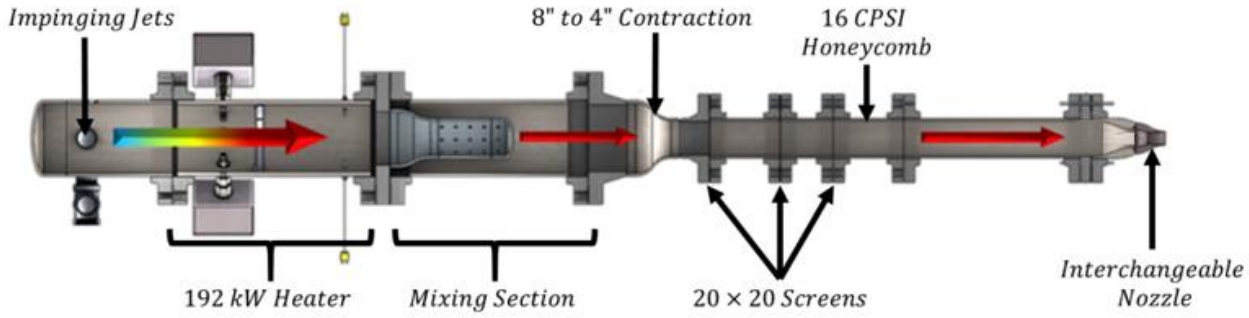

Figure 4.2: Detailed diagram of jet configuration

Pressure and temperature sensors were inserted into the 4 in. plenum upstream of the 2 in. contraction nozzle. A Pitot probe is used within the 4 in. plenum to measure the total pressure of the flow. This flow exits into ambient conditions which results in a static pressure equivalent to the local ambient pressure. This local ambient pressure was acquired from the Virginia Tech airport at https://w1.weather.gov/data/obhistory/KBCB.html. The known static and total pressures can then be used to calculate the exit flow Mach number using the isentropic flow relationship shown in Equation 4.1.

$$\frac{P_s}{P_t} = (1 + \frac{\gamma-1}{2} M^2)^{\frac{-\gamma}{\gamma-1}} \tag{4.1}$$

A total temperature sensor designed for ambient temperature conditions and high velocities was inserted into the 4 in. plenum to measure the total temperature of the flow. The thermocouple used in the total temperature sensor was a grounded, sheathed type K with a stainless-steel sheath and a 0.040” outer diameter. A diagram of the total temperature sensor used can be seen in Figure 4.3.

Figure 4.3: Plenum total temperature sensor

Type K thermocouples are composed of Chromel and Alumel wires. The positive leg of the thermocouple is the Chromel wire which is composed of 90% nickel and 10% of a chromium alloy. Meanwhile, the negative leg of the thermocouple is the Alumel wire which is composed of 95% nickel, 2% aluminum, 2% manganese, and 1% silicon alloy. The voltages from the plenum total temperature sensor and the thermocouples tested within the experiment were measured using a National Instrument NI-9213 c-series temperature module mounted within a NI DAQ-9184 chassis. This instrumentation is capable of a maximum sample rate of 75 samples per second and can acquire 16 simultaneous, high speed voltage measurements with channels separated by a 250 Vrms Ch-Earth ground isolation. The voltage measurements from the data acquisition system were recorded and processed on an NI PXIe-8133 embedded controller running Windows 7 using a developed LabView code. Finally, a Scanivalve Corp. Z0C17IP/8Px-APC pressure transducer was

used to acquire pressure data from the pitot probe. The experimental rig has been described in other literature which can be found in References [14,15].

A simple mount assembly for the nozzle was adapted to be used with the hot jet facility. The nozzle mount is made of a 4.5 in. shaft collar, 8 in. stainless steel struts, and a 3D-printed circular cross-member that holds the instrumented strut. This nozzle mount design was favorable, because the base unit has been used in previous experiments and shown to allow repeatable probe positioning at zero degrees angle of attack even as the facility moves under thermal loading. The 3D-printed circular cross-member is used for a fast, low-fidelity approach to retrofit the strut to the existing nozzle mount. Additionally, the nozzle mount can be easily rotated or shifted along the nozzle axis which allows different distances from the nozzle exit plane to be tested.

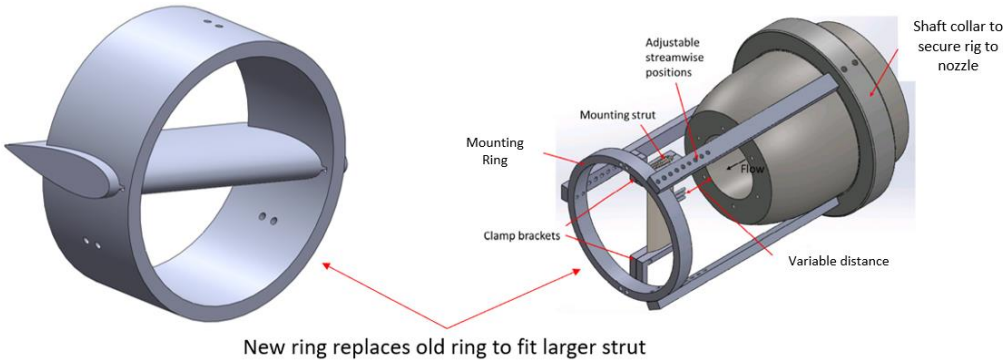

Figure 4.4: Diagram of nozzle mount for sensor assembly

4.2 Velocity Error Experiment – Sensor Assembly and Procedure

The strut that was used in the hot jet aerodynamic error experiments featured a NACA 0024 profile which can be seen below in Figure 4.5.

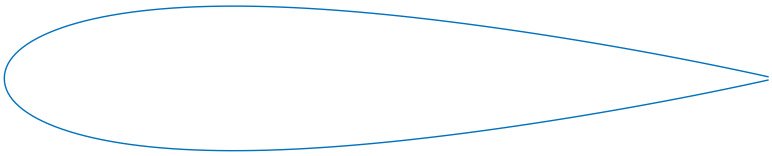

Figure 4.5: NACA 0024 airfoil profile

The strut was 3D-printed from polylactic acid (PLA) material which provided a thermal conductivity value of 0.13 W/(m*K) around ambient temperatures. This low thermal conductivity was ideal for mitigating conduction effects between the strut and probe so that aerodynamic error could be isolated. Since no cooling flow is used and the thermal conductivity of the strut is low, the conduction driver of the probe is very small; therefore, sensor predictions ignoring conduction error should be comparable to the experiment results. Small holes were drilled into the center of the leading edge of the strut near the center span location. A section of the strut was designed with a hollow cavity behind the leading edge so that the temperature probes could be fed through the

tips of the strut outside of the jet test section and out through the strut leading edge holes. Therefore, all of the tested thermocouples were positioned along the centerline of the symmetric strut. A four-hole ceramic tube was used to house, align, and further insulate the thermocouples to mitigate conduction effects. The ceramic tube is positioned so that its end aligns flush with the strut leading edge, while the tested thermocouples extend out into the flow from the ceramic tube. The thermocouple positioning and strut internal assembly can be seen in Figure 4.6.

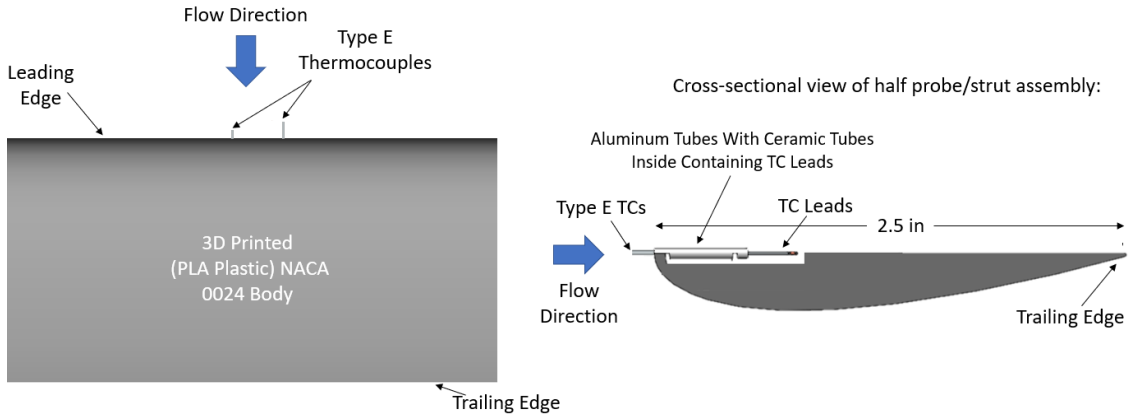

Figure 4.6: Sensor assembly for aerodynamic error experiment

After being printed, the strut was sanded to get rid of major ridges caused by the layering of the PLA plastic. The outside surface of the strut was then painted with a thin, even coat of black paint, and then the sanding process was repeated. This cycle was performed several times until the strut surface was sufficiently smooth. Ensuring a smooth strut surface was done to minimize the chance of early flow transition or flow separation caused by the surface roughness. This was needed to produce a flow-field in the experiments that would be similar to 2D, CFD or potential flow predictions so that the experimental results could be compared to the low order model predictions. Additionally, painting the strut ensured the 3D-printed strut was sealed. Constantly sanding and painting the strut surface guaranteed any air gaps or small holes that were introduced during the 3D printing process would be sealed so that no airflow could circulate through the strut.

Three different thermocouples were tested during this experiment. Two sheathed, type E thermocouples were tested and one beaded, bare wire type E thermocouple was tested. A type E thermocouple is made of Chromel and Constantan wires. The positive leg of the thermocouple is the Chromel wire which is composed of 90% nickel and 10% of a chromium alloy. Meanwhile, the Constantan wire serves as the negative leg of the thermocouple and is composed of 55% copper and 45% nickel. Type E thermocouples were selected for their high sensitivity and accuracy around the ambient temperatures that were measured during testing. Both sheathed probes had an outer diameter of 0.010 inches. The thermocouples were positioned using the length over diameter non-dimensional parameter usually written as *L/d*. One sheathed thermocouple was positioned with an L/d of 9 (L/t of 0.15) while the other was positioned with an L/d of 4 (L/t of 0.067). The same diameter probe positioned at different L/t values was used to test the varying amounts of strut interference. The maximum thickness of the mounting strut, *t*, was utilized in the L/t parameter to determine the location of flow-field conditions local to the sensor to be used with the virtual probe, low-order method. The positioning of both sheathed probes can be seen in the left side of Figure

4.6. Finally, the beaded, bare-wire probe that was tested featured a bead diameter of 0.010” and a wire diameter of 0.003”. The tip of the beaded, bare-wire probe was positioned 0.035” away from the leading edge of the strut and the geometry of the thermocouple in the four-hole ceramic tube can be seen below in Figure 4.7.

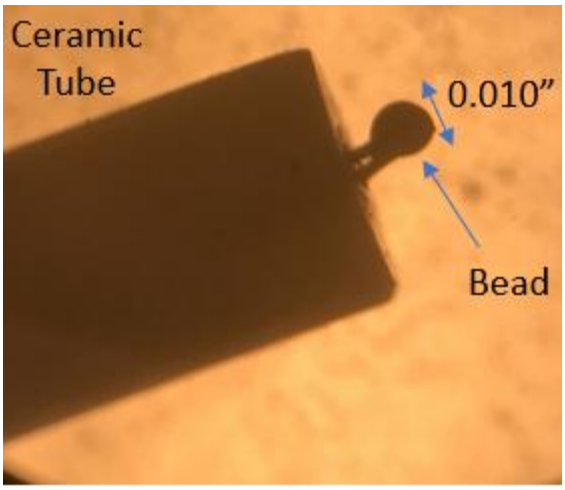

Figure 4.7: Beaded, bare wire thermocouple in ceramic tube

The procedure for the hot jet aerodynamic error experiments will be outlined below. First, the jet is started to produce a nozzle exit Mach number of around 0.5. The hot jet is allowed to run at the Mach number for around 30 minutes to an hour without data acquisition so that the total temperature of the flow can stabilize. It takes a significant amount of time for the pipes, jet, and strut to reach equilibrium. Additionally, the compressor and reservoir tanks are located outside and are subject to temperature changes as they deplete, especially around sunrise or sunset. The aerodynamic error experiments were performed primarily at night or in the afternoon when the ambient air temperature was relatively constant. During the first several minutes of operating the jet the total temperature will either rise or fall slowly which will subsequently change the measured temperatures of the tested sensors. After the jet and flow total temperature have stabilized, a Mach sweep is performed. The Mach number is decreased to 0.25 and then increased to Mach 0.65 in increments of 0.1 while maxing out at Mach 0.72. At each Mach number, the jet and sensor assembly are given two minutes to come to steady equilibrium and then five minutes of data was recorded at 75 samples per second. The probe-based Reynolds number throughout the Mach sweep ranges from 1400 to 4000 using the diameter as the characteristic length. The Mach sweep was performed to analyze the effects of mount interference over a range of Mach numbers that include flow compressibility effects near the mount.

The data was acquired as a raw voltage signal. The thermocouple calibration correlation was then used to convert the measured voltage into a temperature. These results are acquired, converted, and saved using a LabView code, and then exported to Matlab for post processing. The temperature results at each individual Mach number are averaged over the five minutes of recorded data. Then, the measured temperatures can be used to calculate the sensor recovery factor. This post-processing provides one probe performance value for each Mach number. These time-averaged

recovery values at each Mach number provide an accurate way to assess aerodynamic error while minimizing the effects of small Mach number oscillations and signal noise.

A correction/calibration was also made in post-processing to each of the three tested probes used in this experiment. Each of the three tested probes and the plenum total temperature sensor were placed in a sealed container and allowed to come to steady state. The measured temperature of each thermocouple was then recorded for several hours. The plenum total temperature probe measurement was taken as the true ambient temperature, and the difference between each tested probe and the plenum total temperature probe were taken. These delta temperature values were then applied as a correction to the results of each tested probe in post processing to improve accuracy.

4.3 Experimental Methods for Inducing & Measuring Conduction Error

To induce a conduction error within an experiment, a temperature gradient is needed along the total temperature probe. It can be challenging to experimentally identify the magnitude of a sensor's conduction error. This is because in most applications or even experimental setups, other error sources will be present in addition to conduction error. Flow over the sensor will always result in an aerodynamic error, and heat sources used to induce a conduction error will inherently also produce radiation. However, conduction error can be measured and studied experimentally by minimizing aerodynamic and radiation error, while intentionally producing a large conduction error. This could be done by designing an experiment with low local flow velocities, a large temperature gradient along the sensor, and poor view factors combined with radiation shields between heat sources and the tested sensors junction. This type of setup would allow influences by aerodynamic error and radiation error to be minimized so that the effects of conduction error can be directly measured.

With an ideal conduction experiment environment, conduction error of a sensor could be determined by directly measuring the sensors junction temperature and the total temperature of the flow. From these two temperature measurements, the sensor recovery can be calculated which can be used to identify the conduction error if all other error sources are assumed to negligible. However, this type of result provides little information about the conduction environment and cannot be compared to conduction error predictions such as those described in Equation 1.11 or Equation 2.16, because the experimental conduction driver is not known. Therefore, a third measured temperature is required to perform an effective conduction experiment. This third temperature is a base temperature measurement (T_b), and measures the temperature of the primary tested sensor at the location where the sensor and mount leading edge intersect.

While the concept of a base temperature measurement is simple, in an actual experiment setup physically measuring the correct base temperature can be a great challenge. The base temperature measurement must be obtained at the axial location of the mount leading edge for the conduction equations used in the described low-order models to be accurate. With the base temperature measurement taken at the strut leading edge, the entire exposed probe length of interest is subjected to convection from the flow-field. This results in a convective heat transfer coefficient, *h*, over the

entire probe length which is predicted by a Nusselt-Reynolds correlation like the example previously described in Equation 2.7. If the base temperature was measured further back into the strut, an additional model would be needed to predict the conduction behavior along the length of probe that is mounted within the strut. In theory, the base temperature could also be measured at a location along the sensor that is exposed to the flow. However, in real applications this would require a base temperature probe that is either so small that it does not impact the flow behavior and *h*, or a base measurement built into the primary sensor. Finally, the base probe must measure the actual probe temperature at the base location and not the mount temperature physically close to the base location. Film cooling from the flow interaction with the exposed portion of the probe will result in conduction along the probe that will typically create a probe temperature at the base location that is significantly different than the mount temperature. In conclusion, the base temperature must be experimentally measured at the strut leading edge and along the probe conduction path to acquire accurate results.

There are several ways to induce a temperature gradient needed for a conduction error experiment. Therefore, before performing conduction experiments, three different methods for inducing a conduction error were investigated. The first method, was to utilize an ambient temperature mount with a heated freestream flow. This method can be performed using a facility such as the Virginia Tech Hot Jet which features a jet capable of heating the freestream flow to high temperatures. The hot flow significantly heats the mount, but the mount can be cooled with ambient temperature water to hold the mount temperature near ambient and produce a high conduction driver for the tested total temperature sensors. The second method was to utilize an ambient temperature freestream flow with a chilled mount. An experiment using this method could be performed using any ambient temperature jet or wind tunnel and a mount chilled with cold ethyl alcohol. A system was designed and tested to investigate this method that utilized ethyl alcohol chilled with dry ice to reduce the mount temperature and produce a significant conduction driver. Finally, the third method is to utilize a heated mount with an ambient temperature freestream flow. This method will produce a negative conduction driver, and can be performed by using a heater within the mounting strut and an ambient temperature jet or wind tunnel. A diagram of the three investigated methods to induce a conduction error can be seen in Figure 4.8.

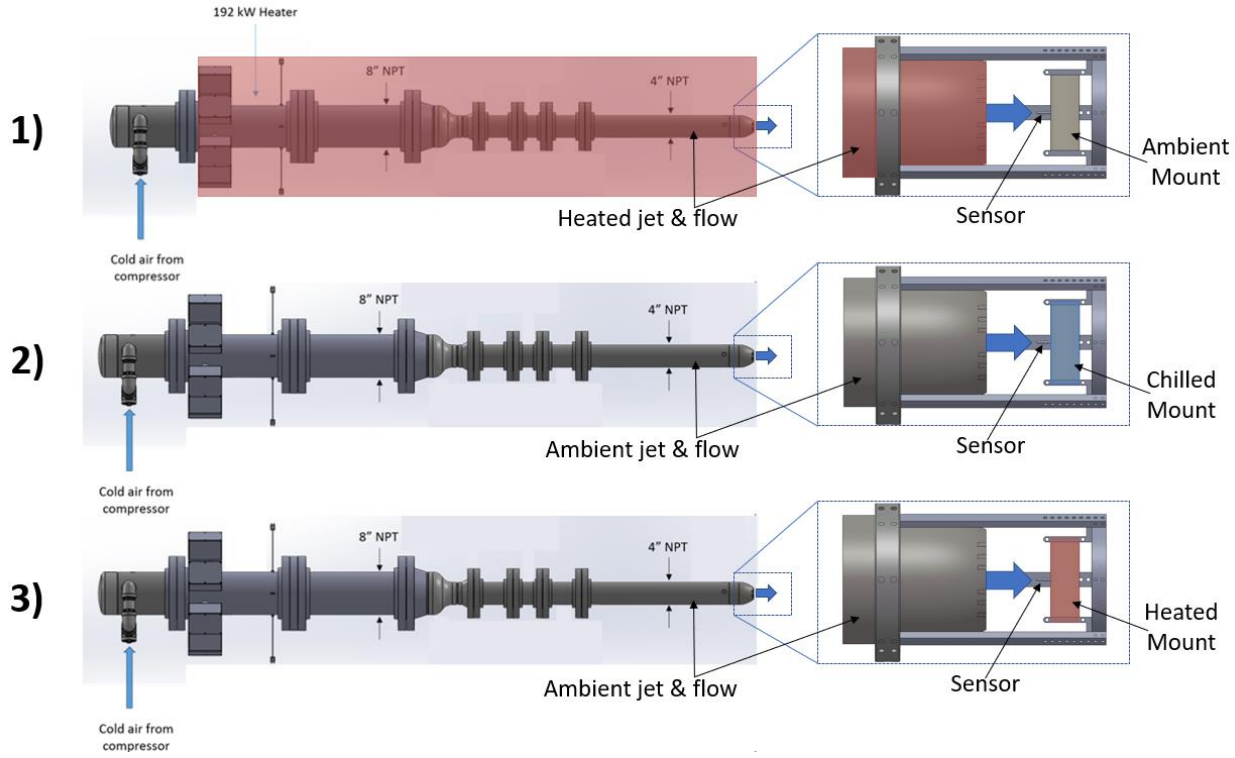

Figure 4.8: Methods to induce conduction error 1) Heated flow, 2) Chilled mount, 3) Heated mount

Each of the investigated methods serve as effective ways to produce a conduction error. However, each method had unique benefits and associated challenges. The heated flow method featured a simple way to produce a constant mount temperature and is physically the most similar to a gas-turbine application. Yet, test times with this method were extremely long due to the need for the heated flow and facility to come to a steady state. Also, it was challenging to produce a uniform heated freestream flow. The heated jet and facility needed to produce a heated freestream flow also produce significant amounts of radiation which interact with the tested sensor and is not ideal when attempting to measure isolated conduction error. The second method utilizing a chilled mount was found to mitigate many of the challenges faced with the first method. Since operating at lower temperatures, this method requires a smaller temperature difference between the base and junction measurements to produce significant conduction drivers. Also, the radiation impacts from the jet and surrounding facility are mitigated since they are now at ambient conditions. An ambient temperature uniform flow is more easily produced than a uniform heated flow, and the strut featured significantly less mass to bring to a steady state condition than the jet and facility. Therefore, test times were greatly reduced due to the thermal response of the strut being much faster than that of the jet and facility. One challenge of the chilled mount method was providing large reservoirs of chilled fluid to maintain a high conduction driver throughout testing. This chilled fluid loses a lot of temperature as it passes through the strut, and is more expensive to provide and chill than the ambient temperature water utilized in method one.

Finally, the third method combines many of the advantages of the first two described methods. The heated strut with an ambient temperature freestream flow mitigates the radiation concerns from the jet and facility. Meanwhile, utilizing an electric heater within the strut to produce a temperature gradient is cheap, and can be used to precisely control the conduction driver for an unlimited amount of time. The heater will need to reach high temperatures to produce significant driver values, but the heater can be designed so that it is primarily heating only the leads of the tested total temperature sensor and not the mounting strut. This allows the strut to act as a radiation shield for the exposed portion of the sensor from the heater. One unique result of this method is that it produces negative conduction drivers and a recovery value above one. However, use of the conduction sensitivity parameter seen in Equation 2.14 provides results that are independent of conduction driver and only dependent on probe geometry and flow conditions. This parameter provides an ideal way to analyze conduction error and allows results to be compared without matching conduction driver when the probe geometry and flow conditions are equivalent.

4.4 Virginia Tech Open Jet Wind Tunnel

The facility utilized for the present experimental study of conduction error was the Virginia Tech Open Jet Wind Tunnel. The purpose of this study was to gain insight into mount interference and freestream flow angle effects on sensor conduction error. Additionally, this study was performed to assess whether the virtual probe method described in Section 2.3 could be utilized with existing conduction-error models to account for the impacts of flow angle and mount interference. The Virginia Tech Open Jet Wind Tunnel is located in Goodwin Hall in Blacksburg, and a photograph of the facility can be seen in Figure 4.9.

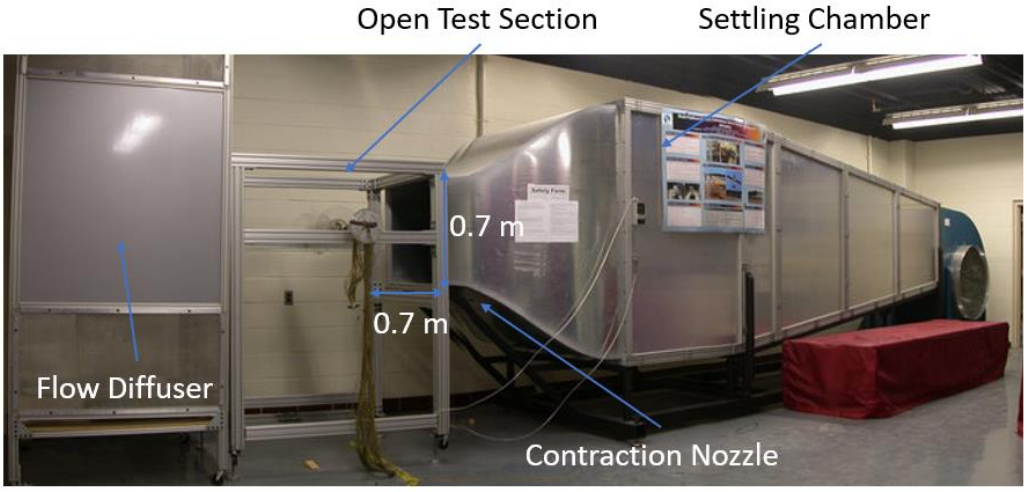

Figure 4.9: Virginia Tech Open Jet Wind Tunnel

The wind tunnel consists of a steel base, aluminum frame, and aluminum-composite panels that create the tunnel walls. A 30 hp BC-SW Size 365 Twin City centrifugal fan powers the wind tunnel and is capable of moving up to 15 m^3/sec of air. The flow is initially drawn in by the fan and then runs through a four-meter diffuser before being directed into a settling chamber of 1.47 meters by

1.78 meters. After the settling chamber, the flow travels through three turbulence-reducing screens and honeycomb which help make the flow uniform. Finally, the flow travels through a 5.5:1 contraction nozzle and exits into the tunnel test section. Downstream of the test section is a flow diffuser which contains several high-loss screens which help to reduce the velocity of the exit flow so that disturbance to ambient air within the lab is minimal. Two different test sections were used during the conduction error experiments. The first is the open test section where air is expelled into the lab room after the contraction nozzle with an exit height and width of 0.7 meters. The second is the closed test section which features a 27.75 in. by 27.75 in. test section area and is 48 inches in length. This large test section size was needed for off-angle testing so that results could be independent of the tunnel walls and so that the entire strut/sensor assembly could by surrounded by flow at high pitch angles. For off-angle testing, nearby tunnel walls or ambient stagnated flow, such as with a small diameter free jet, results in stagnation point shifts on the leading edge of the strut. Therefore, the large test section of the Goodwin wind tunnel was selected to avoid these leading-edge stagnation shifts. The closed test section features plexiglass wall panels and a rotary table mounted to the top of the test section which was used to pitch the strut for off-angle testing. The closed test section can be seen in Figure 4.10.

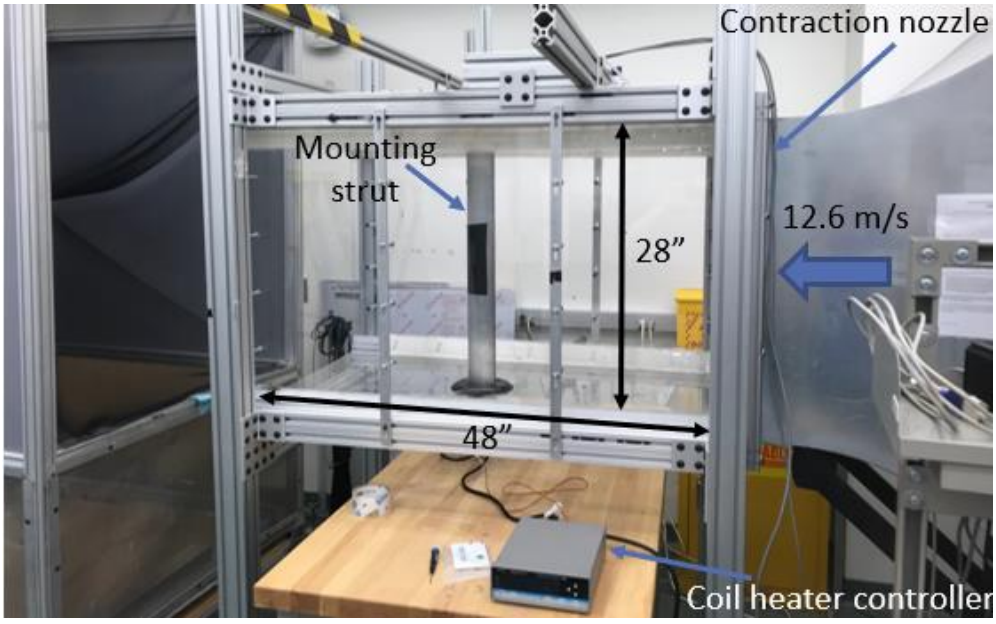

Figure 4.10: External view of Virginia Tech Open Jet Wind Tunnel closed test section

The utilized rotary table was a Vexta stepping motor, model PK266-03A. A 3D-printed mount was created and used to attach the strut to the motor. The 3D-printed mount is a circular cylinder with a centered hole matching the strut profile. This mount was designed to be able to screw into the stepping motor and secure the strut during off-angle testing. This stepping motor provided precise control of the strut pitch angle and provided the capability to perform pitch angle sweeps. Before the experiment, the mounting strut was geometrically aligned with the closed test section, and the Vexta motor was zeroed with that alignment. After initially zeroing the strut’s angle, the Vexta stepping motor allowed the pitch angle to be set within one degree of accuracy.

The flow velocity of the wind tunnel is controlled by an AF-600 General Electric variable frequency drive which has a maximum speed of 1180 RPMs. The maximum RPM setting corresponds to a flow velocity at the contraction nozzle exit of around 30 m/s. The low flow velocities of this tunnel allow high conduction driver values to be achieved, which minimize the effects of aerodynamic error. A Pitot-static probe was positioned within the test section, and its pressure measurements were used to determine the flow velocity within the test section. Additionally, a type T total temperature probe was installed in the plenum of the wind tunnel and used as the reference total temperature value. An internal view of the closed test section, installed mounting strut, rotary table, and pitot probe positioning can be seen in Figure 4.11. The Virginia Tech Open Jet Wind Tunnel and closed test section have been utilized in prior literature and the flow uniformity was characterized by Cadel et al [41,49].

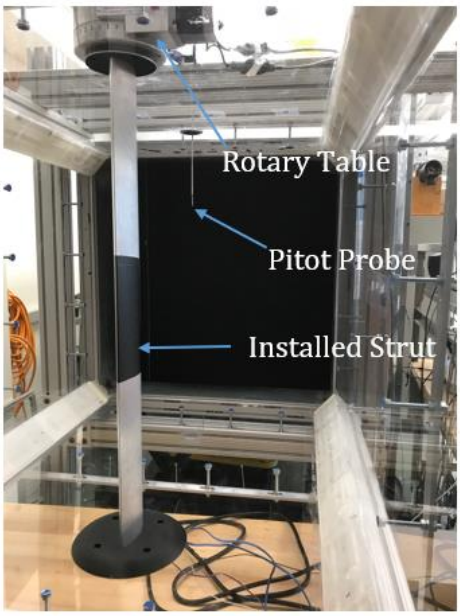

Figure 4.11: Internal view of Virginia Tech Open Jet Wind Tunnel closed test section setup

4.5 Conduction Error Experiment – Sensor Assembly and Procedure

In Section 4.3 above, three different methods for inducing a conduction error were discussed. The third method utilizing a heated base with an ambient temperature freestream flow was selected as the ideal method due to its implementation ease and ability to minimize radiation effects. Therefore, a strut and sensor assembly was designed to perform a heated base, conduction error experiment in the Virginia Tech Open Wind Tunnel facility. The following section outlines the instrumentation, experiment procedure, total temperature sensor selection, and sensor assembly method used in the heated, off-angle, conduction error experiments.

An extruded aluminum symmetric airfoil was selected as the mounting strut for the conduction error experiments. This strut featured a 3.12 in. chord, and a thickness to chord ratio of 0.38. The strut was machined so that the center span section of the airfoil featured a removable trailing edge.

This was done so that the thermocouples and base heater could be properly assembled and secured inside the center of the strut. The removeable trailing edge was designed so that it could reattach to the leading-edge using screws. The profile and removable trailing edge design of the utilized symmetric strut can be seen in Figure 4.12.

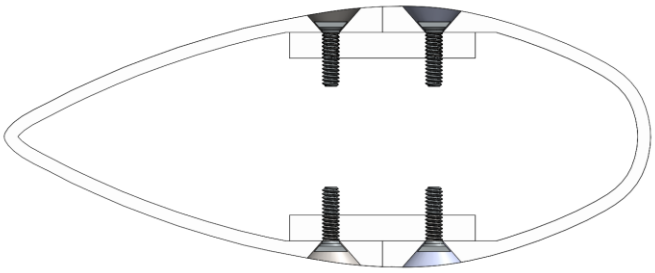

Figure 4.12: Symmetric strut profile for conduction error experiments

A Nexthermal coil heater was used to provide the conduction drivers necessary for the experiment. The coil heater was 110 Watts, sheathed in stainless steel, and had a ¼ in. inner diameter. The coil heater geometry and additional specifications can be seen in Figure 4.13.

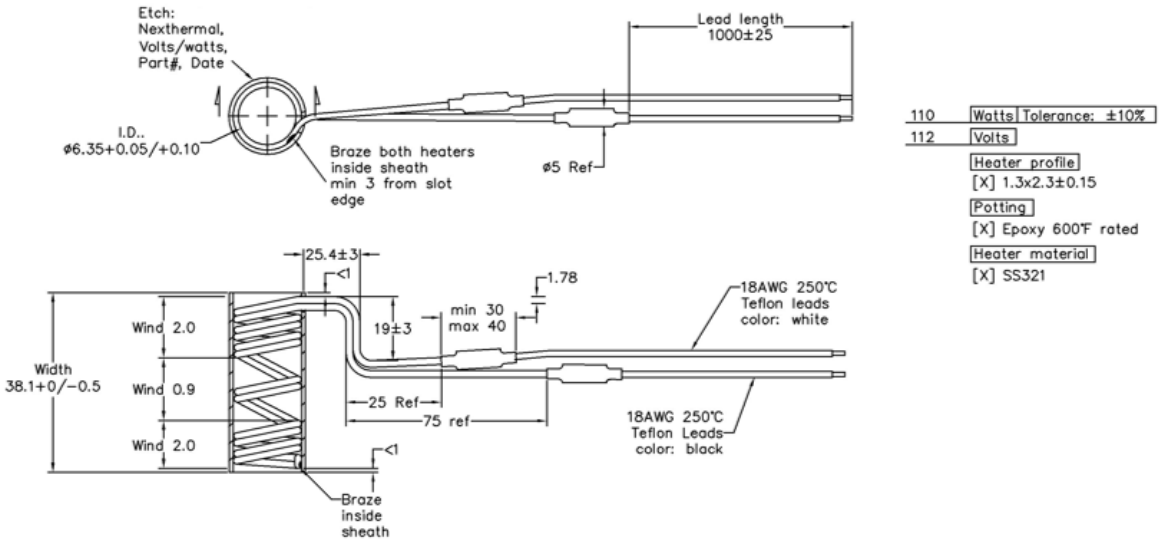

Figure 4.13: Nexthermal coil heater geometry and specifications

A ¼ in. thick-walled stainless-steel tube was inserted into the coil heater. A cut was made halfway along the length of the thick-walled tube and the tube was centered and attached to the strut's removable trailing edge insert. This tube supported the coil heater, prevented it from touching the strut walls, and positioned the heater near the center chord location of the strut. A small hole was drilled in the leading edge of the airfoil near center span for the tested thermocouple. For each test, the primary thermocouple was then fed through the thick-walled stainless-steel tube. The tube helped to secure the primary probe as well as enhance the heat transfer between the heater and the probe. A piece of high temperature heat shrink was attached to the primary thermocouple along the length that the base temperature probe was expected to be near. This insulated the base

temperature probe from the primary thermocouple so that a bare wire could be used for base temperature measurements. A small 0.005 in. or 0.010 in. diameter Type T, butt-welded, bare wire thermocouple was then wrapped around the primary thermocouple at the desired base location. The base thermocouple leads were insulated with additional miniature heat shrink and fed through the strut away from the heater. This ensured that only the primary probe was in contact with the heater, and the base temperature probe could read only the primary thermocouple temperature at the base location. An example image of a base temperature probe assembled with the primary thermocouple using the described method can be seen in Figure 4.14.

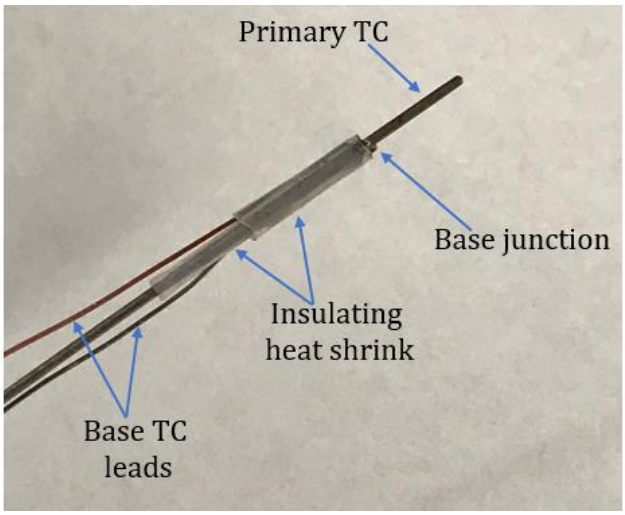

Figure 4.14: Base temperature probe assembly

The voltages from each thermocouple used in this experiment were measured using a National Instrument NI-9213 c-series temperature module mounted within a NI-9181 cDAQ chassis. This instrumentation is capable of a maximum sample rate of 75 samples per second and can acquire 16 simultaneous, high speed voltage measurements with channels separated by a 250 Vrms CAT II, Ch to Earth isolation. During the conduction error experiments, data was acquired at 50 Hz for the symmetric strut configurations and at 3 Hz for the later cambered strut configuration. The voltage measurements from the data acquisition system were recorded and converted to temperature measurements using a developed LabView code. The coil heater was controlled with a Digi-Sense model 89000-10 AC voltage source/temperature controller. This voltage source was capable of providing up to 110 volts and 15 amps of current to the heater and was controlled using a reference thermocouple that was secured to the outside of the coil heater. This reference thermocouple was a 0.032 in. diameter type K thermocouple and indicated that the heater controller was capable of heating the coil heater above 900 F. An image of the utilized strut, coil heater, control thermocouple, and a test thermocouple assembly can be seen in Figure 4.15. After the probe was assembled, the sensor was positioned through the strut leading edge hole at the desired test L/d, and the trailing edge assembly was reattached to the strut. Thin black tape was used to seal the joint where the trailing edge reattaches to the primary strut and cover up exposed screw holes. Finally, the leading-edge hole used to expose the primary thermocouple to the flow was sealed with epoxy. A fully assembled unshielded total temperature sensor can be seen in Figure 4.16.

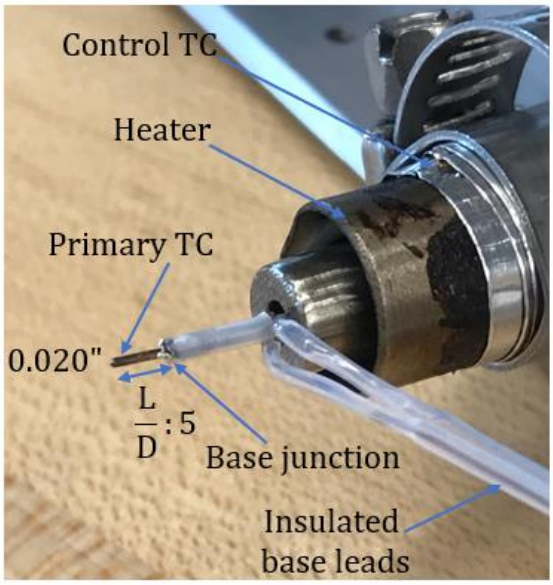

Figure 4.15: Strut-internal heated total temperature sensor assembly

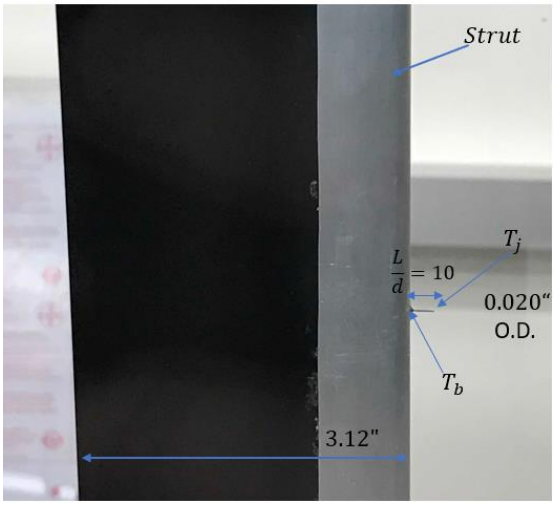

Figure 4.16: Fully assembled unshielded total temperature sensor

Five, type E, sheathed thermocouples with different probe geometries were tested during this experimental study. A length study using three probes with a diameter of 0.020 in. and designed L/d of 5, 7.5, and 10 was setup to be tested. After assembly of each configuration, it was found that the actual probe geometries had L/d of 5, 8, and 10 or L/t of 0.08, 0.128, and 0.16. Additionally, a diameter study was designed to test three probes with a constant L/t parameter but varying diameters. Two probes, one with a 0.010 in. diameter and one a 0.032 in. diameter, were designed to have the same L/t as the nominal 0.020 in. L/t = 0.08 probe. However, after assembly of each configuration the 0.010 in. diameter probe was measured to have a L/d of 12 (L/t = 0.096) and the 0.032 in. diameter probe was measured to have a L/d of 3 (L/t = 0.096). A diagram of the probe geometry test space can be seen in Figure 4.17. The first three probes with a constant diameter were designed to analyze the effects of L/t. This parameter determines the mount

interference effects seen by the probe for a given strut geometry. Similarly, the 0.032 in. and 0.010 in. probes were designed to have the same L/t as the nominal probe with a 0.020 in. diameter and L/d of 5. Therefore, these probes could be used to study the effects of diameter on conduction error during off-angle conditions.

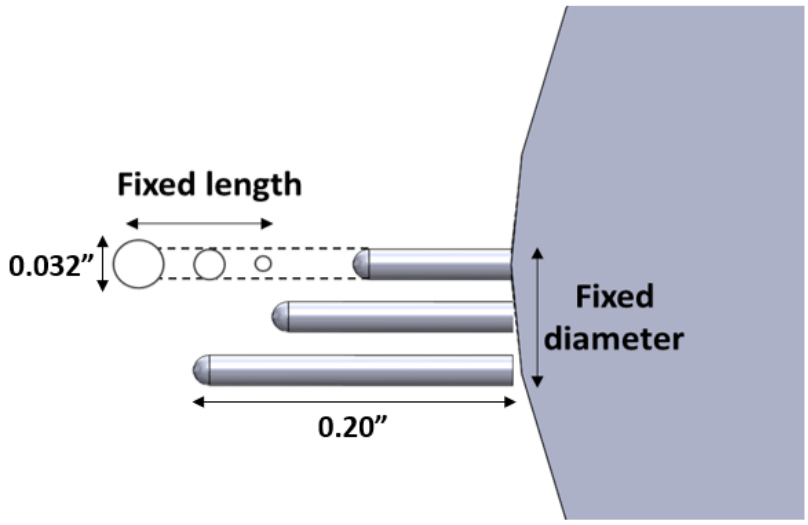

Figure 4.17: Conduction error experiment, tested probe geometries

The procedure for performing the conduction error experiments will be outlined below. First, the strut is returned to the zero-pitch angle position. Next, the wind tunnel is brought up to its testing flow velocity of 12.6 m/s. Then, the heater is activated and the controlling reference temperature is brought to 700 F. Once all temperatures have reached a steady state, two minutes of data is recorded. Next the pitch angle is increased to 1 degree. The probes are then given one minute to reach a steady state and then two minutes of data is collected. This process is repeated for 1-degree increments up to a 5-degrees angle of attack. Then, 5-degree increments are used until 20 degrees. Finally, data is recorded for a 30-degree pitch angle. Once data for 0-30 degrees was acquired, the process was repeated for negative angles. The entire process was also repeated for two additional conduction driver values. Average conduction driver values around 0.07, 0.1 and 0.13 were all tested. Additionally, data was collected for a continuous angle sweep from 0 to 30 degrees for each probe geometry. This continuous angle sweep was performed by setting the stepping motor to rotate continuously at a rate of 1 degree per 16 seconds.

The velocity of 12.6 m/s was selected for testing because it produced a continuous flow state over the airfoil during pitch angle sweeps. Higher tunnel velocities were identified to have multiple flow solutions over the airfoil for a given pitch angle of attack. This was identified using a tuft flow visualization on the airfoil. During this tuft flow visualization, a single flow state would be visualized, then the flow would be disturbed and then let return to its initial state, instead the flow would stabilize at a new second steady state. This flow phenomena was not witnessed at the selected 12.6 m/s flow velocity and was most likely due to the testing conditions being near flow transition Reynolds numbers. The chord-based Reynolds number of the performed conduction experiments was 64,000. This Reynolds number would increase to around 128,000 with a

freestream tunnel flow velocity of 25 m/s. Nevertheless, the selected test velocity provided optimal conduction driver values and minimal aerodynamic error for the performed set of conduction error tests.

After performing the experiments, a Matlab script was used to post-process the raw temperature measurements. A post-processing procedure similar to that described in Section 4.2 was performed. The temperature results at each flow angle were averaged along the two minutes of recorded data. Then, the measured temperatures were used to calculate the sensors recovery and conduction sensitivity. This post-processing provides one performance value for each flow angle and minimizes signal noise and small oscillations in the measurements. Additionally, the conduction sensitivity results from tests with different conduction drivers were evaluated. The collapse of conduction sensitivity for different driver values was verified for each probe geometry and results showing this will be presented in Section 5.4.

4.6 Additional Conduction Error Investigations

Three other unique conduction error experimental investigations were performed. The first was an experimental study to analyze the impact of forced unsteadiness on sensor performance. In order to evaluate this, a cylinder was positioned upstream of the symmetric strut and total temperature sensor assembly previously described in Section 4.5. This upstream cylinder generated an unsteady Von Karman vortex street which impacted the downstream total temperature sensor. This experiment was performed with one probe geometry which consisted on the nominal type E, 0.020 in. diameter probe with a L/d of 5. A diagram of the forced unsteadiness experiment can be seen in Figure 4.18.

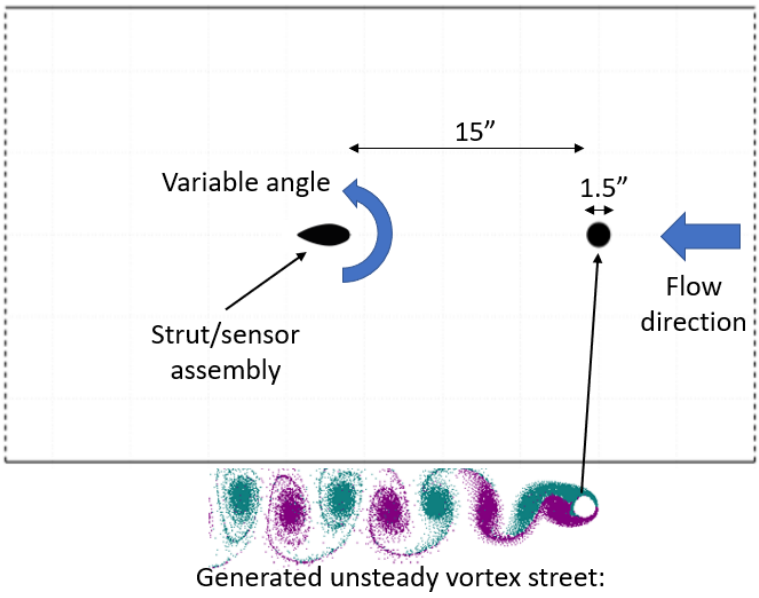

Figure 4.18: Diagram of forced unsteadiness experiment

The cylinder used in the forced unsteadiness experiment had a 1.5 in. diameter and was positioned ten diameters upstream of the strut's leading edge. Equation 4.2 can be used to estimate the shedding frequency of the circular cylinder if the Strouhal number (St) is known. A Strouhal number of 0.2 was estimated based on recommendations from Clark et al for diameter-based Reynolds numbers between 80 and 300,000 [42].

$$f = \frac{d*St}{U_\infty} \tag{4.2}$$

Using a Strouhal number if 0.2, Equation 4.2 predicts a shedding frequency of around 66 hertz for the upstream circular cylinder. This experiment was performed using the closed test section, and the same experimental procedure outlined in Section 4.5 was followed.

The second experimental investigation that was performed was to verify whether the tunnel walls had any influence on the total temperature sensors performance. A mount was designed to attached the previously discussed rotary table and mounting strut directly to the contraction nozzle exit in the wind tunnel. The designed mount and open jet configuration can be seen in Figure 4.20. The symmetric strut experiment using the nominal 0.020 in. diameter probe with an L/d of 5 was repeated using the open test section configuration. In this configuration, the closed test section was removed and the strut leading edge was positioned very close to the tunnel exit so that flow dispersion and any impacts of the tunnel walls would eliminated. The same experimental testing procedure was followed for this experiment that was outlined previously for off-angle conduction tests.

Finally, an experiment was performed to analyze how the impact of mount interference and freestream flow angle changes when the mounting strut features camber. This test was also designed to assess the use of the virtual probe method with current conduction error model for a more complex strut geometry. A cambered trailing edge was designed to attach directly to the symmetric strut that was utilized during the previously discussed conduction error experiments. This cambered trailing edge design results in a total strut chord length of 3.90 inches, a maximum thickness to chord ratio of 0.31, and a maximum camber of 0.21 inches. The designed cambered trailing edge profile can be seen in Figure 4.19.

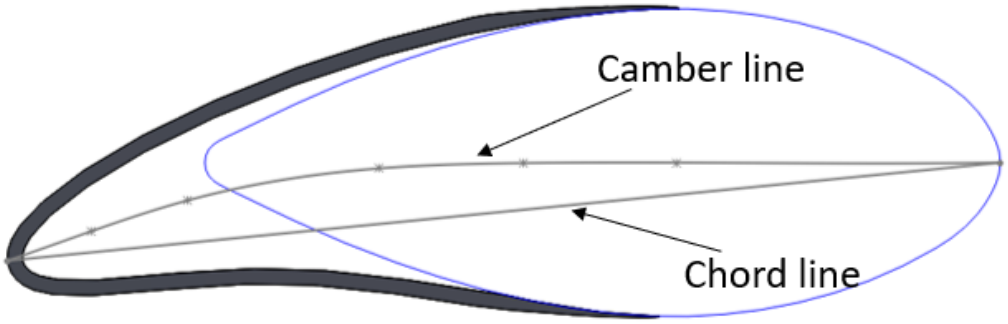

Figure 4.19: Cambered strut profile

The cambered trailing edge was 3D-printed and attached to the symmetric strut. One 14 in. section and two 5 in. sections were printed to create a cambered trailing edge with a span of 24 inches

which spanned the majority of the nozzle exit height. The trailing edge attached to the strut at the maximum thickness, and was designed to create a smooth interaction between the leading edge of the aluminum strut and the attached trailing edge. Thin, black tape was used to cover and seal the interaction between the cambered trailing edge and the primary aluminum strut. The 3D-printed trailing edge attached to the symmetric strut can be seen in Figure 4.20. The open jet configuration was used for the cambered conduction error experiment, and the nominal sheathed, type E probe with a 0.020 in. dimeter and L/d of 5 was tested. The experimental procedure that was previously outlined for off-angle conduction error experiments was utilized to test the cambered profile with the 0.020 in. total temperature sensor.

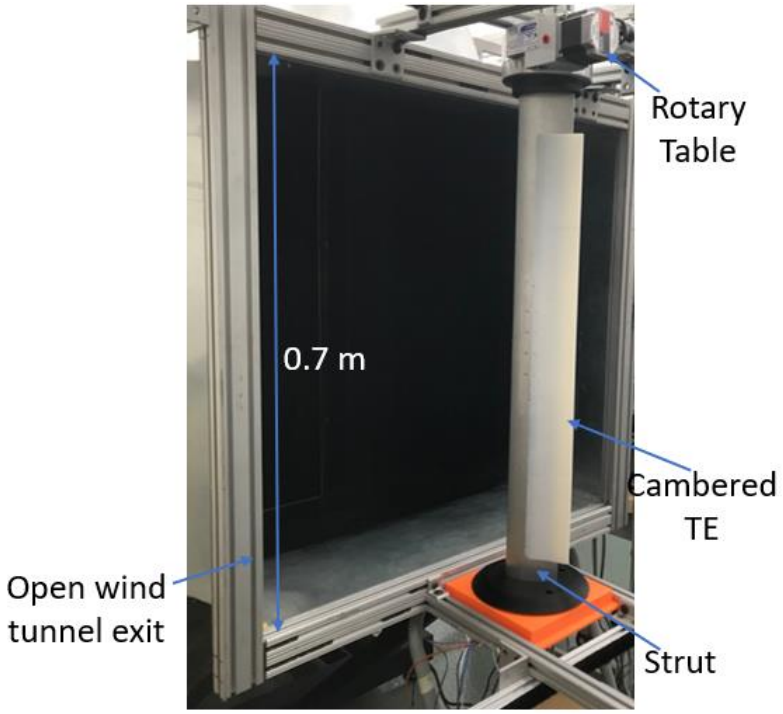

Figure 4.20: Open test section mounting configuration

5 Results

Experimental results for both the aerodynamic error and conduction error experiments will be presented in this section. Performance trends from the experiments will be analyzed, and flow visualizations from 3D CFD computations will be used to help identify flow physics driving identified performance trends. The accuracy of different low-order models and the virtual probe method will be shown. An uncertainty quantification will be presented for both the aerodynamic error and conduction error experiments.

5.1 Aerodynamic Error Experiment Results

In this section the results from the experiment described in Section 4.2 will be presented. This velocity error Mach sweep experiment was performed so that the effects of mount interference could be analyzed, and so that L/t values where significant mount interference effects are present could be identified. Also, the experimental results will help assess the developed virtual probe method for analytically predicting aerodynamic error in the presence of mount interference. The experiment results for the sheathed probes (L/t = 0.067 and L/t = 0.15) and bare wire probe (L/t = 0.059) can be seen in Figure 5.1

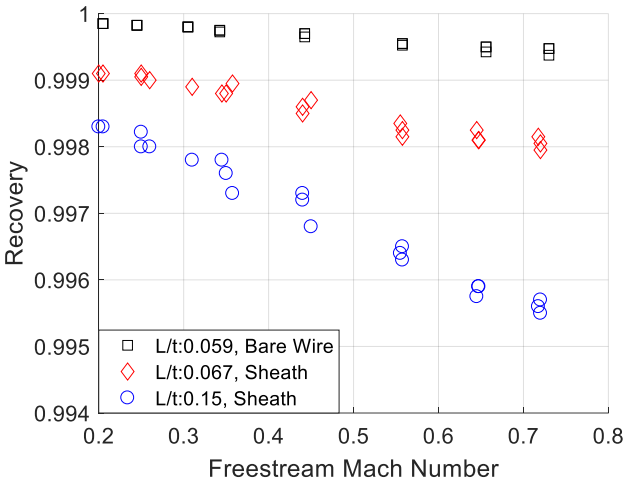

Figure 5.1: Comparison of Mach sweep experiment results

The experimental results show that unshielded, total temperature sensors with a small L/t can utilize mount interference to reduce aerodynamic error. This is possible due to the mount continuously reducing the flow kinetic energy around the probe as L/t is decreased which results in lower aerodynamic error. This occurs because the total temperature sensor is positioned with the mount stagnation point at the base of the probe. Another benefit that can be provided by mount interference effects is a freestream Mach insensitivity for probes positioned near the flow stagnation point on the strut. This can be seen by the recovery slopes decreasing as L/t decreases in Figure 5.1. The high recovery and Mach insensitivity benefits from mount interference will only hold true for this probe positioning for a zero angle of attack freestream flow. However, the probe

could be positioned at a different angle or orientation to provide similar benefits in a freestream flow with a constant angle of attack.

5.2 Aerodynamic Error Low-Order Model Predictions

The developed low-order method to account for mount interference was utilized to predict the performance of each experimentally tested total temperature sensor. The mount interference effects on the local flow-field were modeled by a Rankine half-body flow solution. The L/t ratios of each probe were then used to identify the location to extract virtual probe tip velocities within the flow-field solution. A recovery prediction was then calculated for each probe geometry using Equation 2.1 combined with Equation 1.8. These predictions were calculated for every Mach number tested during the Mach sweep experiment, and the Moffat recommended aerodynamic recovery factor $\alpha = 0.86$ for parallel flow was used. Additionally, recovery predictions using freestream flow conditions and Equation 1.8 were calculated for each probe geometry and every Mach number. Finally, recovery predictions were calculated using the mount interference low-order model with a Karmen-Tsien compressibility correction applied to the predicted flow field solution. A comparison between the experiment results and different prediction methods for the sheathed, L/t = 0.067 probe can be seen in Figure 5.2. Additionally, comparisons between the experiment results and different prediction methods for the sheathed L/t = 0.15 probe and the bare wire L/t = 0.059 probe can be seen in Figure 5.3 and Figure 5.4 respectively. In the legend of Figures 5.2-5.4, "Exp" refers to experiment results. "LOM" refers to the low-order model predictions using freestream flow conditions and the model seen in Equation 1.8. "LOM RH" refers to predictions made with the mount interference low-order model using a Rankine half-body to model the flow-field. Finally, "LOM RH KT" refers to predictions made with the mount interference low-order model using a Rankine half-body flow-field with a Karmen-Tsien compressibility correction applied.

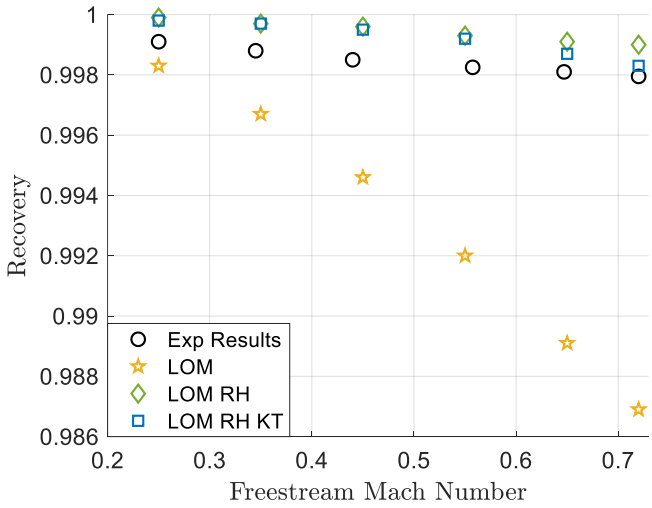

Figure 5.2: Comparison of experiment results and low order aero recovery predictions for sheathed L/t = 0.067 probe

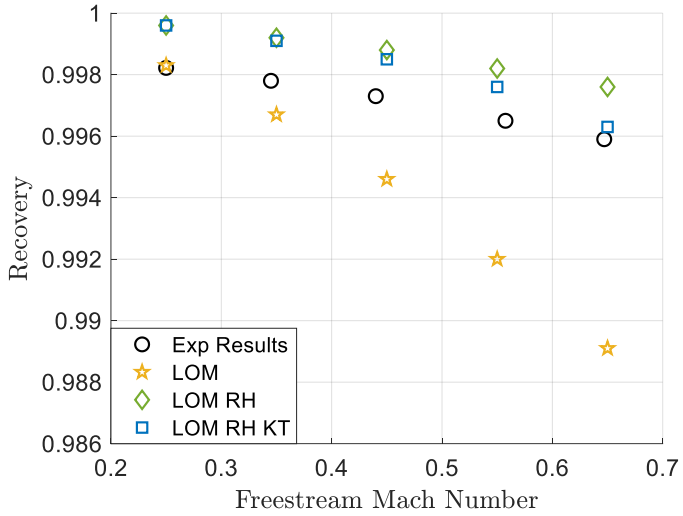

Figure 5.3: Comparison of experiment results and low order aero recovery predictions for sheathed L/t = 0.15 probe

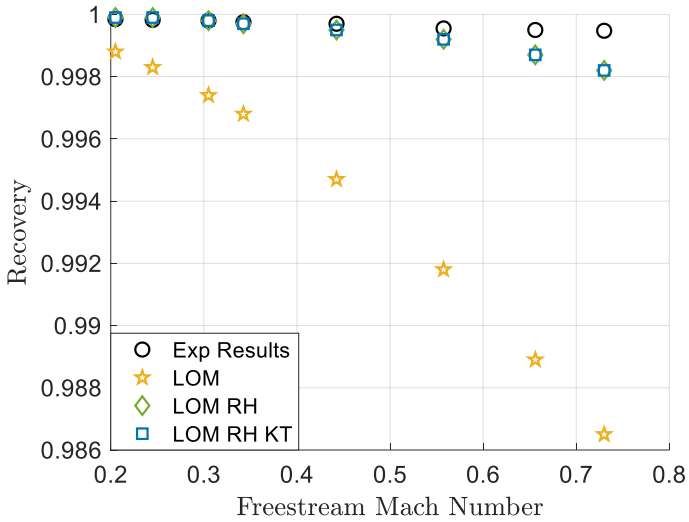

Figure 5.4: Comparison of experiment results and low order aero recovery predictions for sheathed L/t = 0.059 bare wire probe

The comparisons in Figures 5.2-5.4 show that aerodynamic error will be significantly over-predicted for strut-mounted, low L/t probes if mount interference is not considered. The prediction difference relative to the experiment results is rather small at low Mach numbers, but becomes extremely large at high Mach numbers. The above comparisons also show that the mount interference low-order model, or virtual probe method, is capable of more accurately predicting the experiment results by accounting for how the mount changes the local flow-field. However, there is still a small delta between the model predictions and experimental results. This small delta is relatively constant with Mach number, but can be significantly decreased at high Mach numbers if the Karmen-Tsien compressibility correction is used. A summary of the percent difference between the recovery of each low order prediction and the experiment results is provided in Table

5.1. The percent difference summary provides a quantitative comparison of each method and shows that the developed low order method utilizing a Rankine half body and Karmen-Tsien compressibility correction provides the most accurate predictions.

Table 5.21: Summary of the percent difference between the recovery of each low order method and the experiment results

Mach Number	0.25	0.35	0.45	0.55	0.65
L/t = 0.059 Probe:					
LOM % Difference	-0.15%	-0.24%	-0.30%	-0.50%	-0.78%
LOM RH % Difference	0.01%	0.00%	-0.01%	-0.02%	-0.03%
LOM RH KT % Difference	0.01%	0.00%	-0.01%	-0.02%	-0.04%
L/t = 0.067 Probe:					
LOM % Difference	-0.08%	-0.21%	-0.39%	-0.63%	-0.90%
LOM RH % Difference	0.08%	0.09%	0.11%	0.11%	0.10%
LOM RH KT % Difference	0.07%	0.09%	0.09%	0.07%	0.01%
L/t = 0.15 Probe:					
LOM % Difference	0.01%	-0.11%	-0.27%	-0.45%	-0.68%
LOM RH % Difference	0.14%	0.14%	0.15%	0.17%	0.17%
LOM RH KT % Difference	0.14%	0.13%	0.12%	0.11%	0.04%

There are a few potential causes for the difference between the experiment results and the virtual probe method predictions. The first is that the predicted flow-field solution is not completely accurate. The potential flow solution is expected to provide a good estimate of the flow-field at low Mach numbers, but assumes incompressible flow and should therefore be inaccurate at high Mach numbers. However, the delta between the predictions and experiment is just as large at low Mach numbers as it is at high Mach numbers. The true flow around the airfoil could be separating near the trailing edge which would not be captured in the potential flow solution and would impact the upstream flow. This type of error could be accounted for by using a 2D, CFD solution of the flow-field instead of the Rankine-half body. However, since the delta between the virtual probe predictions and experiment results is relatively constant with Mach number, it is more likely caused by the presence of a small conduction error within the experiment results. Furthermore, the beaded, bare-wire virtual probe predictions agree extremely well with the experiment results, especially at low Mach numbers. This probe would be expected to have a considerably lower conduction error than the two sheathed probes because of the extremely small 0.003 in. wire

diameters. The performed aerodynamic error experiments were designed to minimize conduction effects; however, some conduction error will always be present for strut-mounted temperature probes due to aerodynamic cooling of the strut.

During the aerodynamic error experiments, a temperature sensor was positioned near the primary probe base location. The measurements from this base probe were used to estimate conduction drivers experienced by the sheathed sensors throughout the Mach sweep. Since the base sensor was not measuring along the conduction path of the primary probe, the measured condition drivers are expected to be higher than the true driver. However, the base temperature measurements indicate the sheathed sensors experienced conduction drivers between 0.0012-0.0049 throughout the Mach sweep. Even though these driver values are very small, they result in conduction error with the same order of magnitude as the predicted aerodynamic error. These two errors are on the same order of magnitude because the local flow velocity is greatly reduced by the mount. The conduction error for both sheathed, total temperature probes was estimated using Equation 2.16, half the measured conduction driver, and freestream flow conditions. The predicted conduction error was then combined with the predicted aerodynamic error to calculate the total recovery of each sheathed probe. The total recovery predictions for the sheathed, L/t = 0.067 probe can be seen in Figure 5.5. Meanwhile, the total recovery predictions for the sheathed, L/t = 0.15 probe can be seen in Figure 5.6.

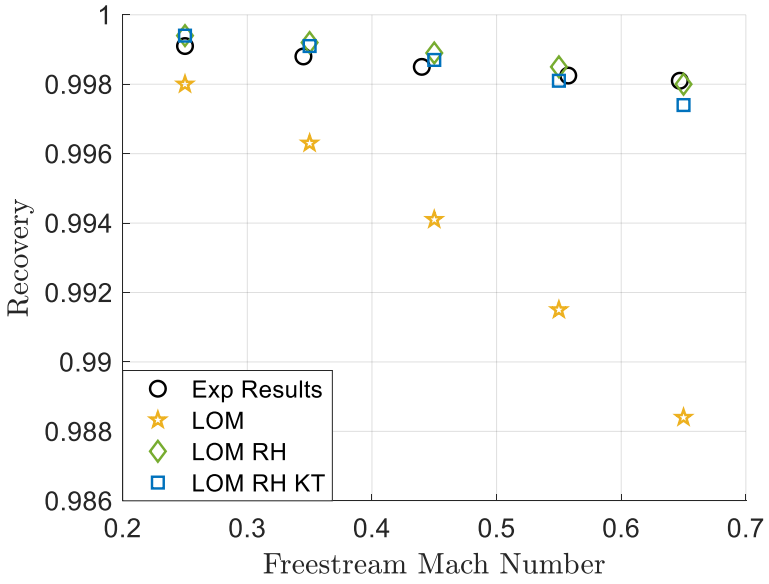

Figure 5.5: Comparison of experiment results and total recovery predictions using combined conduction and aerodynamic error, sheathed L/t = 0.067 probe

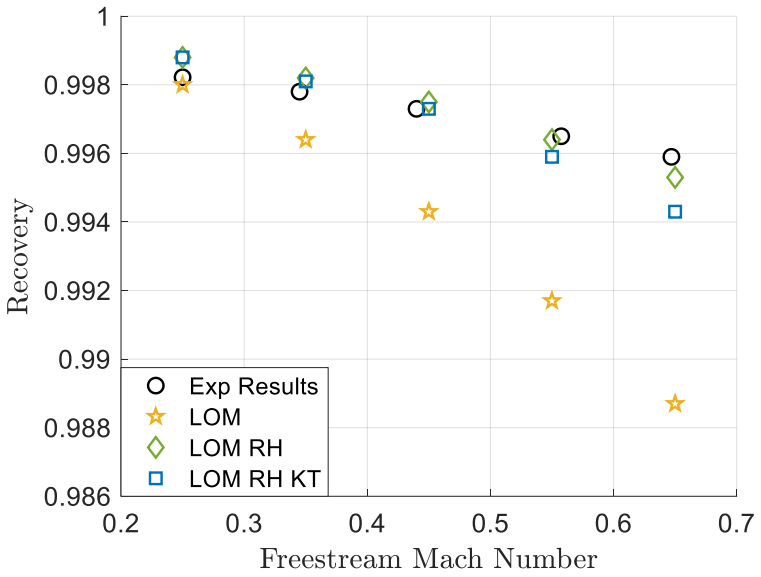

Figure 5.6: Comparison of experiment results and total recovery predictions using combined conduction and aerodynamic error, sheathed L/t = 0.15 probe

The total recovery predictions for both probes agree well at low Mach numbers. The L/t = 0.067 probe also has very good agreement at high Mach numbers, while predictions for the L/t = 0.15 probe begin to over predict the combined probe error at high Mach numbers. This is most likely due to higher velocity, compressible flow over the L/t = 0.15 probe that is not well predicted by the Karmen-Tsien correction. Meanwhile, the flow over the shorter L/t = 0.067 is always near the incompressible flow regime since it is so close to the strut leading edge stagnation point. Overall, the virtual probe method greatly improves the original predictions and is capable of accurately predicting aerodynamic error of a total temperature probe in the presence of mount interference. This virtual probe method utilizing potential flow can be performed thousands of times faster than full-scale CFD simulations. Therefore, this method can be utilized for the rapid design and optimization of unshielded total temperature probes. While using a Rankine half-body flow solution, the method is restricted to attached, incompressible flows over a symmetric strut. However, application of the virtual probe method can be greatly expanded by using a panel method or 2D, CFD flow solution. These more advanced tools will increase prediction time, but would allow the virtual probe method to predict a probe aerodynamic error when separated and compressible flows are present along with predicting the mount interference effects of complex cambered airfoil geometries.

5.3 Aerodynamic Error Results – Uncertainty Quantification

A formal uncertainty quantification was performed to determine the overall uncertainty of both the aerodynamic error experiment results and the low order model predictions. The total system uncertainty is a result of the individual uncertainty in each component that contribute to a system. These individual uncertainties are generally known or estimated, but there are numerous

formulations that can be utilized to calculate a systems total uncertainty. The method presented by Kline and McClintock (1953) [48] will be discussed below and utilized for uncertainty quantification in this work. First, consider a result or system F, seen in Equation 5.1, that is a function of n independent variables. The change in F for small changes in x_n can be estimated using a Taylor series expansion as seen in Equation 5.2.

$$F = f(x_1, x_2, \dots x_n) \tag{5.1}$$

$$\Delta F = \frac{\partial f}{\partial x_1}\Delta x_1 + \frac{\partial f}{\partial x_2}\Delta x_2 \dots + \frac{\partial f}{\partial x_n}\Delta x_n \tag{5.2}$$

In Equation 5.2, the change in each independent variable Δx is representative of the individual uncertainty of that variable. Meanwhile, the partial derivatives indicate the sensitivity of F to changes in each variable. The root-sum squared formula can then be applied to Equation 5.2 to determine the total uncertainty of y. This uncertainty formulation, utilized by Kline & McClintock (1953) [48], is often referred to as the propagation of errors and can be seen in Equation 5.3.

$$\delta y = \sqrt{(\frac{\partial f}{\partial x_1} * \delta x_1)^2 + (\frac{\partial f}{\partial x_2} * \delta x_2)^2 \dots + (\frac{\partial f}{\partial x_n} * \delta x_n)^2} \tag{5.3}$$

The uncertainty quantification method described above can be applied to the overall recovery results for the aerodynamic error experiment. In this experiment, the overall recovery is known as a function of the plenum total temperature T_t and tested junction temperature T_j, as seen in Equation 5.4. Given the overall recovery's known dependent variables, the total uncertainty formulation seen in Equation 5.5 can be formed. The partial derivates in Equation 5.5 were each evaluated and can be seen in Equation 5.6.

$$R_{Exp} = f(T_j, T_t) \tag{5.4}$$

$$\delta R = \sqrt{(\frac{\partial R}{\partial T_j} * \delta T_j)^2 + (\frac{\partial R}{\partial T_t} * \delta T_t)^2} \tag{5.5}$$

$$\frac{\partial R}{\partial T_j} = \frac{1}{T_t} \quad \text{and} \quad \frac{\partial R}{\partial T_t} = -\frac{T_j}{T_t^2} \tag{5.6}$$

The individual uncertainties of the two temperature measurements were determined based on uncertainty values provided by the sensor manufacturer. A type K thermocouple with special limits of error was used for the plenum total temperature measurement. The uncertainty of this thermocouple is reported to be the higher of 1.1 C or 0.4%. Since all calculations were performed using absolute temperature values in Kelvin, 0.4% of the measured temperature was utilized and provided a higher uncertainty estimate. Similarly, a type E thermocouple with special limits of error was used for all tested T_j measurements. The uncertainty of these thermocouples was reported to be the higher of 1 C or 0.4%. Therefore, 0.4% of the measured junction temperature was used for the individual uncertainty of T_j. The total uncertainty for the experimental recovery was calculated for both tested sheathed probes at every tested Mach number, and the results can be seen in Figure 5.7.

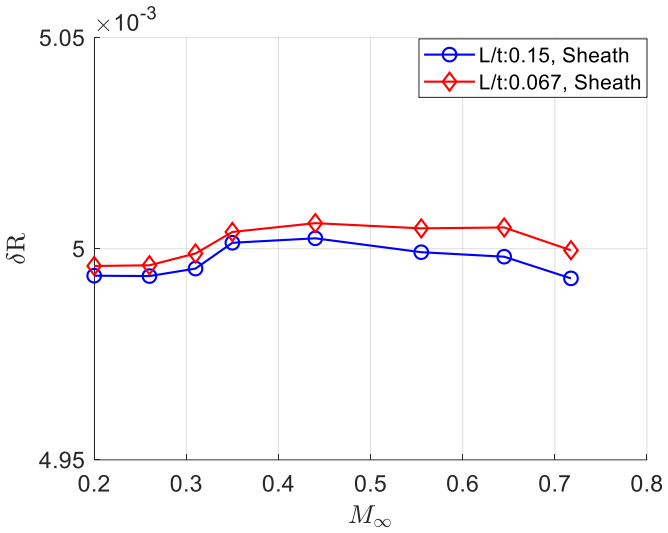

Figure 5.7: Uncertainty of aerodynamic error experiment results

The total uncertainty changed slightly with Mach number due to the flow total temperature varying throughout the Mach sweep tests. However, overall the total recovery uncertainty is around 0.005 for both tested sheathed probes. This uncertainty value is larger than the accuracy needed to compare mount interference effects on aerodynamic error for this experiment. The large uncertainty is a result of the large individual uncertainties of the tested thermocouples; therefore, a correction was applied to account for the individual uncertainty of each thermocouple. This correction procedure was previously discussed in Section 4.2 and was used to reduce the individual uncertainties of the tested temperature sensors.

Next, a formal uncertainty quantification was performed for the developed low-order model predictions. The same total uncertainty calculation method was used, but the predicted recovery is known to be a function of the aerodynamic recovery factor α, the freestream Mach number, and the local Mach number as seen in Equation 5.7. An equation for the predicted recovery factor total uncertainty was then developed and can be seen in Equation 5.8. The partial derivatives in Equation 5.8 were evaluated and can be seen in Equation 5.9.

$$R_{LOM} = f(\alpha, M_\infty, M_{local}) \tag{5.7}$$

$$\delta R = \sqrt{(\frac{\partial R}{\partial \alpha} * \delta\alpha)^2 + (\frac{\partial R}{\partial M_\infty} * \delta M_\infty)^2 + (\frac{\partial R}{\partial M_{local}} * \delta M_{local})^2} \tag{5.8}$$

$$\frac{\partial R}{\partial \alpha} = \frac{(-1+\gamma)M_{\text{local}}^2}{2(1+\frac{1}{2}(-1+\gamma)M_\infty^2)}, \quad \frac{\partial R}{\partial M_\infty} = \frac{(1-\alpha)(-1+\gamma)^2 M_{\text{local}}^2 M_\infty}{2(1+\frac{1}{2}(-1+\gamma)M_\infty^2)^2}, \quad \frac{\partial R}{\partial M_{local}} = -\frac{(1-\alpha)(-1+\gamma)M_{\text{local}}}{1+\frac{1}{2}(-1+\gamma)M_\infty^2} \tag{5.9}$$

The individual uncertainty of the freestream Mach number was estimated to be around 2% based on freestream Mach number variation witnessed in repeated experimental tests. Meanwhile, the local Mach number uncertainty was expected to be slightly larger since a Rankine-half body was used to model the flow-field. Therefore, a 5% uncertainty was used for the local Mach number. Finally, a 10.5% uncertainty in α was utilized. This value was determined based on Moffat reported $\alpha = 0.86 \pm 0.09$ value for a parallel flow. These individual uncertainty values were then used with

Equation 5.8 to calculate the total uncertainty of the predicted recovery values. The total uncertainty was quantified for all three analyzed probes at each Mach number of interest. The total uncertainty of the predicted overall recovery values can be seen in Figure 5.8.

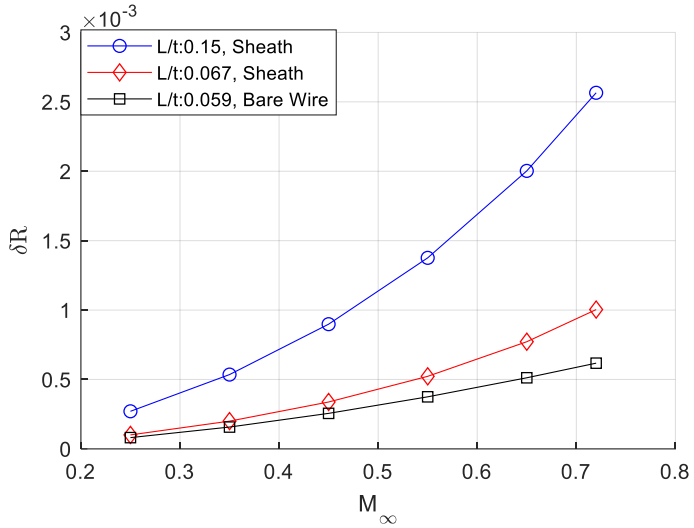

Figure 5.8: Uncertainty of LOM aerodynamic error predictions

The uncertainty results in Figure 5.8 show that the total recovery uncertainty rapidly increases with freestream Mach number. This is because the individual uncertainty in both freestream and local Mach number increases as the Mach number increases. Similarly, it can be seen that the total uncertainty is smallest for the bare wire probe with L/t = 0.09, but continuously increases as the probe L/t is increased. This trend is due to the presence of mount interference which results in the local Mach number increasing as L/t increases. Overall, the prediction uncertainty is quite low at low Mach numbers but grows to a significant value at high Mach numbers. This is consistent with the good agreement between experiment results and low order predictions at low Mach numbers but worsening agreement at high Mach numbers.

5.4 Conduction Error Experimental and CFD/CHT Results

In this section, the results from the experiments described in Section 4.5 will be presented. These conduction error experiments were performed so that the effects of mount interference and freestream flow angle could be studied. The results will be used to identify performance trends with geometry in the presence of these two effects, and results from 3D CFD simulations will be used to identify the flow physics driving the witnessed performance trends. Also, the experimental results will help assess the developed virtual probe method for predicting mount interference and flow angle effects. First, the experimental results for the symmetric strut tested in the Virginia Tech Open Jet Wind Tunnel using the closed test section will be discussed. The experimental results for the nominal probe with a 0.020 in. diameter and a L/d of 5 (L/t = 0.08) can be seen in Figure 5.9:

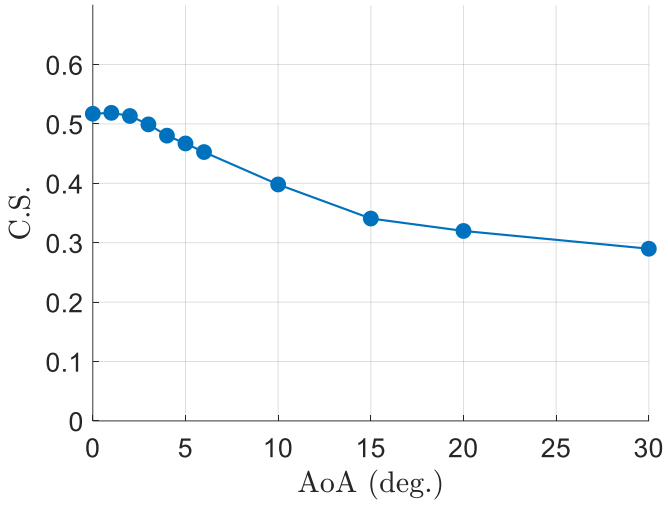

Figure 5.9: Experimental results for 0.020", L/d = 5 (L/t = 0.08) probe in symmetric strut

Figure 5.9 shows the conduction sensitivity of the total temperature probe versus the freestream flow angle. The conduction sensitivity parameter (C.S.) was previously defined in Section 2 as a reformulation of conduction error that is independent of conduction driver. The conduction driver independence of C.S. results for each probe geometry were verified by calculating C.S. from experimental results for the same probe but with different conduction driver values. Conduction sensitivity results for the nominal probe with measured conduction driver values of 0.08 and 0.16 can be seen in Figure 5.10.

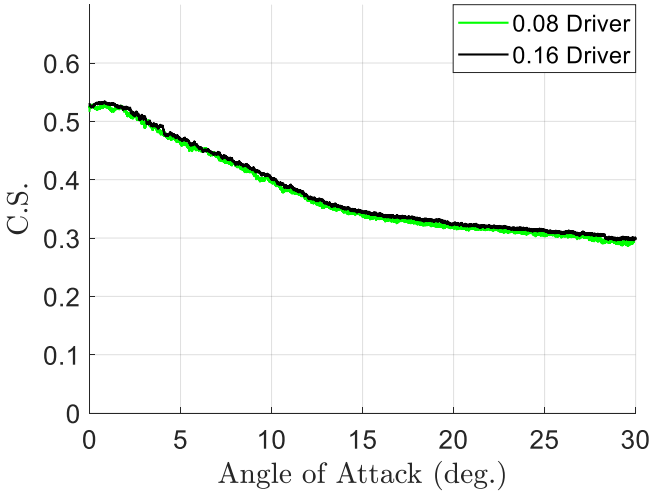

Figure 5.10: Experimental C.S. collapse for the nominal 0.020", L/d = 5 total temperature probe

As can be seen from Figure 5.10, the results for the nominal total temperature probe are almost exactly the same with a doubled conduction driver value. This confirmation that the C.S. results were independent of the conduction driver provides partial verification that the strut/total temperature probe configuration was assembled as designed. The results from Figure 5.9 and 5.10 show that the nominal unshielded total temperature probe is very sensitive to the freestream flow angle. There is a small region where the probe is insensitive to flow angle between 0-2°. This

region is caused by the probe remaining within or very close to the strut's leading-edge stagnation point. The sensitivity to angle can also be seen to decrease significantly at angles greater than 15°. Though the results indicate the probe is sensitive to angle, the C.S. continuously decreases with flow angle. That means the temperature probe recovery is continuous increasing with angle, and the measured temperature is getting closer to the total temperature of the fluid. 3D CFD simulations for the nominal probe geometry were performed at four different freestream angles of attack: 0°, 5°, 10°, and 20°. The film heat transfer coefficient, *h*, from these CFD simulation can be used to help identify why the conduction error continuously decreases with angle. Figure 5.11 shows a surface averaged *h* for the nominal probe geometry versus angle of attack.

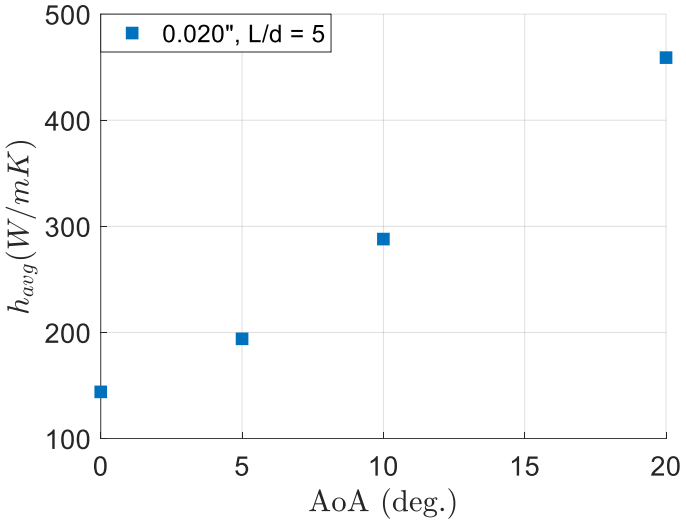

Figure 5.11: Sensor CFD/CHT prediction of averaged convection coefficient vs. freestream flow angle for 0.02 in., L/d = 5 probe

It can be seen from Figure 5.11 that the average convection heat transfer coefficient continuously increases with freestream angle of attack. Equation 2.17 clearly shows that increasing, *h*, would result in the decreasing, *h*, trend seen in Figure 5.9. The 3D, CFD results can further be used to help identify what flow characteristics are causing the increase in h with freestream flow angle. A plot of streamlines around the nominal temperature probe with contours of the probe's *h* at freestream flow angles of 0° and 10° can be seen in Figure 5.12.

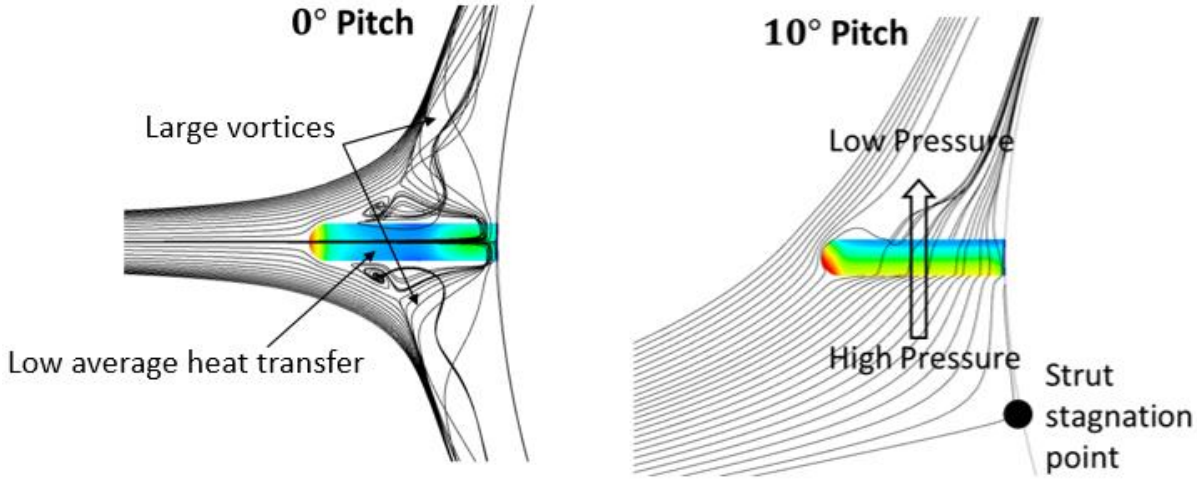

Figure 5.12: CFD/CHT results of streamlines around 0.020", L/d = 5 probe, 0° and 10° freestream flow angles

The streamlines in Figure 5.12 show that the strut stagnation region flow creates vortical structures along the side of the total temperature probe. These vortical structures have relatively low velocities and bring the flow away from the sensor. This results in a low, *h*, when the freestream flow is parallel to the probe. This interaction between the probe, mount, and the freestream flow is extremely complicated, but is only present at very low angles. Figure 5.12 shows that at slightly larger freestream flow angles the local flow across the probe closely resembles a crossflow. This is because the strut stagnation point shifts off the probe and creates a pressure gradient across the sensor resulting in high crossflow. The crossflow results in high velocities across the sensor which create a high average film coefficient, *h*, explaining the trend in Figure 5.11. In fact, at moderate angles the entire configuration of study closely resembles a cylinder in crossflow. This crossflow behavior is also seen in the 5° and 20° CFD results.

Now, that the performance trends and driving flow features of the nominal 0.020 in., L/d = 5 probe have been studied, the influence of probe geometry on mount interference and flow angle effects can be investigated. The results of a probe length study will be discussed first. For this study three 0.020 in. diameter Type E probes were tested with varying L/t parameters. This set of experiments was designed to analyze how mount interference effects at off-angle change with L/t or probe length. The experimental results of the probe L/t study can be seen in Figure 5.13:

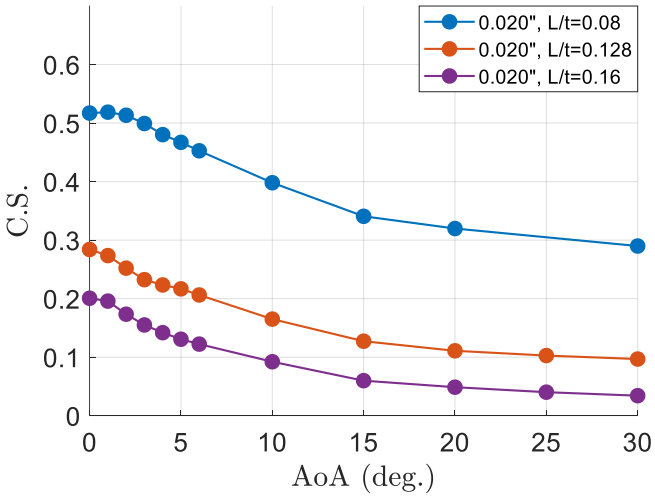

Figure 5.13: Experimental results for L/t study in symmetric strut

The results from Figure 5.13 show that increasing L/t of a probe decreases its C.S. or conduction error. This is consistent with Equation 2.16 which shows that increasing length is an effective way to design for minimal conduction error. However, Figure 5.13 shows that the benefits from increasing length diminish as the length is increased. The diminishing returns can be explained by the fact that there are two effects that are changed when length is increased. The first is the obvious increase in the conduction path length which reduces conduction error, but a second effect is that mount interference effects are reduced when the sensor is far from the strut body. The coupling of these two effects results in large conduction error changes with length when the probe is short but small changes with length for a long probe. Another key feature of Figure 5.13 is that as length varies, the performance trend with angle remains relatively constant. 3D CFD computations were also performed at freestream pitch angles of 0°, 5°, 10°, and 20° for the L/t = 0.128 and L/t = 0.16 probes. These 3D CFD results can be used to identify why the performance trend with angle is not changing when L/t is increased. Figure 5.14 shows surface average h values for the 0.020" L/t = 0.08, 0.128, and 0.16 probe geometries versus angle of attack.

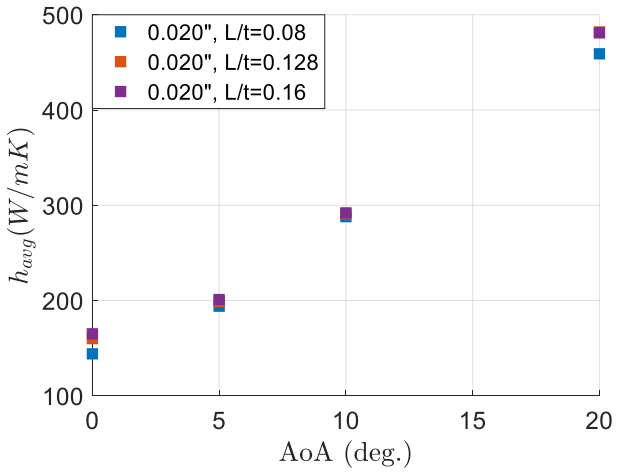

Figure 5.14: CFD/CHT predictions of sensor averaged convection coefficient vs. freestream flow angle for L/t study

It can be seen from Figure 5.14 that the average convection heat transfer coefficient, *h*, is almost completely constant with L/t. There is small variation in *h* at 0° and 20°, but these variations have negligible magnitude compared to *h* changes with flow angle. Additionally, flow visualizations from the 3D CFD results can be used to help identify why the average *h* values remain constant with varying L/t. A plot of streamlines around the L/t = 0.08 and L/t = 0.16 probes with contours of the sensors h with a 10° freestream flow angle can be seen in Figure 5.15.

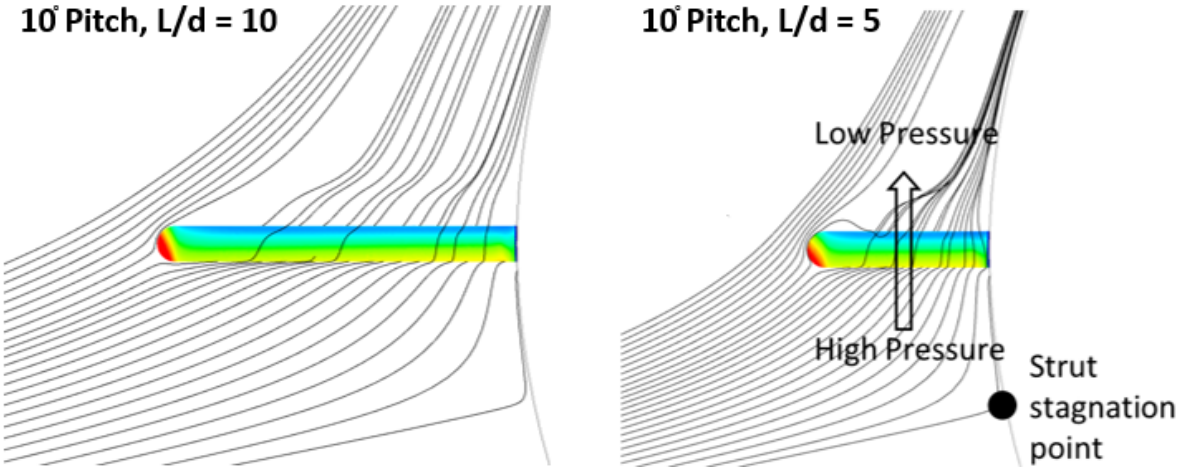

Figure 5.15: CFD/CHT predictions of streamlines around 0.020", L/t = 0.08 and L/t = 0.16 probes, 10° freestream flow angle

The strut stagnation point is independent of the probe geometry; therefore, the pressure gradient and resulting crossflow across the sensor is independent of the total temperature probe's length as seen in Figure 5.15. This means that the, *h*, along the length of the sensor should be relatively constant unless the probe is made so long that the mount influence on the local flow-field is small. The continuous crossflow and constant average h identified by the CFD results agree with and explain the experimental conduction error trend with angle remaining relatively constant when L/t is varied. Flow visualizations for yawed cylinders in crossflow have been discussed in Ramberg (1983) and Shang (2018) [17,40]. This literature similarly analyzes the effects of length, and gives insight into the flow behavior if the total temperature probe configuration was yawed instead of pitched. One important finding from the 3D, CFD results is that the convection heat transfer coefficient at the tip of the sensor will change with length. This is because as the sensor becomes longer, flow with higher velocity is stagnated near the probe tip. However, the increase in tip, *h*, is not large enough to significantly alter an average, *h*, for the probe.

Next, the results of the probe diameter study can be discussed. During the diameter study, three total temperature probes were to be studied, each with a constant L/t while the probe diameter or L/d was varied. However, the measured L/t values of the assembled configurations indicated that both the smaller 0.010 in. diameter probe and the 0.032 in. diameter probe had slightly longer L/t values of 0.096 compared to the nominal 0.020 in. probe with a L/t of 0.08. This resulted in only two probe geometries with a constant L/t that were directly comparable in the diameter study. The experimental results of the diameter study can be seen in Figure 5.16. The collapse of conduction sensitivity (C.S.) on conduction driver was confirmed for each tested probe geometry.

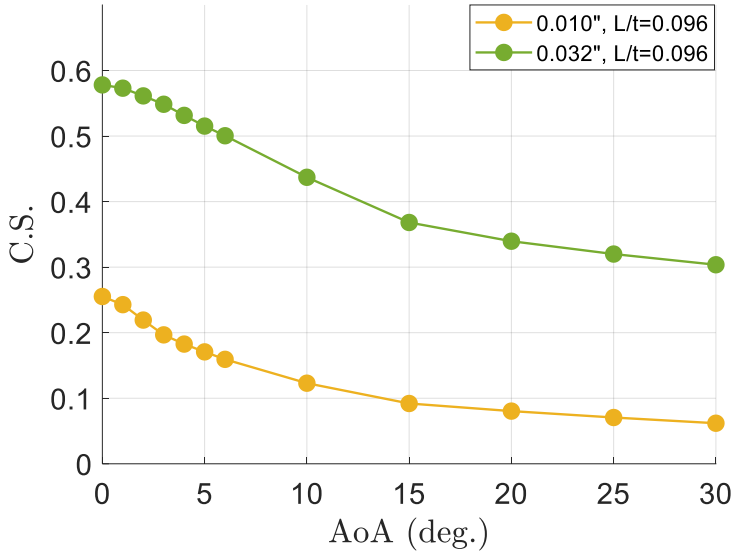

Figure 5.16: Experimental results for probe diameter study in symmetric strut

Figure 5.16 shows that the C.S. and therefore conduction error decreases with diameter. A decrease in diameter creates an increased L/d for conduction which results in the conduction error decrease as predicted by the conduction error Equation 2.16. The diameter also has a small impact on the local flow-field which results in the sensor average, *h*, varying with diameter. This can be seen by the slight difference in curve shape between the 0.010 in. and 0.032 in. probe results in Figure 5.16. 3D CFD computations were also performed at freestream pitch angles of 0°, 5°, 10°, and 20° for the 0.010 in. and 0.032 in. probes. These 3D CFD results can be used to identify how, *h*, changes with diameter. Figure 5.17 shows surface average, *h*, values for the 0.010 in. and 0.032 in. probe geometries versus angle of attack.

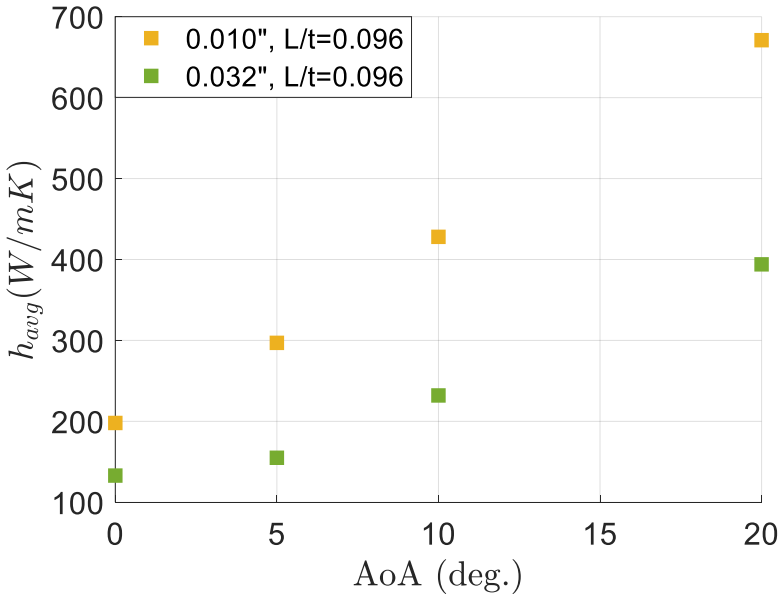

Figure 5.17: CFD/CHT predictions of sensor averaged convection coefficient vs. freestream flow angle for diameter study, 3D CFD results

It can be seen from Figure 5.17 that the sensor averaged convection coefficient, *h*, increases as diameter decreases. Additionally, this increase happens at a larger rate at higher freestream flow angles. This behavior is captured and predicted by the conduction error, low-order models through the Nusselt-Reynolds relationships. Both the Nusselt and Reynolds numbers are dependent on the diameter, and most Nusselt-Reynolds correlations have a Reynolds number raised to a power less than one. This results in an, *h*, prediction that increases as the probe diameter decreases, as seen in Equation 2.8.

Overall, the experimental results and discussed CFD results identify key trends and flow physics regarding how mount interference and flow angle impact unshielded total temperature probes. Unshielded sensors have improved recovery performance at off-angles, but they are very sensitive to freestream flow angle. An unshielded total temperature probe at off-angle behaves very similarly to a cylinder in crossflow which is why probe recovery increases with angle. Additionally, it was identified that a probe's heat transfer coefficient is largely independent of its length. This gained insight indicates that unshielded total temperature probes could be intentionally mounted at a large angle to minimize conduction error and reduce flow angle sensitivity. Similar benefits could also be gained by mounting the probe at a location where the strut is accelerating the flow. The time-averaged, conduction sensitivity values from the experiments that were discussed in this section are summarized in Table 5.2. Similarly, the conduction sensitivity results from the 3D CFD/CHT simulations are summarized in Table 5.3.

Table 5.2: Summary of time-averaged, conduction sensitivity values for all probe geometries and pitch angles experimentally tested on symmetric strut

Pitch Angle (°)	0	1	2	3	4	5	6	10	15	20	25	30
0.020", L/t = 0.08 Probe C.S.	0.517	0.519	0.513	0.499	0.480	0.467	0.453	0.398	0.341	0.320	N/A	0.290
0.020", L/t = 0.128 Probe C.S.	0.284	0.274	0.252	0.232	0.223	0.217	0.206	0.165	0.127	0.111	0.103	0.097
0.020", L/t = 0.16 Probe C.S.	0.201	0.196	0.173	0.155	0.142	0.131	0.122	0.092	0.060	0.049	0.040	0.034
0.010", L/t = 0.096 Probe C.S.	0.255	0.243	0.219	0.197	0.183	0.171	0.159	0.123	0.092	0.080	0.071	0.062
0.032", L/t = 0.096 Probe C.S.	0.578	0.573	0.561	0.549	0.532	0.515	0.500	0.437	0.368	0.340	0.320	0.304

Table 5.3: Summary of conduction sensitivity values calculated from 3D CFD/CHT results, symmetric strut

Pitch Angle (°)	0	5	10	20
0.020", L/t = 0.08 Probe C.S.	0.627	0.564	0.469	0.346
0.020", L/t = 0.128 Probe C.S.	0.364	0.312	0.226	0.128
0.020", L/t = 0.16 Probe C.S.	0.244	0.203	0.135	0.067
0.010", L/t = 0.096 Probe C.S.	0.288	0.199	0.130	0.068
0.032", L/t = 0.096 Probe C.S.	0.669	0.639	0.551	0.415

5.5 Unsteady and Cambered Conduction Error Experiment Results

In this section, the results from the additional conduction error experiments described in Section 4.6 will be presented. An experimental investigation into how freestream forced unsteadiness impacts off-angle total temperature probe performance was conducted. This study utilized an upstream cylinder to induce a shedding wake and was performed on the nominal 0.020", L/d = 5 probe. The results from this study compared with the steady nominal probe results can be seen in Figure 5.18.

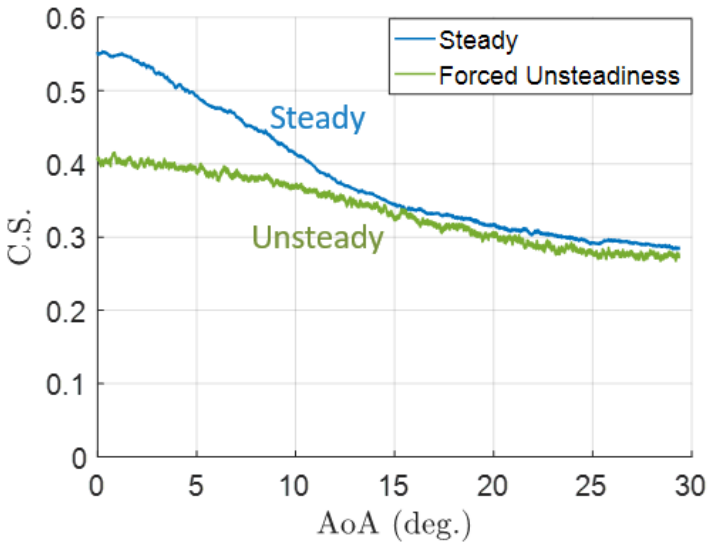

Figure 5.18: Experimental impacts of forced unsteadiness on unshielded total temperature probe, 0.020" O.D., L/d = 5

The results from Figure 5.18 show that at low angles, freestream unsteadiness significantly reduces conduction error. This is because the unsteadiness increases convection to the temperature sensor.

Additionally, it can be seen that the performance at high angles is similar between the steady and unsteady results. This indicates that the convection at high angles is dominated by the strut geometry because of the induced crossflow. Therefore, total temperature sensors positioned at large angles or in the strut acceleration region should be insensitive to changes in the freestream. The results in Figure 5.18 also show that freestream unsteadiness greatly reduces a total temperature probe's sensitivity to angle of attack. This can be seen by the C.S. decrease between 0° and 30° dropping by half for the unsteady results compared with the steady measurements.

Next, an experimental investigation was performed to assess whether the closed test section walls had an impact on the results presented in Section 5.5. A pitch angle sweep using the symmetric strut and nominal 0.020 in., L/d = 5 probe was performed using a modified open test section. This experiment was performed an entire year after the original experiment using a new probe but the same assembly method and geometry. The results from the open test section test compared to the original closed test section test can be seen in Figure 5.19.

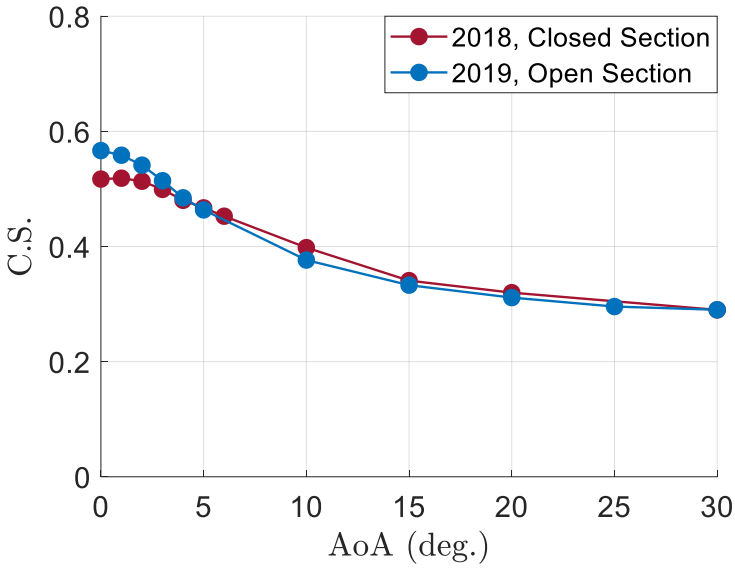

Figure 5.19: Virginia Tech Open Jet Wind Tunnel test section influence, experimental results for 0.020" O.D., L/d = 5 probe

The results agree well between the 2018 closed test section test and the 2019 open test section test. However, there is a small difference between the results at 10° pitch angle and at low angles between 0-2°. The difference at the 10° case is expected to be caused by physical differences in the flow over the airfoil. As previously discussed, multiple flow solutions at a single pitch angle were witnessed in the experiment at higher test velocities. A 10° angle of attack was the most common angle that multiple flow states were encountered at higher velocities. Therefore, it is likely that different flow states are still able to occur at the 10° positioning even at the lower freestream velocity. Meanwhile, the difference at low angles between 0-2° is expected to be caused by the influence of the tunnel walls in the closed test section. Figure 5.20 shows a comparison of the two experimental results along with results from the 3D CFD simulations of the nominal 0.020 in., L/d = 5 probe geometry.

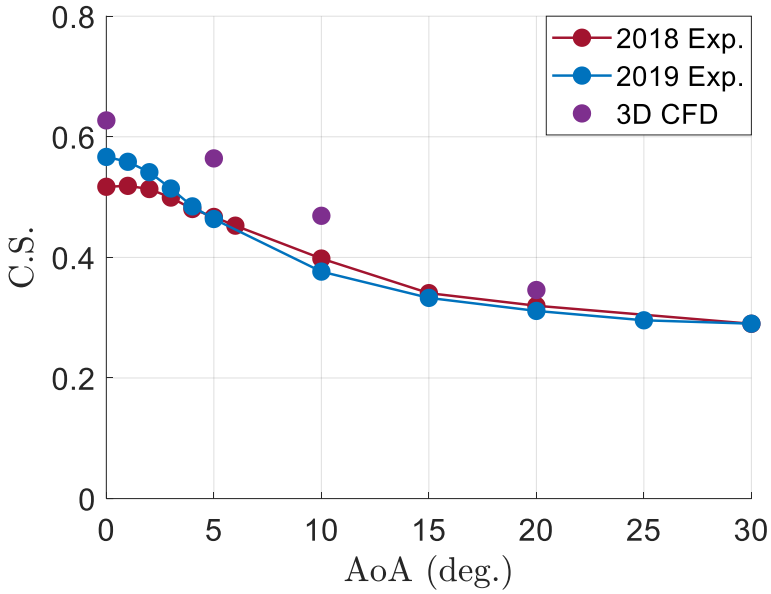

Figure 5.20: 3D CFD results vs Virginia Tech Open Jet Wind Tunnel test section influence, 0.020" O.D., L/d = 5

The 3D CFD results feature curvature similar to the 2019 open test section experiment results. The 3D CFD simulations were performed with pressure far-field boundary conditions which would be more representative of the open test section configuration. The fact that the 3D CFD results and open test section experiment have closer C.S. values and slopes indicates that the closed test section walls reduced the C.S. or conduction error at very low angles. This is counterintuitive, but can be explained thanks to the insight gained from the forced unsteadiness experiment. When the strut/sensor assembly is placed in the closed test section, the walls force additional acceleration around the airfoil due to the blockage caused by the strut's presence. This increased velocity increases the sensor, *h*, which results in the decrease in C.S. that is seen at very low angles in Figure 5.19. However, at moderate angles the strut geometry influence is expected to dominate the sensor performance which would reduce the impact of the walls and results in similar performance between the closed and open test sections. Overall, the agreement between these two tests greatly supports the repeatability and accuracy of the presented conduction error experiments.

Finally, an experimental investigation was performed to analyze how the impact of mount interference and freestream flow angle changes when the mounting strut features camber. A cambered trailing edge was attached to the symmetric strut utilized in the previous experiments, and the nominal 0.020 in., L/d = 5 probe was tested. All angles in the cambered strut experiment will be defined relative to the total temperature probe alignment. At 0° the probe is still aligned with the freestream flow; however, the new cambered strut geometry is positioned at an angle relative to its chord line. The experiment results for the cambered strut test can be seen in Figure 5.21.

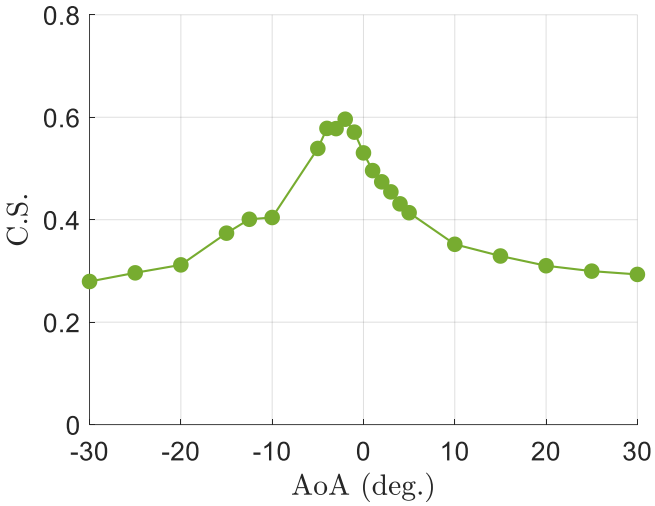

Figure 5.21: Experimental results for 0.020", L/d = 5 (L/t = 0.08) probe in cambered strut

The cambered strut experiment results show a nonsymmetric performance profile as expected. The C.S. trend with positive angles behaves very similarly to the performance trends seen with the symmetric strut. However, the negative angle C.S. curve, where the leading edge is pitched down, has several unique features not seen in the symmetric strut experiments. First, the maximum conduction error occurs around -2° to -4°. This indicates that the strut stagnation point coincides with the total temperature probe base location in this angle range. Additionally, there is a performance plateau between -10° and -12.5°. This performance plateau was identified during a continuous angle sweep and is most likely a feature of the cambered strut geometry at the tested flow conditions. This feature will be discussed further in Section 5.7 when compared with low-order model predictions. Overall, the cambered strut results show that the main performance trends identified during the symmetric strut studies hold true for more complex airfoil geometries. The maximum conduction error location or effective "zero" angle is simply shifted based on the amount of camber and leading-edge profile. Consequently, the continuous C.S. decrease with increasing angle, and relative C.S. insensitivity to angle at high angles can still be seen in the cambered strut results.

5.6 Various Conduction Error Low-Order Model Predictions

The developed low-order method to account for mount interference effects, named the virtual probe method (VPM), was utilized to predict the conduction error of each experimentally tested total temperature probe. Predictions using different conduction models and Nusselt-Reynolds correlations were then compared to determine whether the virtual probe method could be used with prior conduction models to account for mount interference and flow angle effects. First, low-order predictions for the symmetric strut experiments were performed. In order to use the virtual probe method with a conduction model described in Section 2, a solution to the flow-field around the desired strut is required. Additionally, to predict pitch angle sweeps matching the experiment results, a flow-field solution is needed for every freestream flow angle of interest. Therefore, 2D

CFD simulations with ANSYS Fluent were performed for the symmetric strut at freestream flow angles of 0°, 5°, 10°, and 20°. The freestream flow conditions from the experiment were matched in the 2D CFD simulations. The strut geometry was acquired by tracing the experimental strut, and then a spline was utilized to create a CAD file of the strut geometry. 2D CFD simulations were used to acquire the flow-field solution for conduction error predictions instead of a potential flow method or panel method because separation off the large t/c strut was expected and this separation needed to be accounted for to provide an accurate flow-field solution. Contours of velocity magnitude acquired from the 2D CFD solutions can be seen in Figure 5.22:

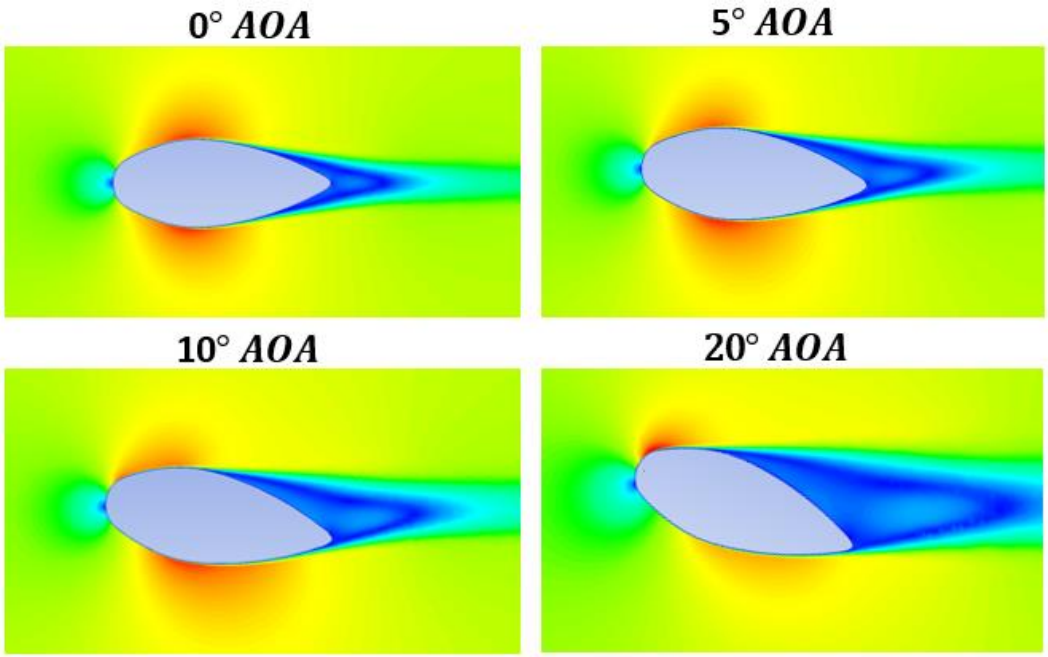

Figure 5.22: Total velocity contours used for virtual probe method, symmetric strut

The contours in Figure 5.22 show that indeed the airfoil has trailing edge separation even at a 0° angle of attack. This separation occurs after the maximum thickness and is a fairly small region at 0°. However, at larger angles of attack separation occurs right at or before the maximum thickness on the suction side of the airfoil, and the stagnation region becomes very large. For the nominal 0.020 in. L/d = 5 probe, a virtual probe line of length 0.10 in. is used to extract a velocity profile from each flow-field solution. This velocity profile is extracted from the strut surface where the base of the sensor would be located to 0.10 in. away from the strut where the tip of the temperature sensor would be located. An illustrated example of a virtual probe line was shown in Figure 2.2. The velocity profile for each virtual probe line extracted from the symmetric strut 2D CFD solutions can be seen in Figure 5.23. The plot in Figure 5.23 shows the total velocity normalized with the freestream velocity versus the normalized position along the probe length. The high slopes at small x/L values indicate the velocity increase through the boundary layer. It can be seen that at low angles the velocity continuously increases with x/L since the probe location is moving away from the strut stagnation point. However, at large angles, the flow velocity is immediately large after the boundary layer and remains relatively constant along the probe length due to the presence of strut induced crossflow.

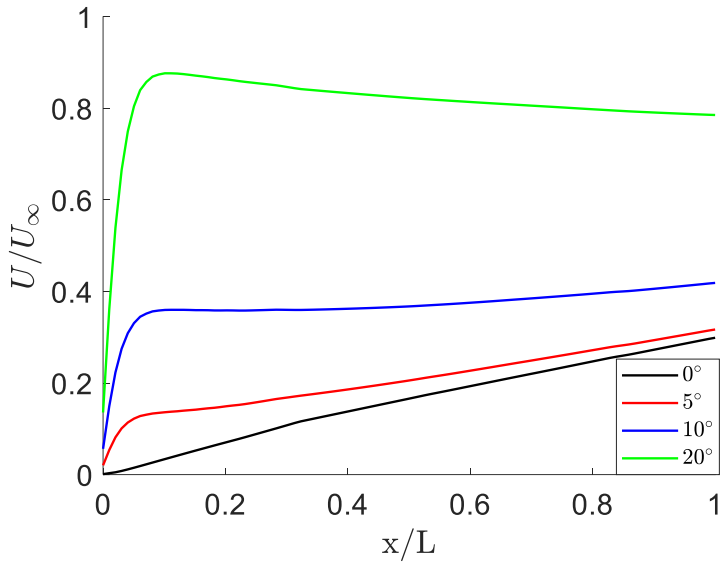

Figure 5.23: Virtual probe lines from symmetric strut 2D CFD solutions

Next, the velocity along each virtual probe line is averaged to get an average local velocity for the nominal probe from each contour. Each averaged velocity is then used in the Reynolds number equation seen in Equation 2.5 to calculate a local Reynolds number that accounts for mount interference effects. This local Reynolds number can then be used with a Nusselt-Reynolds correlation to predict the nominal probe's average film coefficient h for each freestream angle of attack. The Moffat correlation for a bare-wire thermocouple in perpendicular flow, seen in Equation 2.19, was initially used due to the crossflow seen across unshielded total temperature sensors at any moderate freestream flow angle. Finally, the predicted h values can be used in a conduction error model along with the probe geometry and effective thermal conductivity. The reformulated conduction sensitivity parameter will be used to evaluate all conduction error predictions since it allows a probe conduction error to be analyzed independent of conduction driver. The conduction sensitivity formulation found in Equation 2.17 was initially used for predictions. This equation is a form of the base conduction model seen in Equation 1.11, but is enhanced by dropping the insulated tip assumption. The predicted results using the virtual probe method, perpendicular Moffat correlation, and enhanced conduction model compared with the experiment results for the nominal probe can be seen in Figure 5.24.

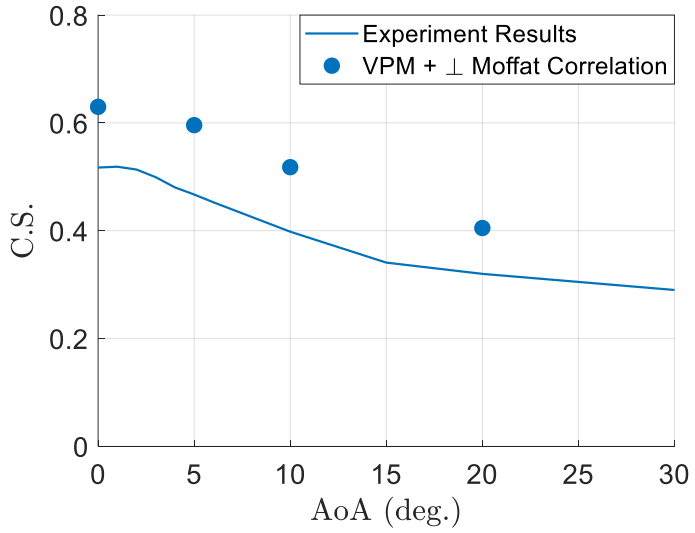

Figure 5.24: Comparison of experiment results and predictions using Virtual Probe Method with Moffat perpendicular flow correlation and enhanced conduction model, 0.020" L/d = 5 probe

Figure 5.24 shows that the low-order predictions estimate a C.S. higher than the experiment results for all flow angles. However, the predicted C.S. trend with flow angle appears to match the experiment results well. The trend agreement indicates that the virtual probe method is successfully capturing the effects of mount interference and freestream flow angle. The constant delta between the predictions is most likely due shortcomings of the utilized Nusselt-Reynolds correlation or inaccuracies in the physical properties used in the predictions. Therefore, the utilized Nusselt-Reynolds correlation will be assessed. Additionally, the uncertainty of each physical property used in the low order predictions will be discussed in detail in Section 5.8.

The Moffat correlation for a bare-wire thermocouple in perpendicular flow was expected to accurately predict, *h*, at moderate and high angles since the strut induced crossflow results in a local flow angle across the sensor that is much larger than the freestream flow angle. However, there are other known Nusselt-Reynolds correlations that could potentially better model parts of an unshielded total temperature sensors performance. For instance, the Moffat correlation for a wire in parallel flow is expected to better predict h at 0° and low angles. Additionally, the Churchill and Bernstein correlation for a cylinder in a crossflow, seen in Equation 2.18, is expected to represent the flow behavior at high angles along the length of the sensor, but does not capture tip effects since the correlation is developed for an infinitely long cylinder. A study was performed to assess each of the three discussed Nusselt-Reynolds correlations along with the impact of the insulated tip assumption. Low-order predictions were made using the virtual probe method, each the three discussed Nusselt-Reynolds correlations, and the enhanced conduction sensitivity model seen in Equation 2.17. Additionally, predictions were made using the virtual probe method, perpendicular flow Moffat correlation, and the original conduction model assuming an insulated tip. The results from each of these predictions along with experimental results for the nominal 0.020 in. L/d = 5 probe can be seen in Figure 5.25.

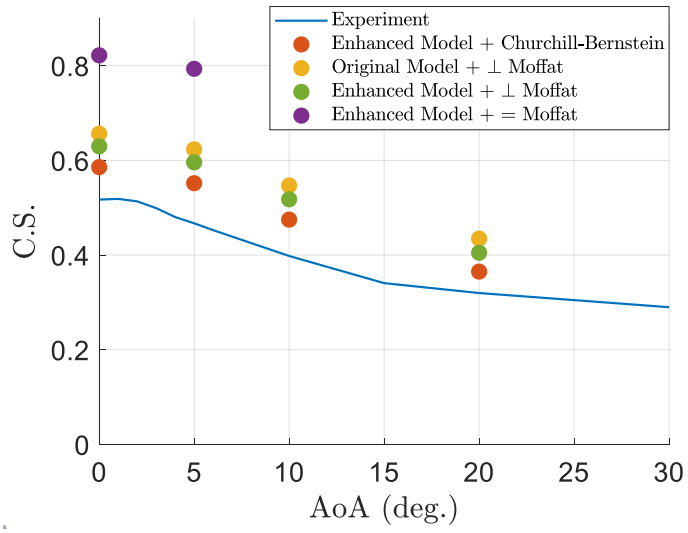

Figure 5.25: Comparison of predictions using Virtual Probe Method, enhanced conduction model and three different Nu-Re correlations. Additional Moffat, Perp. flow predictions performed with standard conduction model, 0.020" L/d = 5 probe

The results in Figure 5.25 show the virtual probe method allows predictions with each of the Nusselt-Reynolds correlations to correctly capture the effects of freestream flow angle. The impact of the insulated tip assumption in the conduction error equation can be seen by comparing the yellow and green results in Figure 5.25. These results show that removing the insulated tip assumption improves prediction accuracy; however, the error introduced by that assumption is relatively small. Meanwhile, the accuracy of different Nusselt-Reynolds correlations can be seen by comparing the purple, red, and green results in Figure 5.25. Moffat's correlation for a bare-wire thermocouple in parallel flow was expected to be most accurate at 0°. However, the prediction results show that this correlation is inaccurate even at low angles. This could be due to the probe geometries used to develop Moffat's correlation experiencing separation off of the bead or junction at low angles which would greatly impact the heat transfer on the downstream wires. This type of flow feature would not be present with the current sheathed thermocouples at low angles.

The Moffat correlation for a wire in perpendicular flow and the Churchill-Bernstein correlation both result in predictions much closer to the experiment results. Although the two correlations have similar performance, the Churchill-Bernstein correlation predicts larger average, *h*, values which results in slightly lower C.S. predictions that agree better with the experiment results. As previously mentioned, the Churchill-Bernstein correlation is expected to better capture the flow physics around the probe if tip effects are negligible. Meanwhile the Moffat perpendicular flow correlation is expected to better capture the flow physics relating to tip effects and their impact on the heat transfer along a probe side, but less accurately represent crossflow across a cylinder. Therefore, the flow physics relating to off-angle sheathed temperature sensors is not fully captured by either correlation, but performing predictions with both correlations should provide a good performance estimate without developing a new correlation or performing full-scale 3D, CFD simulations.

The 3D CFD computations that were previously discussed can be used as an additional point of comparison between the experiments and the low-order model predictions. Temperature solutions from the 3D CFD simulations were used to calculate the C.S. performance vs freestream flow angle for the nominal 0.020 in., L/d = 5 probe. These results compared to the experiments and low order predictions can be seen in Figure 5.26.

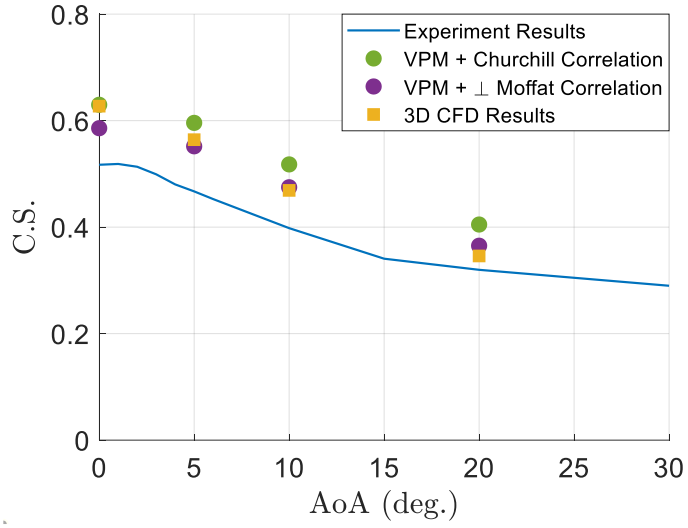

Figure 5.26: Comparison between experiments, 3D CFD results, and predictions using Virtual Probe Method, enhanced conduction model, and Churchill-Bernstein and ⊥ Moffat correlations, 0.020" L/d = 5 probe

The 3D, CFD results predict C.S. values that are also higher than the experiment results but show good agreement with the low-order predictions. This indicates that uncertainty in the experimental measurements or physical properties used for predictions may be causing the difference between the experiments and predictions. This uncertainty will be discussed and quantified in Section 5.8. The 3D, CFD results show good agreement with Moffat's perpendicular flow correlation at low angles, but closer agreement to the Churchill-Bernstein correlation at higher angles. This makes sense based on the known strengths of each correlation and the fact that tip effects are expected to be greatest at low angles and then continuously decrease with increasing angle as the strut induced crossflow becomes more uniform.

Now that various low-order model predictions have been assessed for the nominal 0.020 in., L/d = 5 probe, the virtual probe method, enhanced conduction model, and selected Nusselt-Reynolds correlations can be used for predictions of all five tested probe geometries. These predictions will help show how the accuracy varies with probe geometry and the robustness of the developed prediction method. Since the Churchill-Bernstein and Moffat perpendicular flow correlations were identified to each contain separate relevant physics, low-order predictions were made with both correlations. The experiment results and predictions using the virtual probe method, enhanced conduction model, and corresponding correlation for the L/t study can be seen in Figure 5.27. Additionally, experiment results and predictions for the diameter study can be seen in Figure 5.28.

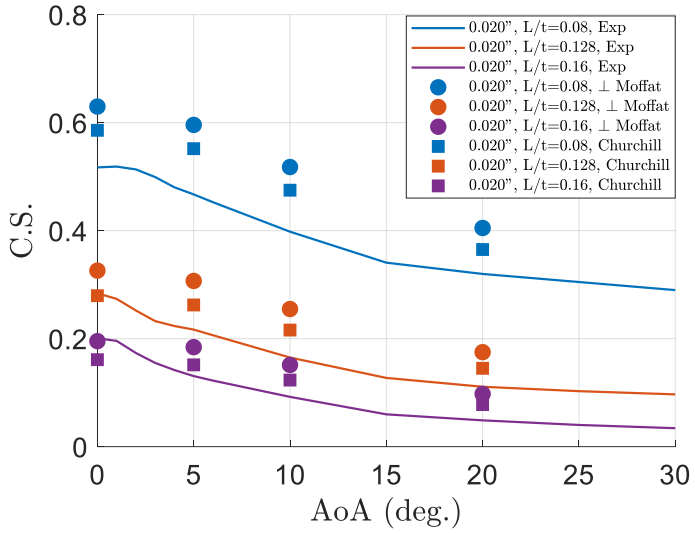

Figure 5.27: Comparison of experiments and low-order predictions using Virtual Probe Method, enhanced conduction model, and Churchill-Bernstein and ⊥ Moffat correlations. Symmetric strut, for the L/t variation study

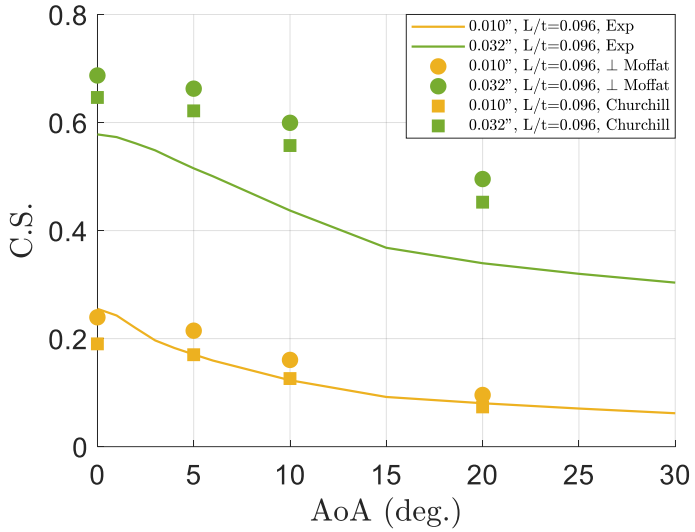

Figure 5.28: Comparison of experiments and low-order predictions using Virtual Probe Method, enhanced conduction model, and Churchill-Bernstein and ⊥ Moffat correlations. Symmetric strut, for the diameter variation study

Overall, the low-order model predictions accurately predict how length and diameter will impact total temperature probe performance. Additionally, the impact of mount interference and freestream flow angle is accurately captured for most of the tested probe geometries. The worst agreement between predicted and experimental curve shapes is for the 0.020 in. L/t = 0.16 probe. It can be seen in Figure 5.27 that the predictions for this sensor have a flatter slope than the measured experiment results. This occurs for the longest probe because the average, *h*, approximation weakens as sensor length increases. In off-angle conditions, the average, *h*, remains relatively constant with length, but the tip, *h*, greatly increases with length, since mount

interference near the tip decreases. The impact of the probe tip, *h*, is neglected by the average, *h*, approximation, but this regions importance grows as length increases since the tip, *h*, values greatly increase. This error could be eliminated if a more complex conduction error model was used, such as that seen in Equation 2.18. Finally, the experimental results and low-order predictions were compared with the 3D, CFD results for all five probe geometries. A comparison of the experimental results, 3D, CFD results, and predictions using the virtual probe method, enhanced conduction model, and corresponding correlations for the L/t study can be seen in Figure 5.29. Additionally, a comparison of experimental results, 3D CFD results, and low-order predictions for the diameter study can be seen in Figure 5.30.

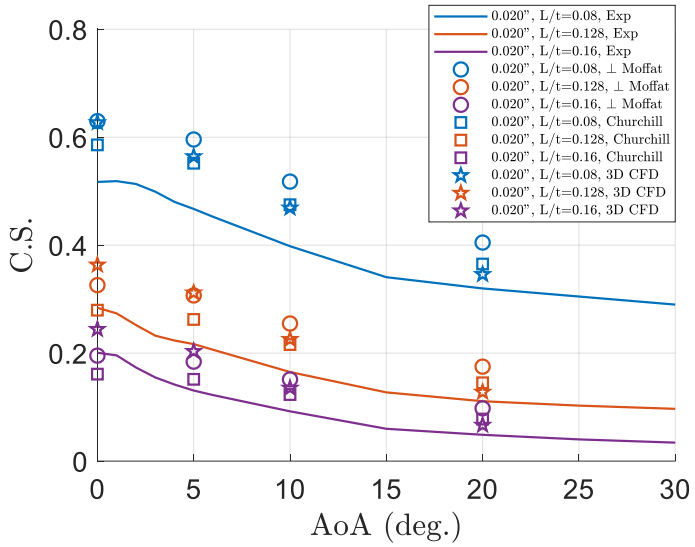

Figure 5.29: Comparison between experiments, 3D CFD, and low order predictions using Virtual Probe Method, enhanced conduction model, and Churchill-Bernstein and Moffat perpendicular flow correlations. Symmetric strut, for the L/t variation study

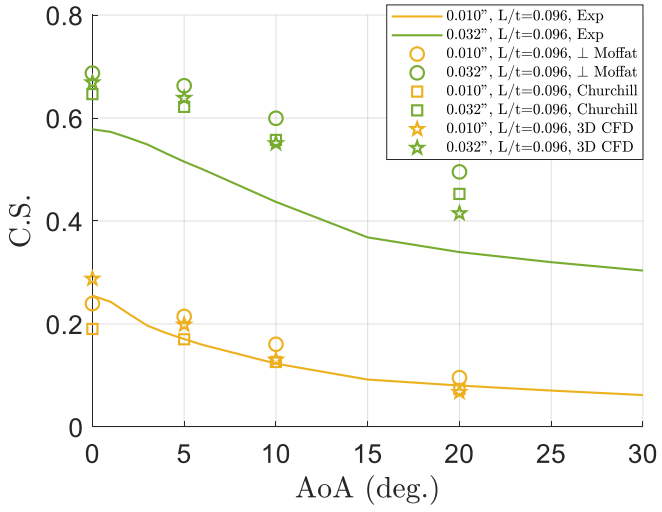

Figure 5.30: Comparison between experiments, 3D CFD, and low order predictions using Virtual Probe Method, enhanced conduction model, and Churchill-Bernstein and Moffat perpendicular flow correlations. Symmetric strut, for the diameter variation study

The 3D, CFD results support the low-order model predictions for each probe geometry. Once again, the 3D, CFD results show good agreement with Moffat's perpendicular flow correlation at low angles, but closer agreement to the Churchill-Bernstein correlation at higher angles. This behavior holds true for all five probe geometries and shows that the assessment of different Nusselt-Reynolds correlations for the nominal probe should be relevant for all tested probe geometries.

Next, low-order predictions using the virtual probe method were performed for the 0.020 in. L/d = 5 probe tested on a cambered strut. These predictions were performed to assess if the virtual probe method can accurately account for mount interference and flow angle effects when a more complex cambered strut geometry is present. In order to perform predictions using the virtual probe method for the cambered strut, 2D, CFD computations were run to acquire the flow field solution around the cambered airfoil. Contours of total velocity around the cambered strut can be seen in Figure 5.31 for six of the analyzed flow angles. 2D, CFD simulations were run for the cambered strut at freestream flow angles of -20°, -12.5°, -10°, -5°, -2.5°, 0°, 5°, and 10°.

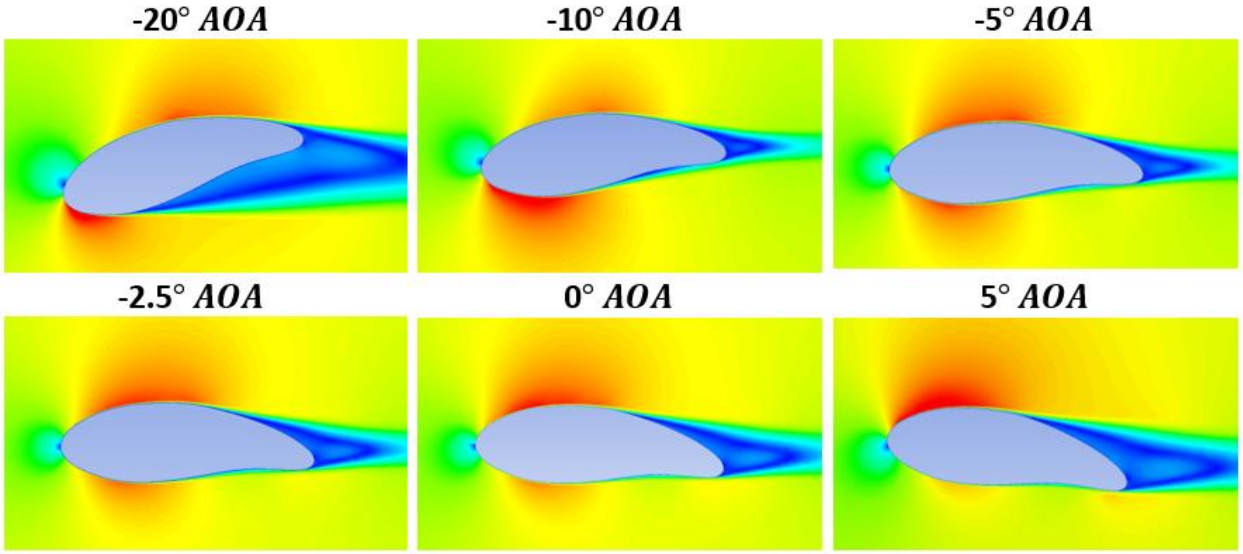

Figure 5.31: Total velocity contours used for virtual probe method, cambered strut

It can be seen from Figure 5.31 that the flow field around the cambered strut is significantly different than the flow-fields for the symmetric strut. The stagnation point is shifted off the base probe location at 0°, and large asymmetries in the flow-field are present at all freestream flow angles. A virtual probe line was used to extract a local velocity profile for the nominal probe geometry for each flow angle case. A plot of these local velocity profiles nondimensionalized by the freestream velocity versus the nondimensional length along the nominal probe can be seen in Figure 5.32.

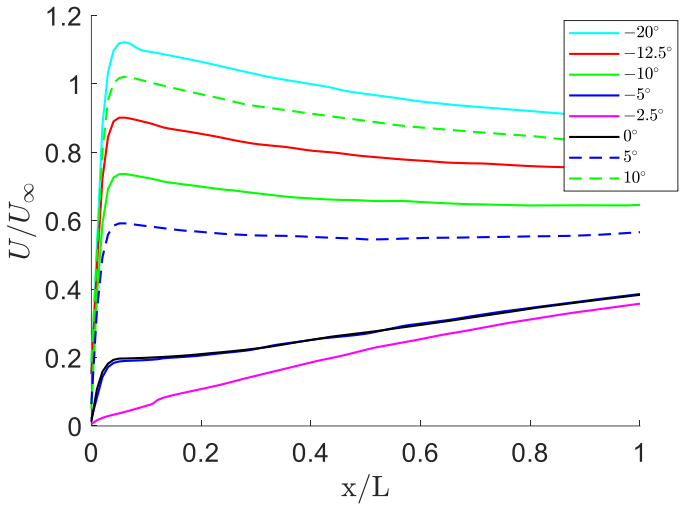

Figure 5.32: Virtual probe lines from cambered strut 2D, CFD solutions

These local velocity profiles help identify performance features before conduction error predictions are even calculated. It can be seen from Figure 5.32 that the lowest velocity occurs near -2.5°. This indicates that the maximum C.S. will occur around this angle. Additionally, the 0° and 5° cases have the same local velocity profiles and are therefore expected to have the same conduction error and performance. A comparison of the symmetric strut velocity profiles with some cambered strut velocity profiles, seen in Figure 5.33. This can be used to identify how performance will change with strut geometry and illustrates why the virtual probe method is extremely effective.

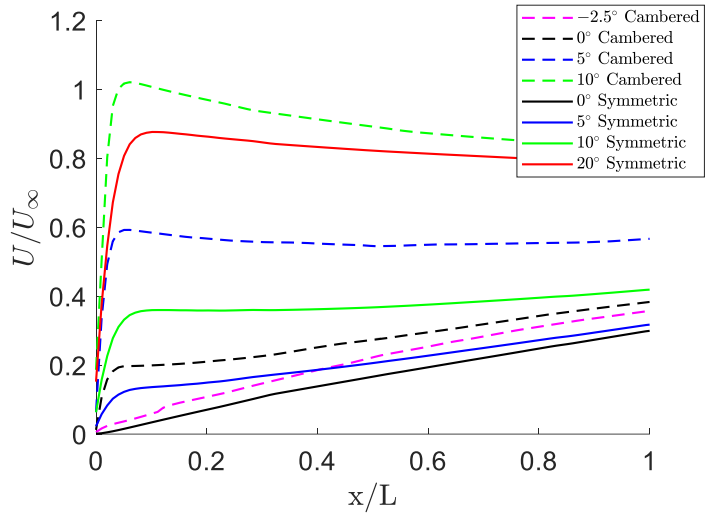

Figure 5.33: Comparison between symmetric strut and cambered strut virtual probe lines

It can be seen that the cambered -2.5° velocity profile behaves very similarly to the 0° symmetric strut case. This similarity occurs because the strut stagnation region is on the temperature probe's base in both cases. Similarly, the difference in velocity profiles between the cambered and symmetric results at 5° and 10° illustrates how mount interference and flow angle effects are

captured and why the same probe geometry will have a different performance if strut geometry is changed.

Finally, the local velocity profiles can be used to calculate a local Reynolds number, and conduction error can be predicted. A comparison of the cambered experiment results and low-order predictions using the virtual probe method, enhanced conduction model, and the Churchill-Bernstein and Moffat perpendicular correlations for the nominal probe on a cambered strut can be seen in Figure 5.34.

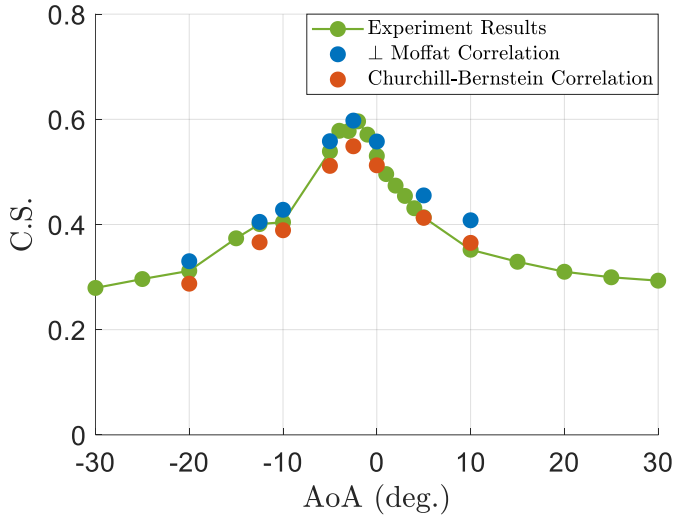

Figure 5.34: Comparison of cambered experiment results and predictions using Virtual Probe Method, enhanced conduction model, and both the Moffat perpendicular correlation and Churchill-Bernstein correlation, 0.020 in. L/d = 5 probe

The low-order predictions for the cambered strut have very good agreement with the experiment results. The performance trend with angle is captured well by utilizing the virtual probe method and both correlations are able to provide close estimates of the C.S. magnitude. The results show that the Moffat perpendicular correlation provides a more accurate estimate at high C.S. values while the Churchill-Bernstein correlation provides a more accurate estimate at higher angles with lower C.S. values. This supports the trends seen for the Moffat and Churchill-Bernstein correlations with the symmetric strut. Overall, the comparisons provided in this section show that the virtual probe method is capable of capturing mount interference and flow angle effects, and can be used with known conduction error models to effectively predict conduction error for unshielded total temperature probes in the presence of a mounting strut or freestream flow angle.

5.7 Conduction Error Results – Uncertainty Quantification

This section will discuss the amount of variation in the conduction error experiment results, and a formal uncertainty analysis will be presented to determine the total uncertainty in the experiment and low order conduction sensitivity predictions. During the discussed symmetric strut experiments, around 6000 samples of data were acquired for each configuration at every tested

angle. The standard deviation of this data for each freestream flow angle was calculated. The symmetric strut conduction sensitivity results with $\pm$ 2 standard deviations for the L/t and diameter studies can be seen in Figure 5.35.

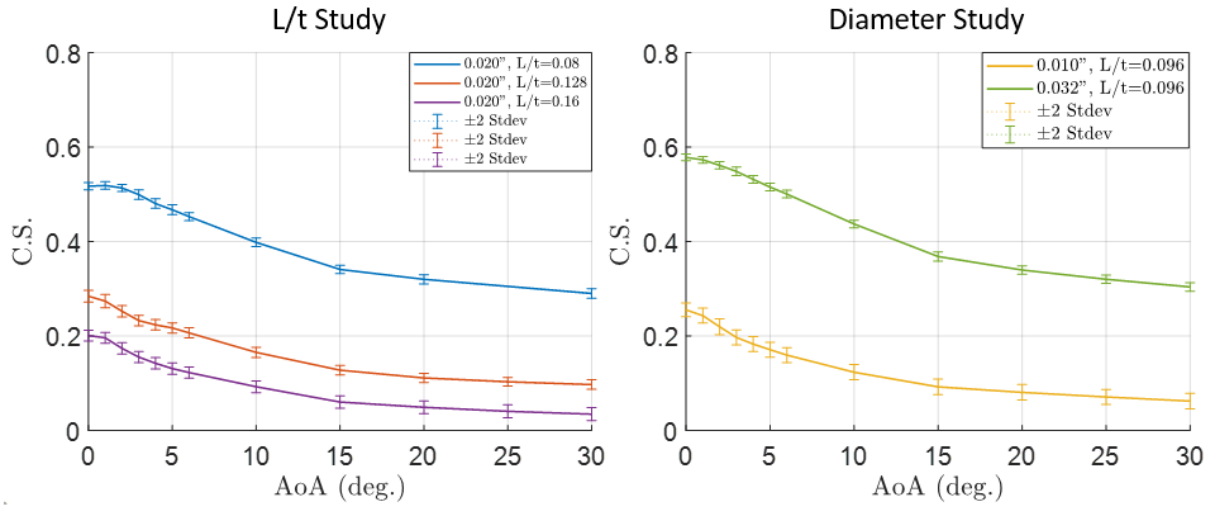

Figure 5.35: Symmetric strut conduction sensitivity results with $\pm$ 2 standard deviations, L/t and diameter studies

The standard deviation magnitude appears to remain relatively constant with angle, but varies greatly between different total temperature probe configurations. The 0.010" diameter temperature sensor and the L/t = 0.16 sensor have the largest standard deviations. However, overall the standard deviations are very small for all of the tested symmetric strut configurations.

A formal uncertainty analysis for the conduction error experiments will be presented below. The experiment conduction sensitivity results are a function of the measured junction temperature, measured base temperature, and the total temperature of the flow which can be seen in Equation 5.10. The Kline & McClintock method previously discussed was again used to develop an equation for the total uncertainty in the conduction sensitivity results. This developed equation is a function of the individual uncertainties in each of the three measured temperatures and can be seen in Equation 5.11. Each of the partial derivatives in Equation 5.11 were evaluated and can be seen in Equation 5.12.

$$CS = f(T_j, T_b, T_t) \tag{5.10}$$

$$\delta CS = \sqrt{(\frac{\partial R}{\partial T_j} * \delta T_j)^2 + (\frac{\partial R}{\partial T_b} * \delta T_b)^2 + (\frac{\partial R}{\partial T_t} * \delta T_t)^2} \tag{5.11}$$

$$\frac{\partial CS}{\partial T_j} = -\frac{1}{-T_b+T_t}, \quad \frac{\partial CS}{\partial T_b} = \frac{-T_j+T_t}{(-T_b+T_t)^2}, \quad \frac{\partial CS}{\partial T_t} = \frac{1}{-T_b+T_t} - \frac{-T_j+T_t}{(-T_b+T_t)^2} \tag{5.12}$$

The individual uncertainties of the three temperature measurements were determined based on uncertainty values provided by the sensor manufacturer. The type E thermocouples that were utilized had individual uncertainties of the greater of 1 C or 0.4%. Meanwhile, the type T thermocouples that were utilized had individual uncertainties of the greater of 0.5 C or 0.4%. For

all of the measured temperatures, 0.4% uncertainty provided a higher individual uncertainty and was therefore used for total uncertainty quantification. The total uncertainty in the experiment conduction sensitivity results was calculated for each probe geometry and every flow angle that was tested. The symmetric strut conduction sensitivity results and total uncertainty bounds for the L/t and diameter studies can be seen in Figure 5.36.

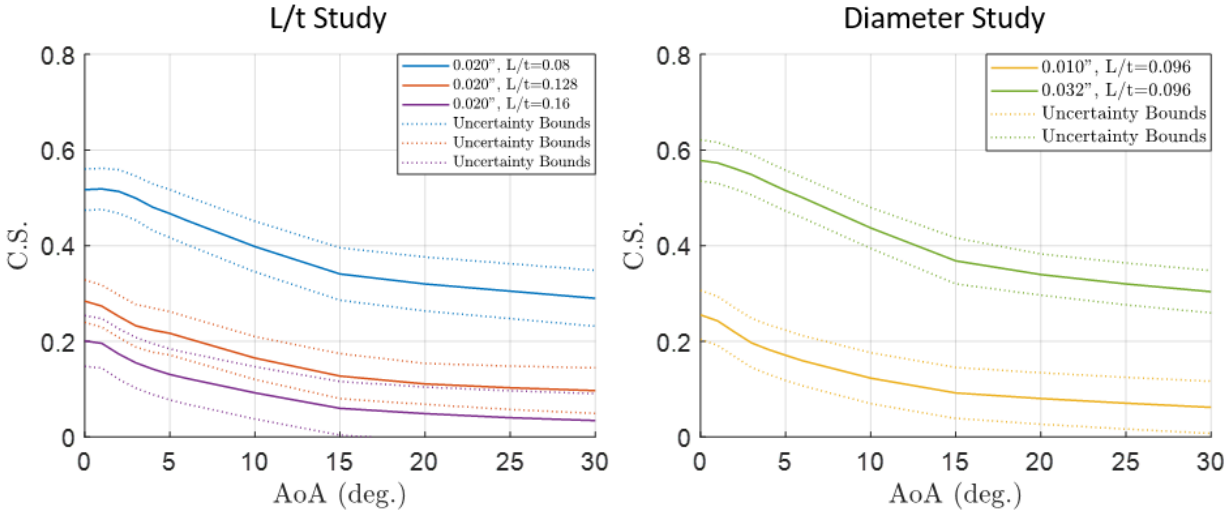

Figure 5.36: Symmetric strut conduction sensitivity and total uncertainty results for L/t and diameter studies

The total uncertainty in the experiment conduction sensitivity results is significant and can be seen to increase slightly with freestream flow angle. This increase occurs because the experimental conduction driver decreases as angle increases due to larger h values on the sensor. The magnitude of the total uncertainty is therefore dependent on the conduction driver, but it is primarily set by the individual uncertainty values that were provided for the utilized thermocouples. The same total uncertainty quantification was performed for the cambered strut experiment results and the cambered strut conduction sensitivity and total uncertainty bounds can be seen in Figure 5.37.

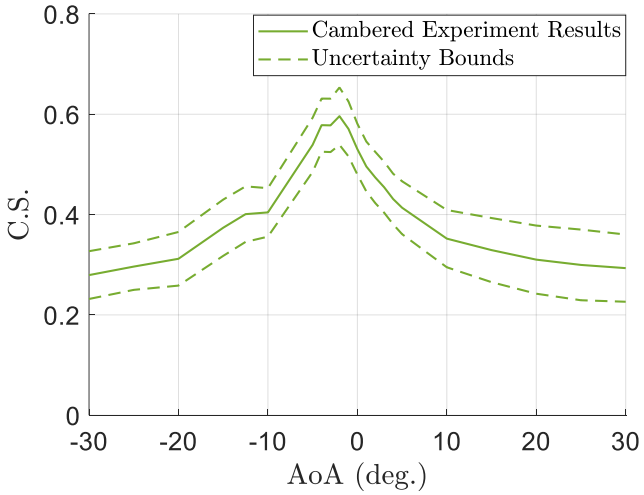

Figure 5.37: Cambered strut conduction sensitivity and total uncertainty

The cambered strut total uncertainty more clearly shows that the uncertainty increases with angle due to decreasing conduction drivers. It can also be seen that the total uncertainty is different at positive and negative high angles even though the conduction sensitivity values are very similar. This is due to different amounts of base heating even though the temperature ratio expressed in the conduction sensitivity parameter is the same.

A formal uncertainty analysis was also performed for the conduction error low-order predictions. The enhanced conduction error model seen in Equation 2.17 was used for this uncertainty analysis. The low order conduction sensitivity formulation is significantly more complex than the equation needed for experiments. Equation 5.13 shows that the low order conduction sensitivity results are a function of the sensor length, sensor diameter, the effective thermal conductivity of the sensor, and the average convection film coefficient, *h*. This assumes an individual uncertainty for *h* instead of including *h*'s dependent variables in the total uncertainty analysis. Using the Kline and McClintock method, Equation 5.14 can be developed for the total uncertainty of the low order conduction sensitivity results.

$$CS = f(\mathrm{L}, \mathrm{d}, k_{tc}, h) \tag{5.13}$$

$$\delta CS = \sqrt{(\frac{\partial R}{\partial \mathrm{L}} * \delta \mathrm{L})^2 + (\frac{\partial R}{\partial \mathrm{d}} * \delta \mathrm{d})^2 + (\frac{\partial R}{\partial k_{tc}} * \delta k_{tc})^2 + (\frac{\partial R}{\partial h} * \delta \mathrm{h})^2} \tag{5.14}$$

The partial derivatives seen in Equation 5.14 were each evaluated; however, the formulas will not be presented here due to the length and complexity of the partial derivatives. The low-order predictions were performed using input parameters meant to replicate those present in the performed experiments. Therefore, the individual uncertainty in each input parameter is dependent on how well the corresponding value is known in the experiments. The sensor diameter was measured with a caliper for each tested temperature probe. The diameter was always found to be very close to the manufacturer specified diameter and had extremely low variability. Therefore, a 0.002 in. uncertainty in the sensor diameter was used for this analysis. Meanwhile, the temperature sensor was hand positioned at the desired test length. The final probe lengths were also recorded using a caliper, but this measurement was less accurate since it was measured relative to the curved strut at the base location. Therefore, an individual uncertainty of 0.015 in. was used for the sensor length which is about half an L/d for the 0.032 in. diameter probe. The effective thermal conductivity was estimated based on an area weighted average and thermal conductivity values from prior literature. However, the material properties of the insulating magnesium oxide powder were unknown and estimated from literature. An experiment was also to measure the effective thermal conductivity of a sheathed thermocouple. The measured k_{tc} was within 10% of the value estimated from literature; therefore, a 10% uncertainty in the effective thermal conductivity was used. Finally, the individual uncertainty of, *h*, was determined based on the Moffat Nusselt-Reynolds correlation, seen in Equation 2.19, that was used for low order predictions. This correlation provides a $\pm$ 0.06 value for the leading coefficient which results in a 13.7% uncertainty value. The total uncertainty in the low order model predictions using Moffat's correlation for a wire in perpendicular flow was calculated for each probe geometry and every predicted flow angle previously presented. The total uncertainty of the low order predictions compared to the experiment results for the symmetric strut can be seen in Figure 5.38.

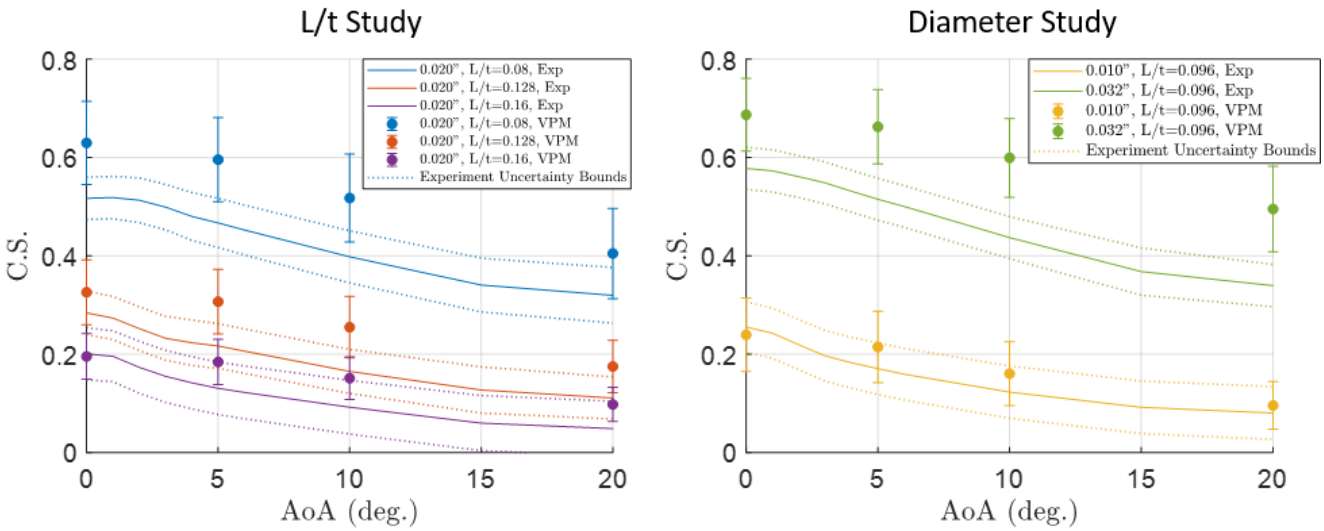

Figure 5.38: Comparison of total uncertainty for low-order predictions and experiment results, symmetric strut configurations, Moffat ⊥ correlation

As previously discussed, the low-order method over predicts all of the symmetric strut results. However, the uncertainty bounds for the experiment and low-order predictions overlap for the majority of the probe configurations. An uncertainty quantification was also performed for the Churchill-Bernstein correlation predictions using the same method and individual uncertainties. A comparison of the total uncertainties for the low order predictions using the Churchill-Bernstein correlation and the experiment results for the symmetric strut can be seen in Figure 5.39.

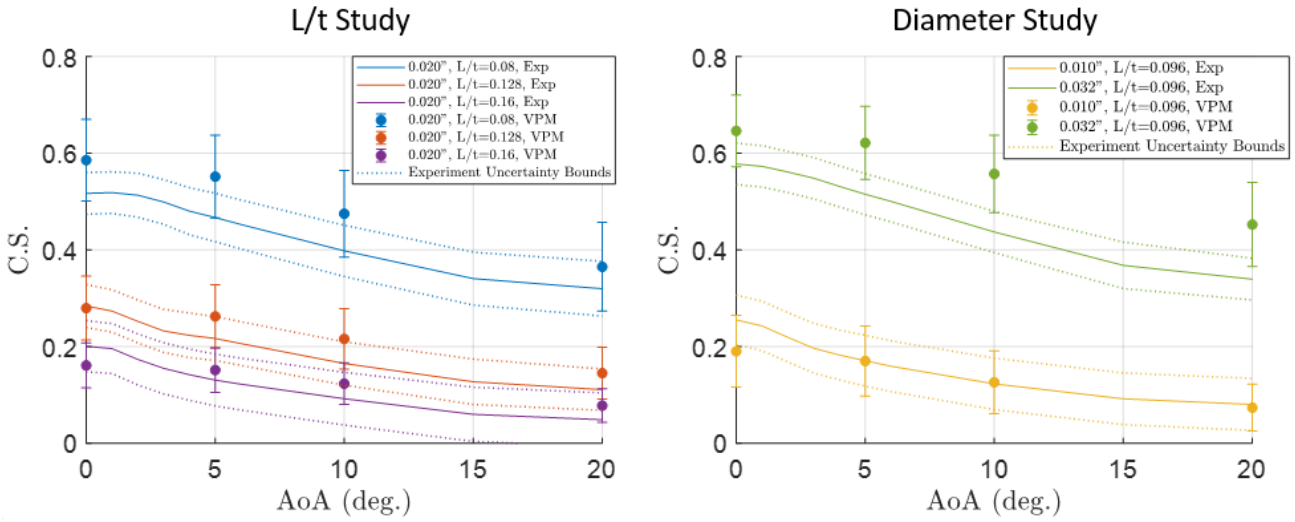

Figure 5.39: Comparison of total uncertainty for low-order predictions and experiment results, symmetric strut configurations, Churchill-Bernstein correlation

When the Churchill-Bernstein correlation is used, all of the symmetric strut predictions shift closer to the experiment results. All of the uncertainty bounds overlap between the predictions and experiments. This suggests that the uncertainty in the measured temperatures and input parameters used in the low-order predictions can explain the discrepancy between the magnitudes of the

experiment results and predictions. A potential explanation for the generally high predictions for the symmetric strut configurations is that the strut is shedding and this shedding is not captured in the 2D CFD flow-field solutions. This theory is supported by the excellent agreement between the cambered experiment and low-order predictions, since the cambered strut has a smaller t/c and would be less likely to shed. An uncertainty quantification was also performed for the cambered strut results using the previously discussed method and individual uncertainties. This total uncertainty quantification was performed using both the Churchill-Bernstein correlation and Moffat correlation for a wire in perpendicular flow. A comparison of the total uncertainties for the low order predictions using both correlations and the experiment results for the cambered strut can be seen in Figure 5.40.

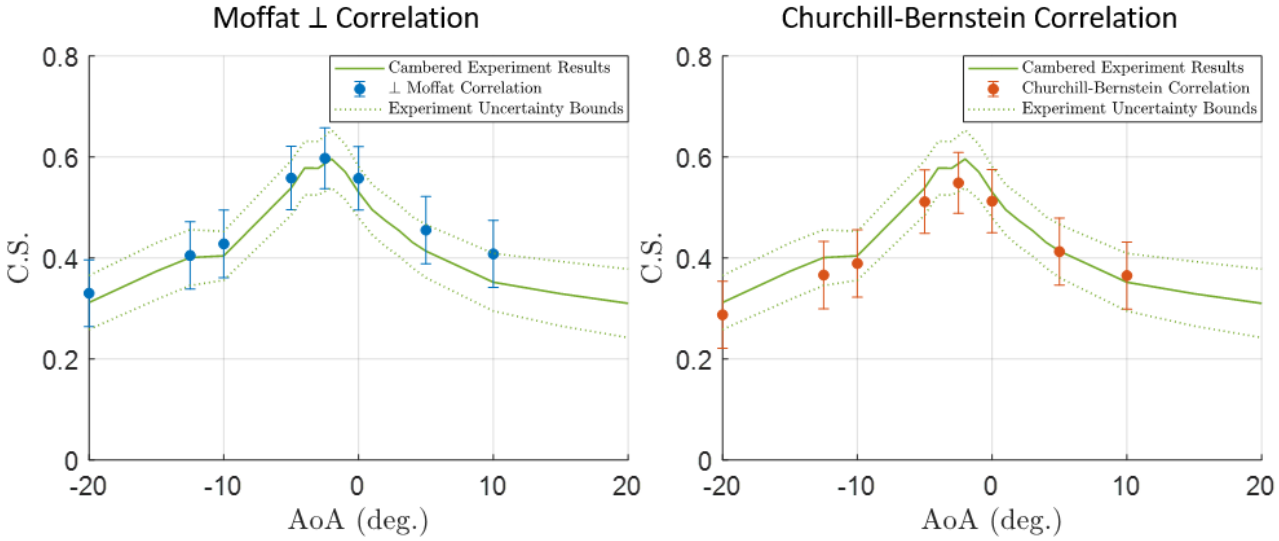

Figure 5.40: Comparison of total uncertainty for low order predictions and experiment results, symmetric strut configurations, Churchill-Bernstein correlation

The total uncertainty bounds primarily overlap for both correlations and the low order predictions all fall within the experiment uncertainty bounds. Finally, the total uncertainty for the low order predictions was recalculated to include the dependent variables in the h equation. Conduction sensitivity's dependent variables for this revised method can be seen in Equation 5.15. Similarly, the developed total uncertainty equation for conduction sensitivity can be seen in Equation 5.16.

$$CS = f(\mathrm{L}, \mathrm{d}, k_{tc}, k_{fluid}, V_{local}, \nu) \tag{5.15}$$

$$\delta CS = \sqrt{(\frac{\partial R}{\partial \mathrm{L}} * \delta \mathrm{L})^2 + (\frac{\partial R}{\partial \mathrm{d}} * \delta \mathrm{d})^2 + (\frac{\partial R}{\partial k_{tc}} * \delta k_{tc})^2 + (\frac{\partial R}{\partial k_{fluid}} * \delta k_{fluid})^2 + (\frac{\partial R}{\partial V_{local}} * \delta V_{local})^2 + (\frac{\partial R}{\partial \nu} * \delta \nu)^2} \tag{5.16}$$

The same values for the previously described individual uncertainties were used. Additionally, a 2% uncertainty in the fluid properties k_{fluid} and ν was used along with a 10% uncertainty in the local velocity determined from the virtual probe method. The total uncertainties for the low order predictions were then recalculated using the new formulation. A comparison of total uncertainties

using the new formulation and original formulation for the symmetric strut conduction sensitivity predictions can be seen in Figure 5.41.

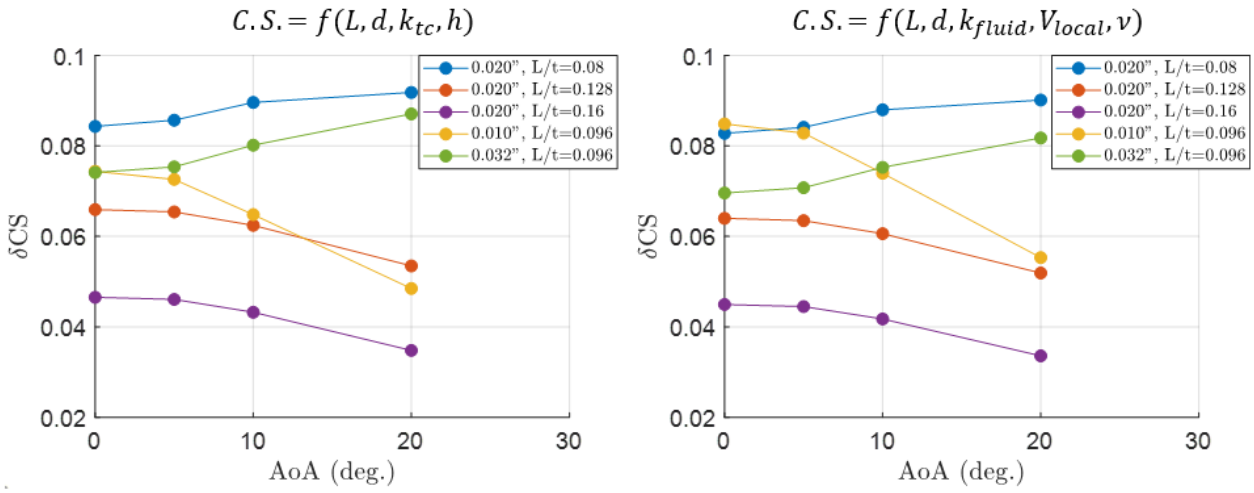

Figure 5.41: Comparison of total uncertainty for low-order predictions using different dependent variables, uncertainty of symmetric strut predictions using Moffat ⊥ correlation

The uncertainty results in Figure 5.41 show that the trend in uncertainty with angle remains the same between the two different formulations. However, the formulation utilizing a defined, *h*, uncertainty from the Moffat correlation results in slightly higher total uncertainty values for all probe geometries except the 0.010 in. diameter probe.

6 Conclusion

A fundamental study of mount interference and freestream flow angle effects on unshielded total temperature probe aerodynamic error and conduction error was performed. A low-order method was developed to account for mount interference and flow angle effects in the prediction of aerodynamic error and conduction error. The following section will review the developed low order method and insight gained by the performed experiments and complementary 3D, CFD/CHT simulations.

An experiment to study mount interference effects on the aerodynamic error of total temperature probes was designed and performed in the Virginia Tech Heated Jet facility. Three temperature probe geometries were mounted into a NACA 0024 strut, and temperature data was collected for Mach numbers varying between 0.25 and 0.72. This Mach number sweep provided data for a range of mount interference conditions, and three different probe L/t values were tested. Two sheathed thermocouples of varying length, and a beaded, bare wire sensor, were tested. The results of this experiment showed that reducing probe L/t can reduce aerodynamic error on a conventionally positioned probe aligned with the freestream. This occurs because the probe tip moves closer to the strut stagnation point and the local flow velocity decreases as L/t is reduced. Additionally, this experimental study identified that the strut stagnation point provides a Mach insensitivity for short L/t total temperature probes.

A low-order method to account for mount interference in aerodynamic error predictions was developed. The low-order method utilizes a flow solution from potential flow theory, a panel method, or 2D CFD simulation to identify the flow velocity local to the tip of the probe. The ratio of the identified local velocity squared to the freestream velocity squared is then used in an analytical expression presented by Moffat to account for how the mount reduces aerodynamic error. A Rankine half-body flow solution and the developed low-order method were used to predict aerodynamic error for each total temperature probe geometry and every Mach number tested experimentally. Predictions using the developed low-order method were capable of predicting the same Mach insensitivity and recovery increase with decreasing L/t that was witnessed in the experiment. Additionally, the developed prediction method provided good agreement with the experiment results and a more accurate estimate of aerodynamic error than the historic, freestream-based expression.

A set of experimental studies were also performed to analyze both mount interference and freestream flow angle effects on the conduction error of a total temperature probe. The conduction error experiments were performed in the Virginia Tech Open Jet Wind Tunnel, and five different sheathed probe geometries were tested on a symmetric strut. Three sheathed 0.020 in. diameter probes were tested with varying L/t values, and two sheathed probes with constant L/t but varying diameters were tested. All of the experiments were performed with a freestream Mach number of 0.038, Reynolds number of 64,000, and the strut/probe pitch angle was varied between -30° and 30° during angle sweeps. This low Mach number provided negligible aerodynamic error and the conduction sensitivity parameter was used to assess probe performance. This conduction

sensitivity parameter described the probe conduction error independent of conduction driver and was extremely useful for nondimensional scaling of experiments.

The results of the off-angle conduction error experiments showed that unshielded total temperature probes have improved performance at off-angles, but are sensitive to freestream flow angle. 3D, CFD/CHT simulations were performed in conjunction with the conduction error experiments to provide key heat transfer information and flow visualizations. It was identified that at off-angle conditions, the flow around an unshielded total temperature probe closely resembles a cylinder in crossflow. This is caused by a strut induced pressure gradient and results in an increased, *h*, profile along the length of the sensor at off-angle conditions. Additionally, it was identified that the average convection coefficient, *h*, is largely independent of the probe length. Off-angle experiments were also performed using a cambered mounting strut. One total temperature probe geometry was tested over a pitch angle range of -30° to 30°. The results of this experiment showed that unshielded total temperature probe performance is highly dependent on strut geometry, but the trends identified with flow angle hold true for varying strut geometries. A forced freestream unsteadiness experiment was also conducted using the same facility, symmetric strut, and the nominal 0.020 in. diameter total temperature probe. Flow unsteadiness was induced by positioning a circular cylinder upstream of the tested strut/probe configuration. This study showed that freestream unsteadiness significantly reduces conduction error at low angles and results in an insensitivity to freestream flow angle. These benefits are a result of flow unsteadiness increasing convection to the temperature sensor and high angle performance being dominated by strut induced crossflow.

A low-order method, referred to as the virtual probe method, was developed to account for mount interference and flow angle effects in conduction error predictions. This method uses a local velocity profile that is extracted from a strut flow-field solution obtained using potential flow theory or 2D, CFD simulations. This local velocity profile is used in an applicable Nusselt-Reynolds correlation and conduction error model to account for the impacts of mount interference and freestream flow angle. Predictions using the virtual probe method were performed for each probe experimentally tested on the symmetric and cambered struts. These predictions used the virtual probe method, an enhanced conduction model, and several Nusselt-Reynolds correlations. It was determined that the Churchill-Bernstein correlation and Moffat correlation for a bare-wire thermocouple in perpendicular flow contained the most relevant physics for an off-angle sheathed total temperature probe. Predictions using these correlations, the virtual probe method, and an enhanced conduction model closely matched results from 3D, CFD/CHT simulations. Uncertainties in the experimental measurements and in the physical properties used for predictions resulted in some variations between predictions and the experiment results. However, many of the predictions and experiments showed good agreement and all predictions were able to accurately capture flow angle trends. Additionally, the low-order predictions were able to accurately account for the impacts of varying probe L/t and L/d.

In conclusion, the effects of mount interference and freestream flow angle were investigated. The impacts of each effect were identified, and a low-order method was developed to account for these effects. The developed method is capable of accounting for mount interference effects on

aerodynamic error through the use of a local Mach number. Similarly, the developed virtual probe method is capable of accounting for mount interference and flow angle effects on conduction error through the use of a local Reynolds number. The developed methods are considerably quicker to perform than full-scale 3D, CFD simulations, and they can be utilized for the design of unshielded total temperature probes in a wide range of applications.

6.1 Future Work

One primary area that was not covered in this study was the effects of radiation on unshielded total temperature probes. There are many high temperature applications for total temperature probes where radiation would be a primary source of heat transfer. There exists a wide range of prior literature on the prediction of radiation error [11,12,22-26]. These radiation predictions methods could be coupled with the low-order methods presented in this study for the prediction of probe performance in complex heat transfer environments. Also, a simple investigation of the effects of flow unsteadiness was performed in this study. Freestream flow unsteadiness is present in most gas-turbine applications of total temperature probes, and additional work to thoroughly analyze and model the effects of freestream, forced unsteady flow would be very valuable.

REFERENCES

[1] Franz, A., “Pressure and Temperature Measurement in Supercharger Investigations”, NACA Technical Report NACATM-953, National Advisory Committee for Aeronautics, 1940.

[2] Lindsey, W.F., “Calibration of Three Temperature Probes and Pressure Probe at High Speeds”, Report, National Advisory Committee for Aeronautics, 1942.

[3] King, W.J., “Measurement of High Temperatures in High Velocity Gas Streams”, Trans. ASME, 65:421, 1943.

[4] Hottel, H.C., and Kalitinsky, A., “Temperature Measurements in High-Velocity Air Streams”, J. Applied Mechanics, 12:A25-A32, 1945.

[5] Markowski, S. and Moffatt, E., "INSTRUMENTATION for Development of AIRCRAFT POWERPLANT COMPONENTS Involving FLUID FLOW," SAE Technical Paper 480179, 1948, doi:10.4271/480179.

[6] Gerhard, R. E., “Shielded Thermocouples”, In “Physical Measurements in Gas Dynamics and Combustion,” Princeton University Press, Princeton, NJ, 1954.

[7] Winkler, E.M., “Design and Calibration of Stagnation Temperature Probes for Use at High Supersonic Speeds and Elevated Temperatures,” J. Applied Physics, 25:231-232, 1954.

[8] Moffat, R.J., “Gas Temperature Measurement”, Temperature, Its Measurement and Control in Science and Industry, Vol. 3, Part 2, 1962.

[9] Gorlin, S.M. and Slezinger, I.I., “Wind Tunnels and Instrumentation,” Izdatel’stvo “Nauka, Moskva, 1964.”

[10] Albertson, C.W. and Bauserman W.A., Jr., “Total Temperature Probes for High-Temperature Hypersonic Boundary Layer Measurements,” NASA TM 4407, 1993.

[11] Schetz, J.A., Vincent, T.G. and Lowe, K.T., “Analysis of Base-Cooled Total Temperature Probes with Radiation,” ASME Paper IMECE2016-65130, 2016.

[12] Vincent, T., Schetz, J., and Lowe, K., "Enhanced Low-Order Model with Radiation for Total Temperature Probe Analysis and Design," SAE Technical Paper 2017-01-2047, 2017, doi:10.4271/2017-01-2047.

[13] Anderson, J. D. Jr., *Fundamentals of Aerodynamics, 5th ed.*, New York: McGraw-Hill, pp. 538, (2011).

[14] Ecker, T., Lowe, K. T., and Ng, W. F., “Eddy Convection in Developing Heated Supersonic Jets,” AIAA Journal, vol. 53, Nov. 2015, pp. 3305–3315.

[15] Ecker, T., Brooks, D. R., Lowe, K. T., and Ng, W. F., “Development and Application of a Point Doppler Velocimeter Featuring Two-Beam Multiplexing for Time-Resolved Measurements of High-Speed Flow,” Experiments in Fluids, vol. 55, Sep. 2014, pp. 1819.

[16] Ismail, Mohamed, and Devin Alexander. “The Basics of Thermocouples.” *Maxim Integrated*, Maxim Integrated Products, Inc., 26 Mar. 2018, www.maximintegrated.com/en/app-notes/index.mvp/id/6550.

[17] Ramberg, Steven E. "The effects of yaw and finite length upon the vortex wakes of stationary and vibrating circular cylinders." *Journal of Fluid Mechanics* 128 (1983): 81-107.

[18] “Temperature Sensor Basics.” *National Instruments*, National Instruments, 19 Mar. 2019, www.ni.com/en-us/innovations/white-papers/16/temperature-sensor-basics.html.

[19] Schetz, J.A. and Bowersox, R.D.W. “Boundary layer analysis.” 2nd ed. AIAA Reston, VA 2011.

[20] Eckert, E.R.G. and Drake, R.M. “Heat and Mass Transfer.” McGraw-Hill Book Company, Inc. New York. 1959. pg. 39-42.
[21] Özişik, M.N. “Basic Heat Transfer.” McGraw Hill Book Company. New York. 1977. pg. 68-71.
[22] Dahl, A.I. and Fiock, E.F. “Thermocouple pyrometers for gas turbines.” Trans. ASME 71, 153. 1949.
[23] Moffatt, E.M. “Multiple Shielded High Temperature Probes – Comparison of Experimental and Calculated Errors.” SAE T-13. 1952.
[24] West, W.E. and Westwater, J.W. “Radiation-conduction correction for temperature measurements in hot gases.” Ind. and Eng. Chem. 45, 2152-2156. 1953.
[25] Dahl, A.I. and Freeze, P.D. “Tests of Total Temperature Probes.” WADC Technical Report 53-251. 1953.
[26] Glawe, G.E. and Shepard, C.E. “Some effects of exposure to exhaust-gas streams on emittance and thermoelectric power of bare wire platinum rhodium-platinum thermocouples.” NACA TN-3253. 1954.
[27] Hottel, H.C., and Sarofim, A.F.: “Radiative Transfer,” McGraw-Hill Book Company, New York 1967
[28] Özişik, M.N.: “Radiative Transfer and Interations with Conduction and Convection,” John Wiley & Sons, Inc., New York, 1973.
[29] Singham, J.R.: Tables of Emissivity of Surfaces, Int. J. Heat Mass Transfer, 5:67-76 (1962)
[30] Gubareff, G.G, Janssen, J.E: “Thermal Radiation Properties Survey,” Honeywell Research Center, Honeywell Regulator Company, Minneapolis, 1960.
[31] Englerth, S.T. The study of conduction error of cooled total temperature probes. Master’s thesis. Virginia Tech. 2015.
[32] Moffat, R.J. “Designing thermocouples for response rate.” Trans. ASME 80, 257. 1958.
[33] Dahl, A.I. and Fiock, E.F. “Response characteristics of temperature sensing elements for use in the control of jet engines.” J. Research Natl. Bur. Standards, Vol. 45, No. 4. 1950.
[34] Wormser, A.F. “Experimental determination of thermocouple time constants with use of a variable turbulence, variable density wind tunnel, and the analytic evaluation of conduction, radiation, and other secondary effects.” SAE Preprint 158D. 1960.
[35] Shepard, R.L. and Carroll, R.M. “Measurement of the transient response of thermocouple and resistance thermometers using an in situ method.” ORNL/TM-4573. 1977.
[36] Goodwin, W. N., Response time and lag of a thermometer element in a protecting case, Am. Inst. Elec. Engrs. 64, 665 (1945)
[37] Beede, H.M. and Droms, C.R. “A simplified thermocouple for temperature measurements in high velocity gas streams.” Instruments 24, 338. 1951.
[38] Scadron, M.D. and Warshawsky, I. “Experimental Determination of Time Constants and Nusselt Numbers for Bare Wire Thermocouples in High Velocity Air Streams and Analytical Approximation of Conduction and Radiation Error.” NACA TN-2599. 1952.
[39] Glawe, George E., and Robert C. Johnson. "Experimental Study of Heat Transfer to Small Cylinders in a Subsonic, High-Temperature Gas Stream." (1957).
[40] Shang, Jessica K., H. A. Stone, and A. J. Smits. "Flow past finite cylinders of constant curvature." *Journal of Fluid Mechanics* 837 (2018): 896-915.
[41] Cadel, Daniel R. *Advanced Instrumentation and Measurements Techniques for Near Surface Flows*. Diss. Virginia Tech, 2016.

[42] Clark, Christopher. "Measuring the Vortex-Shedding Frequency Behind Staggered Cylinders in Cross-Flow." (2018).
[43] Churchill, S. W., and M. Bernstein. "A correlating equation for forced convection from gases and liquids to a circular cylinder in crossflow." *Journal of Heat Transfer* 99.2 (1977): 300-306.
[44] ANSYS Fluent, Software Package, Release 14.5, Sections “ANSYS Fluent User’s Guide,” and “ANSYS Fluent Theory Guide,” ANSYS Inc., Canonsburg, PA, 2013, http://148.204.81.206/Ansys/readme.html [retrieved 24 Dec. 2019]
[45] Schneider, A.J. “Computational modeling of total temperature probes.” Master’s thesis. Virginia Tech. 2015. [46] Reardon, J. P., “Computational Modeling of Radiation Effects on Total Temperature Probes,” M.S. Thesis, Aerospace and Ocean Engineering Dept., Virginia Polytechnic Inst. and State Univ., Blacksburg, VA, Jan. 2016.
[47] Godbee, H. W., and W. T. Ziegler. "Thermal conductivity of MgO, A12O3, and ZrO2 powders to 850° C." *Journal of Applied Physics* 37.1 (1965): 56.
[48] Kline, S. J. and McClintock, F. A. (1953). Describing the uncertainties in single sample experiments. Mechanical Engineering, pages 3–8.
[49] Cadel, D.R., Zhang, D., Lowe, K.T. and Paterson, E.G., 2018. Unsteady boundary layer development on a wind turbine blade: an experimental study of a surrogate problem. Experiments in Fluids, 59(4), p.72.